

**3-D LIVER RECONSTRUCTION
AND MODELING FOR SURGICAL SIMULATION**



**A Thesis Submitted in Partial Fulfillment of the Requirements for the
Degree of Doctor of Philosophy in
Telecommunication and Computer Engineering
Suranaree University of Technology
Academic Year 2020**

การสร้างคืบและแบบจำลองตัว 3 มิติเพื่อการจำลองการผ่าตัด



นายควน กอง เลอ

วิทยานิพนธ์นี้เป็นส่วนหนึ่งของการศึกษาตามหลักสูตรปริญญาวิศวกรรมศาสตรดุษฎีบัณฑิต

สาขาวิชาวิศวกรรมโทรคมนาคมและคอมพิวเตอร์

มหาวิทยาลัยเทคโนโลยีสุรนารี

ปีการศึกษา 2563

**3-D LIVER RECONSTRUCTION
AND MODELING FOR SURGICAL SIMULATION**

Suranaree University of Technology has approved this thesis submitted in partial fulfillment of the requirements for the Degree of Doctor of Philosophy.

Thesis Examining Committee



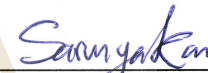
(Asst. Prof. Dr. Krisana Chinnasarn)

Chairperson



(Asst. Prof. Dr. Paramate Horkaew)

Member (Thesis Advisor)



(Dr. Sarunya Kanjanawattana)

Member



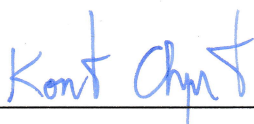
(Assoc. Prof. Dr. Peerapong Uthansakul)

Member



(Assoc. Prof. Dr. Monthippa Uthansakul)

Member



(Assoc. Prof. Ft. Lt. Dr. Kontorn Chamniprasart)

Vice Rector for Academic Affairs
and Internationalization



(Assoc. Prof. Dr. Pornsiri Jongkol)

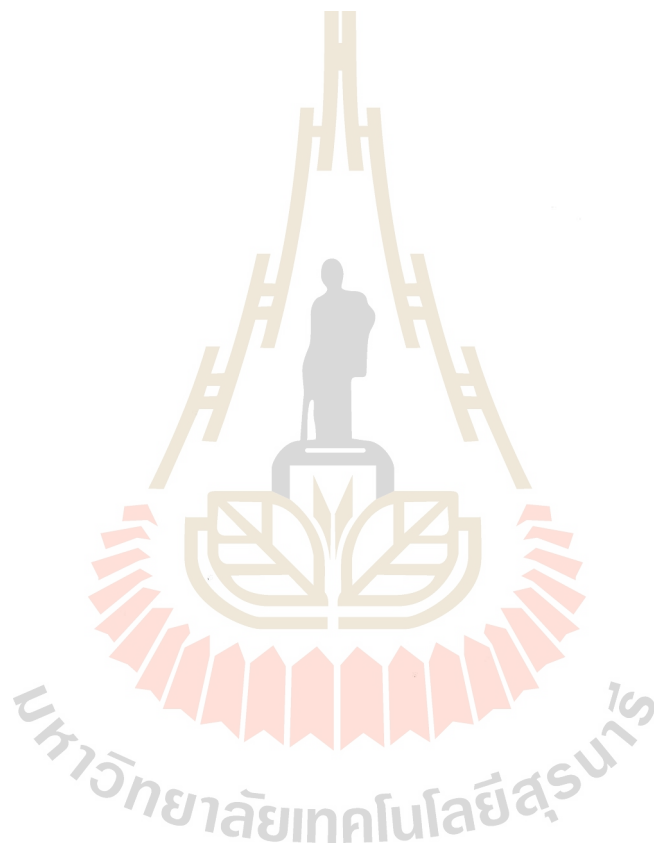
Dean of Institute of Engineering

ควาน คอง เลอ : การสร้างคีนและแบบจำลองดัด 3 มิติเพื่อการจำลองการผ่าตัด (3-D LIVER RECONSTRUCTION AND MODELING FOR SURGICAL SIMULATION) อาจารย์ที่ปรึกษา : ผู้ช่วยศาสตราจารย์ ดร. ประเมศวร์ ห่อแก้ว, 206 หน้า.

ในช่วงไม่กี่ทศวรรษที่ผ่านมาได้พบการใช้ภาพทางการแพทย์ของดัดอย่างกว้างขวางเพื่อประโยชน์ในการวินิจฉัย และการบำบัดรักษา โดยเฉพาะอย่างยิ่งในการผ่าตัดดัด แม้ภาพถ่ายของดัดที่บันทึกโดยเครื่องกวาดภาพจะประกอบด้วยข่าวสารที่สำคัญ และสอดคล้องกับกายวิภาค ทว่าความซับซ้อนเชิงโครงสร้างรวมถึงความต่างขัระหว่างดัดและเนื้อเยื่อรอบข้างที่ต่ำ ก่อเกิดความท้าทายที่สำคัญหลายประการที่จำเป็นต้องเผชิญ ประการแรก เพื่อประโยชน์ต่อการนำเสนอจำเป็นต้องระบุบริเวณของดัดให้เห็นชัดด้วยเทคนิคการสะกดภาพ หลังจากนั้นจึงสร้างแบบจำลอง มิติของดัดจากบริเวณที่สะกดเพื่อสร้างจินตทัศน์ของอวัยวะ เป็นที่ทราบกันว่าความเข้าใจที่ลึกซึ้งของกายวิภาค และโครงสร้างของดัดก่อนการผ่าตัดครั้งสำคัญ จัดเป็นข้อกำหนดเบื้องต้นที่สำคัญประการหนึ่งเพื่อลดความเสี่ยง และสร้างความมั่นใจว่าผู้ป่วยจะรอดชีวิต โดยเฉพาะอย่างยิ่งการระบุตำแหน่งและอณาบริเวณของชิ้นส่วนซึ่งมีหน้าที่อิสระอย่างถูกต้อง มีส่วนช่วยศัลยแพทย์ในการผ่าตัดบริเวณที่กำหนดได้โดยไม่ก่อให้เกิดความเสียหายต่อบริเวณอื่น ๆ อีกทั้งยังลดการสูญเสียเลือดสำหรับการผ่าตัดปลูกถ่ายดัดจากผู้บริจาคที่ยังมีชีวิต การวัดปริมาตรของชิ้นส่วนปลูกถ่ายที่แม่นยำมีความสำคัญยิ่งยวดต่อการหลีกเลี่ยงความไม่สมบูรณ์เพียงพองของดัดภายหลังการผ่าตัด ในทางปฏิบัติจินตทัศน์ มิติมีบทบาทช่วยสนับสนุนการแบ่งปันข่าวสารของดัด และอวัยวะแวดล้อม กระบวนการดังกล่าวมุ่งเน้นเพื่อลดความเข้าใจที่ไม่ตรงกันระหว่างสมาชิกของกลุ่มศัลแพทย์ นอกจากนี้จินตทัศน์ยังมีประโยชน์ต่อแพทย์ฝึกหัด และศัลยแพทย์ในการฝึกปฏิบัติเทคโนโลยีใหม่ ๆ

ด้วยแรงบันดาลใจจากเหตุผลดังกล่าว วิทยานิพนธ์นี้จึงเสนอ วิธีการสร้างคีนดัด มิติโดยอาศัยภาพถ่ายทางการแพทย์ ในการนี้จักเริ่มจากการสะกดแบบจำลองกายวิภาค มิติของดัด และหลอดเลือดออกจากภาพเชิงปริมาตร โดยใช้กลยุทธ์การสะกดภาพ หลังจากนั้นชิ้นส่วนที่สำคัญจำนวน ชิ้นจะถูกแบ่งจำแนกออกจากดัดตามนิยามทางกายวิภาคซึ่งอ้างอิงกับโครงข่ายหลอดเลือดถัดมาจึงสร้างจินตทัศน์ มิติ และจำลองสถานการณ์เฉพาะผู้ป่วยเพื่อสนับสนุนการวางแผนก่อนการผ่าตัด และการบริหารจัดการหลังการผ่าตัด สุดท้ายการหาค่าตัวแปรของโครงข่าย และการแปลงที่คล้ายคลึงจะใช้ในการช่วยประมาณปริมาตรของชิ้นส่วนปลูกถ่าย ซึ่งพิจารณาจากความเข้าใจของชิ้นส่วนในการปลูกถ่าย ผู้วิจัยตรวจสอบความถูกต้องของวิธีการที่นำเสนอกับชุดข้อมูลสาธารณะชื่อว่า **MICCAI SLIVER 2007** และดำเนินการทดลองการสะกดแยกดัด เปรียบเทียบ

ผลกับวิธีการร่วมสมัยต่าง ๆ อ้างอิงกับมาตรวัดที่เกี่ยวข้องทางคลินิก การประเมินทั้งด้วยสายตา และเชิงเลข ทั้งนี้รายงานในวิทยานิพนธ์นี้บ่งชี้ว่า ระบบที่นำเสนอสามารถปรับปรุงความแม่นยำ และความเชื่อถือได้ของการสกัดแยก พร้อมกันนี้การระบุตำแหน่งที่แม่นยำของชิ้นส่วนเชิงหน้าที่ ของตับแสดงให้เห็นว่าวิธีการที่เสนอสามารถกำหนดหมายชิ้นส่วนตามนิยามของควีโน โดยเฉพาะอย่างยิ่งชิ้นคาเดท โดยพึ่งพาการโต้ตอบจากผู้ใช้ในระดับที่น้อยกว่า ผลการศึกษาเบื้องต้นยังนำไปสู่ ข้อเสนอแนะว่าสามารถบูรณาการวิธีการดังกล่าวเพื่อเสริมการวางแผนและการแทรกแซงการผ่าตัด ได้อีกด้วย



สาขาวิชา วิศวกรรมคอมพิวเตอร์
ปีการศึกษา 2563

ลายมือชื่อนักศึกษา

Uluam

ลายมือชื่ออาจารย์ที่ปรึกษา

Paromte Herkano

DOAN CONG LE : 3-D LIVER RECONSTRUCTION AND MODELING FOR
SURGICAL SIMULATION. THESIS ADVISOR : ASST. PROF. PARAMATE
HORKAEW, PhD., 206 PP.

LIVER/RECONSTRUCTION/MODELING/SURGICAL SIMULATION

Over recent decades, medical image of the liver has been widely used in diagnostics and treatment, particularly in hepatectomy. Although the liver images recorded by scanners provide useful information relevant to the anatomy, the structural complexity as well as the low contrast between liver and surrounding tissues lead to major challenges needed to be solved. Firstly, to have a better presentation, the segmentation is applied to locate and highlight the liver. Then, the 3-D liver model generated from segmented results is used for visualization. It has been known that deeper understanding of the anatomy of liver and its structure prior a major surgery is considered as one of most important prerequisites to reduce the risks and ensure the survival of patients. Particularly, the correct localization of functionally independent segments assists surgeons to operate on a specified region without causing damages to other regions as well as reducing the blood losing. In living donor liver transplantation, accurate measurement of graft volumetry (GV) of liver in donor is critical to avoid the liver insufficiency in post-operation. In real practices, the 3-D visualization enables information sharing of liver and its peripherals. It aims to avoid the misunderstanding between members of surgical team. The visualization is also useful for trainee and surgeons in practicing new technologies.

Motivated by these reasons, this thesis proposes a method for 3D liver reconstruction by using medical image. To this end, a 3D anatomical model of a liver and vessels were first extracted from a volumetric image, using image segmentation strategies. Subsequently, eight segments on the extracted liver were separated based on anatomical definition and vascular network. Next, 3D visualization and subject-specific surgical simulation were performed to support both pre-operative planning and post-operative administration. Finally, mesh parameterization combined similarity transformation assists to estimate the GV, which was used to assess the compatibility of the graft to be implanted. The proposed method was evaluated on a public datasets MICCAI SLIVER 2007. The experimental results on segmentation of liver were benchmarked against the state-of-the-art methods, based on major clinically relevant metrics. Both visual and numerical assessments reported herein indicated that the proposed system could improve the accuracy and reliability of segmentation. Simultaneously, the accurate localization of functional segments of liver implied that the proposed method could faithfully label all Couinaud's segments, especially the caudate, with lesser degree of user interaction. The preliminary findings suggested that it can be integrated into augmented surgical planning and intervention.

School of Computer Engineering

Academic year 2563

Student's signature



Advisor's signature



ACKNOWLEDGEMENTS

Foremostly, I would like to express my sincerest gratitude to my advisor, Asst. Prof. Dr. Paramate Horkaew for bringing me to scientific research. During recent years at Suranaree University of Technology, his kindly supports, patience, and understanding have truly motivated me to this study. Next, I am also very grateful to Doctors, Nattawut Keeratibharat and Jirapa Chansangrat who have ideas, expert advice, and assessment for this research. Without these supports, this study would not be possible.

Besides my advisor, I would like to thank to Committee for the suggestions and comments to my thesis. These feedbacks not only help to improve my study but also useful for my research in future.

I would like to thank to Suranaree University of Technology for financial supporting under SUT-PhD Scholarship Program for ASEAN. I am very thankful to School of Computer Engineering, Institute of Engineering, Center for International Affairs, Suranaree University of Technology for giving me the opportunity and supporting me during my time here.

I would like to acknowledge with gratitude An Giang University and Faculty of Information Technology for supporting and allowing me to study in these years.

Lastly, I would like to present my deepest thanks to my parents, my parents-in-law, my lovely wife, and daughters for the encouragement me every day. Their supports and words helped me to be more patient and stronger in studying.

I am also thankful to authors for providing the dataset and open-source libraries which were employed in this study.

Doan Cong Le



TABLE OF CONTENTS

	Page
ABSTRACT (THAI)	I
ABSTRACT (ENGLISH).....	III
ACKNOWLEDGEMENTS.....	V
TABLE OF CONTENTS.....	VII
LIST OF TABLES	XIII
LIST OF FIGURES	XV
CHAPTER	
1 INTRODUCTION.....	1
1.1 Liver segmentation in surgical planning.....	2
1.1.1 Liver: anatomy and function.....	4
1.1.2 Segmentation and simulation.....	6
1.2 Motivation.....	11
1.3 The purposes	12
1.4 Scope of research	13
1.5 Outline of the thesis	15
2 LITERATURE REVIEW	16

TABLE OF CONTENTS (Continued)

	Page
2. 1 Medical imaging	17
2. 1. 1 Computed Tomography	17
2. 1. 2 Magnetic Resonance Imaging	22
2. 1. 3 Digital Imaging and Communications	24
2. 2 Digital image processing.....	26
2. 2. 1 Digital image.....	27
2. 2. 2 Fourier transform	27
2. 2. 3 Image processing	31
2.2.3.1 Filtering	31
2.2.3.2 Morphological operators	34
2.2.3.3 Texture feature	36
2. 2. 4 Image segmentation	39
2. 3 Liver segmentation approaches.....	47
2. 3. 1 Thresholding	49
2. 3. 2 Region growing.....	50
2. 3. 3 Contour delineation.....	51
2. 3. 4 Graph based segmentation	54

TABLE OF CONTENTS (Continued)

	Page
2. 3. 5 Statistical shape model.....	56
2. 4 3-D representation and pre-processing	60
2. 4. 1 Volumetric data.....	60
2. 4. 2 Volumetric visualization.....	60
2.4.2.1 Multi planar visualization.....	61
2.4.2.2 Surface rendering	62
2.4.2.3 Volumetric rendering	63
2. 4. 3 Three-dimensional file format	63
2. 4. 4 Marching cubes.....	65
2. 4. 5 Mesh smoothing.....	68
2. 5 Functional segmentation for preoperative liver	71
2. 5. 1 Voxel-based approach.....	74
2. 5. 2 Surface-based approach	76
2. 5. 3 Summary of latest algorithms	77
2. 6 Mesh parameterization.....	79
2. 7 Liver and general surgical simulation.....	83
3 METHODOLOGY	85

TABLE OF CONTENTS (Continued)

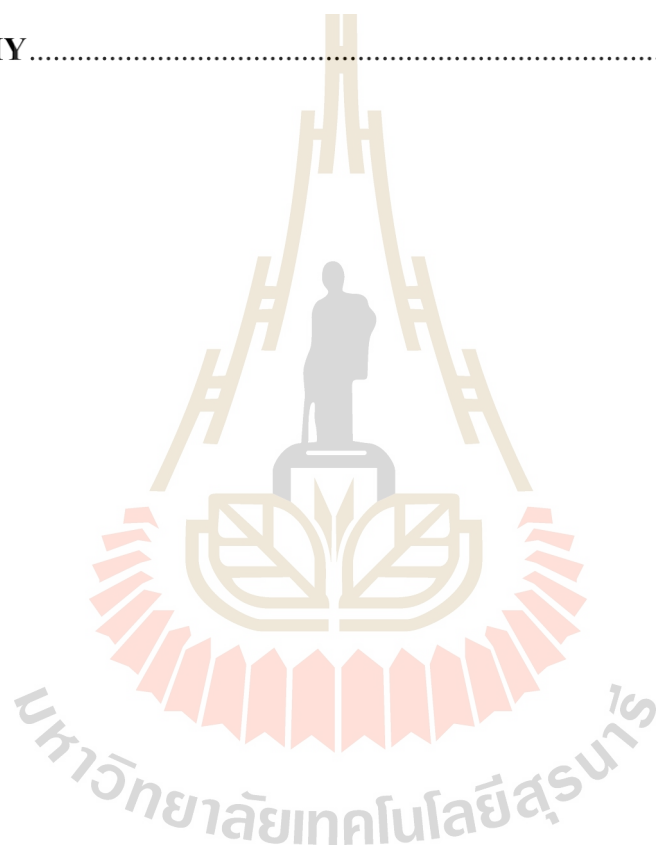
	Page
3. 1 Liver segmentation.....	86
3. 1. 1 Proposed schemes	86
3. 1. 2 Probabilistic model	89
3. 1. 3 Relaxation labeling	92
3. 1. 4 Graph cut.....	95
3. 1. 5 Bottleneck detection and anatomy-constraint.....	96
3. 1. 6 Improvements	102
3.1.6.1 3-D relaxation labeling.....	102
3.1.6.2 Anisotropic measurement.....	105
3. 2 Functional segmentation for preoperative liver	108
3. 2. 1 Liver and vessels segmentation	109
3. 2. 2 Tracing vascular centerlines	110
3. 2. 3 Functional segmentation	111
3.2.3.1 Differential Geometry of the Features.....	111
3.2.3.2 Locating Primary Functional Landmarks.....	115
3.2.3.3 Labeling Vessels and Extracting Vectors.....	117
3.2.3.4 Determining the Resections Planes	118

TABLE OF CONTENTS (Continued)

	Page
3.3 Parameterization of a Liver Surface	124
4 EXPERIMENTS AND RESULTS	127
4.1 Dataset and evaluation metrics	128
4.1.1 MICCAI dataset	129
4.1.2 Evaluation metrics	130
4.2 Liver segmentation results	134
4.3 Functional segmentation results	148
4.3.1 Liver dataset	149
4.3.2 Visual assessment	149
4.3.3 Numerical assessment	151
4.3.3.1 Overview of Functional Segments	152
4.3.3.2 Benchmarking	154
4.3.3.3 Evaluation at Lobe-Level	155
4.3.3.4 Evaluation at Section-Level	156
4.3.3.5 Evaluation at Functional Section-Level	157
4.4 Liver parameterization	160
4.5 Liver surgical simulation	166

TABLE OF CONTENTS (Continued)

	Page
5 CONCLUSION AND FUTURE WORK.....	170
REFERENCES.....	176
BIOGRAPHY.....	206



LIST OF TABLES

Table	Page
2.1	Examples of Hounsfield Units (Wilson, 2005) 19
2.2	A comparison between CT and MRI technique 23
2.3	The important information in DICOM head file 25
3.1	Process of building a multivariate probability density function..... 91
3.2	The contour-constraint algorithm..... 99
3.3	The algorithm of 3-D RL..... 104
3.4	Expressions of MHV, RHV, and RPV planes..... 119
3.5	Expressions of the bounding planes and surface of the segment I..... 123
4.1	Average user errors 133
4.2	The evaluation metrics obtained from 18 (labelled) cases. 134
4.3	The errors before and after removing IVC on the above case..... 140
4.4	Benchmarking on metrics and processing time..... 142
4.5	The evaluation metrics and score obtained from 7 asymptomatic 144
4.6	Comparison evaluation metrics and score..... 145
4.7	Percentage of functional segment volumes in liver..... 152
4.8	Averaged proportions (in %) of volume sizes in four sections 156
4.9	Averaged proportions (in %) of volume sizes in functional segments..... 158
4.10	The Hausdorff distance between the correct and projected paths 164
4.11	The Hausdorff distance between the correct and projected paths 165

LIST OF TABLES (Continued)

Table	Page
4.12 The RVD and error between estimated and actual volume.....	167
4.13 The RVD and error distance.....	167



LIST OF FIGURES

Figure	Page
1.1 The incidence rate and mortality rate of cancer in 2020.	2
1.2 The anatomy of abdominal organs under 3-D model.....	4
1.3 The Couinaud classification	5
1.4 The segmentation of the liver in abdominal CT.....	9
1.5 Some cases of CT image of the liver.....	14
2.1 The windowing of CT image.....	20
2.2 The distribution of CT number.....	21
2.3 The CT and MRI image of liver, brain.....	24
2.4 The organization of a DICOM	26
2.5 An example of Fourier transform.....	30
2.6 An example of smoothing image.....	34
2.7 Dilation operator.....	35
2.8 Erosion operator	35
2.9 An example of computing GLCM.....	37
2.10 An example of GLCM.....	38
2.11 An example of LBP	39
2.12 The structure of neighbors by different parameters (P, R).....	39
2.13 An example of region growing.....	41
2.14 A result of thresholding	42

LIST OF FIGURES (Continued)

Figure	Page
2.15 The result of level set method	47
2.16 Challenges associated with liver segmentation	48
2.17 The 18 voxels of scalar values composed from 3 slices.....	60
2.18 Multiplanar visualization of liver	61
2.19 Fifteen unique configurations of marching cube.....	65
2.20 An example of build marching cube for configuration 4	66
2.21 The intersection point and normal vector.....	67
2.22 Tangent planes, and directions of principal curvatures	70
2.23 The neighbour of a vertex and inter-angles.....	71
3.1 The workflow of proposed method by model 1.	87
3.2 The workflow of proposed method by model 2.	88
3.3 An example of probability map and relaxation labeling	94
3.4 Bottle neck detection using exterior angle constraint.....	98
3.5 The performance of BN-CC.....	101
3.6 The flow chart of post processing	102
3.7 Two cases of neighbours of pixel p	104
3.8 An example of anisotropic	107
3.9 Key steps of functional liver segmenting scheme.	109
3.10 The extracted venous system with overlaid centerlines	111
3.11 An example of mean curvature distribution	113

LIST OF FIGURES (Continued)

Figure	Page
3.12 Location of landmarks	116
3.13 Three vertical and two horizontal planes	118
3.14 Illustrations of the left HV plane (Π_{LHV})	120
3.15 The left PV plane (Π_{LPV}) (orange).....	121
3.16 The bounding planes of the segment I.....	122
3.17 The rigid and TPS of surface points	126
4.1 The workflow of experiments.	129
4.2 Box-Whiskers plots of metrics, and over scores	135
4.3 Examples of 3D segmentations	136
4.4 Selected examples of two healthy livers	137
4.5 Graph-cuts weight/ bottleneck angle and score.....	138
4.6 Graph-cuts weight / or exterior angle and score.....	138
4.7 An example of manually remove IVC	140
4.8 Segmentation of vessel and liver.....	141
4.9 Sample distribution of metrics	141
4.10 Illustration for segmentations of diseased livers	146
4.11 Results of spleen segmentation	147
4.12 The distribution of in- and out blood flows.....	150
4.13 Localization of a caudate segment	150
4.14 Box-Whisker (a) and tree plots (b) of segment volumes.....	153

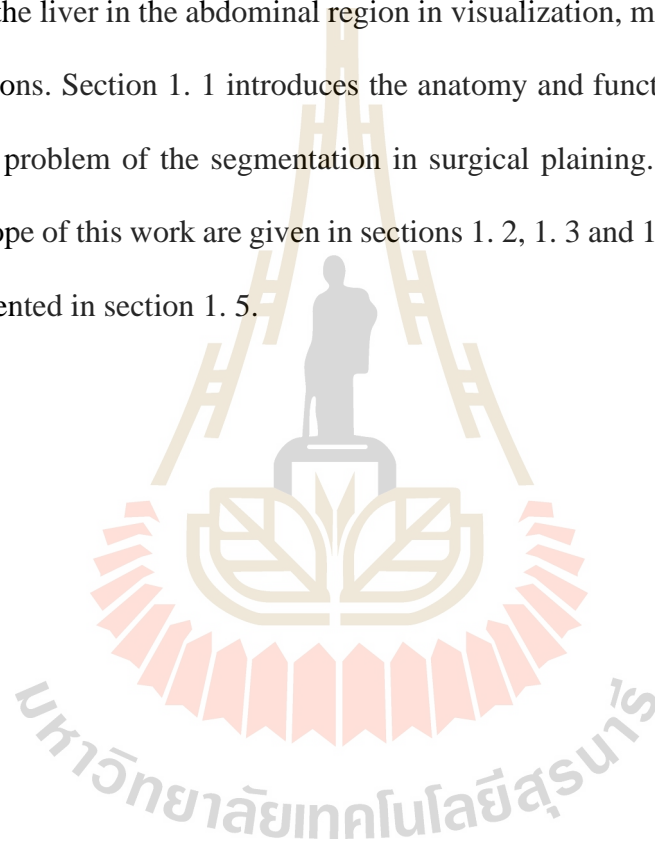
LIST OF FIGURES (Continued)

Figure	Page
4.15 The variation of volumetry between two subjects.....	154
4.16 Comparisons of relative segment volumes at lobe-level.....	156
4.17 The distributions of volume sizes evaluated at section level	157
4.18 The distributions of volume sizes evaluated at segment level	159
4.19 Landmark annotations	161
4.20 The SCM with landmark constraints.....	162
4.21 The registration (S'1) of source (S1) to target (S2).....	162
4.22 An example of resection on source and target livers.....	163
4.23 The error distances between projected and correct resection paths	166
4.24 Illustration of estimation of graft in examples	169

CHAPTER 1

INTRODUCTION

This chapter presents an overview of the importance of the segmentation and modeling of the liver in the abdominal region in visualization, monitoring, and simulation applications. Section 1. 1 introduces the anatomy and functions of liver, then the important of problem of the segmentation in surgical plaining. The motivation, purposes and scope of this work are given in sections 1. 2, 1. 3 and 1. 4 . The outline of the thesis is presented in section 1. 5.



1.1 Liver segmentation in surgical planning

Over recent decades, cancer has been known as one of leading causes of death worldwide. It was reported in 2018 (Bray et al., 2018; WHO, 2018) that, there were 18.1 million new cancer cases and 9.6 million cancer deaths in 2018. In a recent report, these number were updated, with 19.3 million and 10.0 million, respectively (Sung et al., 2021). The global burden is estimated to grow to 28.4 million by 2040 (Society, 2018). Among different cancer types, the rate of new liver cancer case and liver cancer death are 841,080 (4.7%), and 781,631 (8.2%) in 2018; and 905,667 (4.7%), and 830,180 (8.3%) in 2020, respectively (shown in **Figure 1.1**).

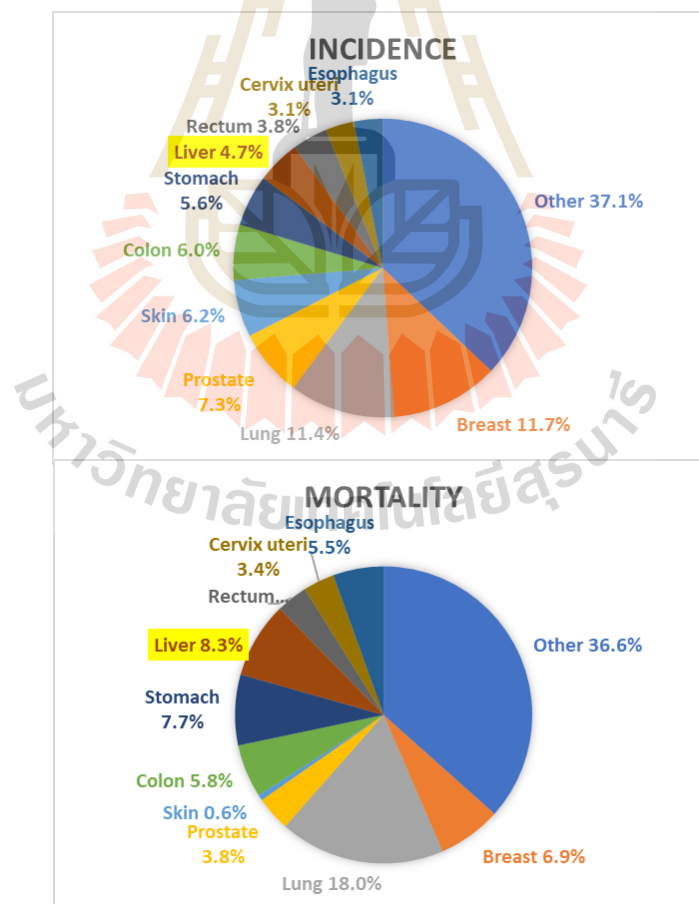


Figure 1.1 The incidence rate and mortality rate of cancer in 2020.

Thanks to the developments of information technology and advancements in modern medicine, they allow the doctor and radiologist can visualize the internal organs the individual body in two dimensions (2-D) or three dimensions (3-D) modality by using medical acquisitions, such as CT, MRI, Ultrasound. Therefore, the reconstruction and extracting the information of 2-D/3-D tissues play a vital role in the diagnosis, monitoring and surgery planning. However, organs in the human body, including heart, liver, spleen, kidney, stomach, gallbladder, inferior vena cava, artery, vein, and other organs are of complex 3-D structures (as shown in **Figure 1.2**). Additionally, their shape, size, weight, and location are different among individuals that will be changed or deformed under the impact of the disease. The segmenting and 3-D modeling of these objects, therefore, are the important pre-processing stages enable a surgeon makes a decision if a patient should be applied a surgery or not. Besides, understanding of the volume, the anatomy and vessel structure, the segments of an organ using the modeling of this organ on a computer or virtual reality enable doctors to predict the successful surgical intervention and the ability of the regeneration of tissues operated before they perform a major surgery on the specified patients.

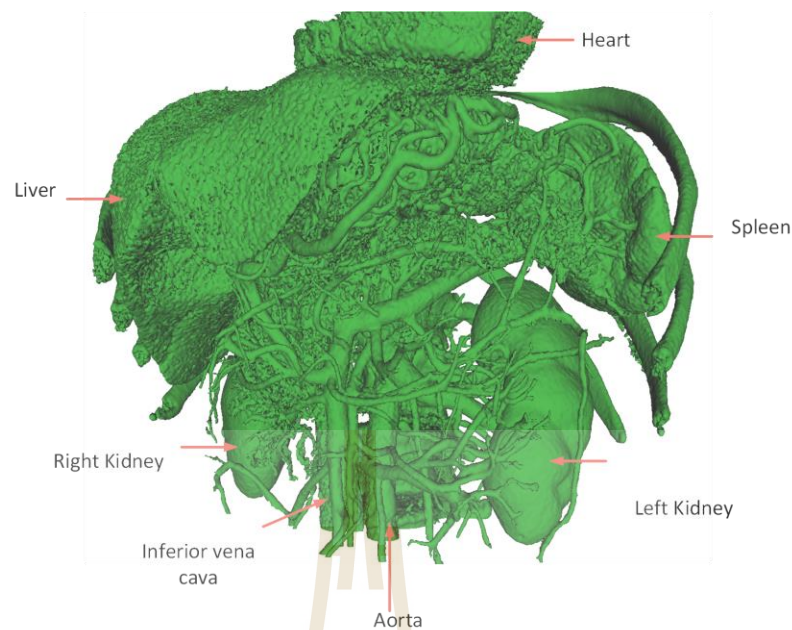


Figure 1.2 The anatomy of abdominal organs under 3-D model

1. 1. 1 Liver: anatomy and function

In a human abdomen, the liver is one of the largest organs located at the right hand of the upper body, near to the heart, and lung. The liver plays an important role in our body and functions as a filter to prevent the release of toxin into the blood. The weight of a liver varies in the gender and age of people, with an average of about 1.44 to 1.66 kg (de la Grandmaison, Clairand, & Durigon, 2001). The ability of the regeneration of liver after a partial resection surgery is one of special characteristics this tissue. The volume of liver rapidly increases within 7 first days after major surgery. After 3 to 12 months, the process of regenerating will be completed (M. F. Chen, Hwang, & Hung, 1991; Fausto & Riehle, 2005). Because of the special properties, the liver cannot be substituted by any artificial machine (László, 2014). Moreover, unlike other organs in a human body, the liver is combined from the parenchyma and a system

of the vessels. The analysis of the structural liver is mainly based on two aspects, which are morphological and functional anatomy. In terms of the morphological anatomy, the liver comprises of two independent lobes: left lobe and right lobe. Unlike the previous one, functional anatomy partitions the liver into functionally independent segments based on the internal vessel which are of obvious importance in hepatic surgery (Robin & Eduard, 2015). The process of the hepatic vascular (hepatic artery, hepatic vein, portal vein) is described as follow: the hepatic artery supplies the oxygenated blood flow to the liver; the hepatic portal vein carries the blood which contains the nutrients and toxins from all parts of digestive tract (gastrointestinal tract, gallbladder, pancreas, and spleen) to the liver; the de-oxygenated blood drains hepatic veins and inferior vena cava before coming in the right atrium (Corness, McHugh, Roebuck, & Taylor, 2006). Based on the location of hepatic vein and hepatic portal vein, Couinaud, in his seminar in 1954, classified the liver into eight independent functional segments, called by Couinnaud's classification. Moreover, each segment can be resected and implanted and able to recover after resection and the surgery on them own and do not affect other segments (Gong & Chen, 2011). The segments of the liver are shown in Figure 1.3.

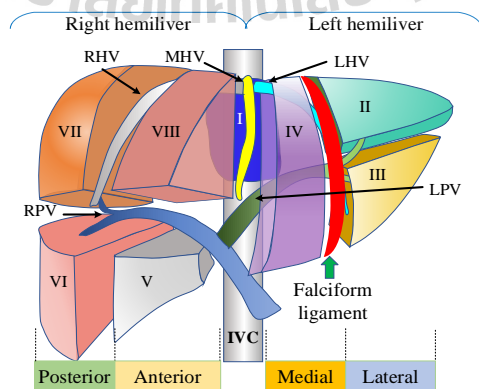


Figure 1.3 The Couinaud classification

As mentioned earlier, the liver's vital function is to filter the blood flow from the digestive tract before passing it back to the rest of the body. As a consequence, the liver can be subject to by several different diseases, including *Fascioliasis*, *Cirrhosis*, *Hepatitis*, *Alcoholic liver disease*, e.g. (Newman, 2018). Cancer is a group of various disease relevant to the unhandled growing, increasing in size and number of abnormal cells. There are several therapies applied for treating liver cancer, such as interventional radiology, chemotherapy, radiation therapy, and the combination of these techniques (László, 2014; Reitinger, Bornik, Beichel, & Schmalstieg, 2006). Among these methods, surgical intervention to remove the tumor is an efficient solution in preventing the recurrence (the re-growth of cancer after hepatectomy) of the tumor and extending the life of patients with primary and secondary stage (Martel et al., 2015).

1. 1. 2 Segmentation and simulation

The liver segmentation is defined as the delineating the liver from other tissues typically in CT or MRI image. The segmentation of CT/MRI image is commonly presented by closed contours with one slide is the liver region of interest and other slide is the background. The segmented liver contains not only the parenchyma, but also the vascular system and tumor if it exists. This process is the required step in the 3-D liver reconstruction, 3-D modeling, and simulation task. Numerous benefits of the reconstruction of accurate 3-D model in medicine has been discussed in (Lamade et al., 2000; Nakayama et al., 2017; Yeo et al., 2018). Using the 3-D liver model reconstructed from segmented liver, the surgeons can accurately calculate *the total liver volumetry* (TLV), *future liver remnant volume* (FLRV). Regarding anatomy, 3-D liver model is beneficial in determining independent segments, as well as in recognizing the *location of vessel* of the liver. For tumor and vessel detection, segmentation of liver is

one of the first and most significant requirements. In surgical planning, using of 3-D liver model enables to efficiently compute the positional relationship between the *vascular branch and tumor*. As reported by (Lamade et al., 2000), in comparison with 2-D CT image, 3-D model reconstruction of the liver increased the precision in tumor localization and the target area of the resection proposal were improved up to 37% and 31 %, respectively. Besides, it substantially contributed to reducing amount of time required to plan the surgery. Nowadays, 3-D simulation has become more popularly for *training* and supporting for clinicians in *practicing* new techniques (Agha & Fowler, 2015).

There are several different factors that influence the post-operative liver function, such as the minimal volume of the future liver remnant, patient's age, diabetes, chemotherapy-associated injury, operative blood loss and cholestasis. Among these factors, the risk of insufficient volume of liver is the most popular reason leads to post-operative liver failure. It is a prominent cause of death after major hepatic surgery in patients (Loffroy et al., 2015). In surgical intervention, the lower of risks in surgery, the higher the survival rate. To remove the tumor from the liver and guarantee the regeneration capacity, for example, the median of FLRV mass after a resection surgery is 25% (range from 15% to 40%) of TLV. This rate increases up to 50% (range from 25% to 90%) in cirrhotic, depending on the stage of the disease and the patient age. For transplant surgery, the minimal FLRV for living donor liver transplantation (LDLT) is 40% (30-50%), whereas the accepted graft body weight ratio was 0.8-1.0% (Ben-Haim et al., 2001) (or 0.6-1.2 (S. Breitenstein, C. Apestegui, H. Petrowsky, & P. A. Clavien, 2009; Clavien et al., 2010; Clavien, Petrowsky, DeOliveira, & Graf, 2007; Gotra et al., 2017; Ribero et al., 2007)). Most surgeons concurred that, the major hepatic resections on the

livers whose volumetry is below these thresholds may potentially put patients to liver insufficiency or small/large for size syndrome. In some special case, a novel pre-operative strategy referred as the portal vein embolization (PVE), is applied on patients before a major surgery. This procedure aims to reduce or block blood flow to abnormal regions and increases the size of the remnant liver volume (Clavien et al., 2010; May & Madoff, 2012). This process is generally re-evaluated after 3 to 4 weeks to assess the growth of the liver volume and hypertrophy (E. K. Abdalla et al., 2006). If a volumetry of the liver after applied PVE is above thresholds, patient is eligible to an actual surgery, otherwise, another therapy is considered.

Due to the requirements of the minimal liver remnant previously mentioned, the accurate measuring of the liver volume has substantially contributed to a successful surgery. There are several approaches have been proposed for calculating the TLV and FLRV. Based on the body surface area of patient, Vauthey et al (Vauthey et al., 2000) proposed a method for estimating the TLV as follow,

$$TLV (cm^3) = 706 \times SBA + 2.4, \text{ where } SBA, \text{ the body surface area (in } m^2) \text{ was computed in previously study (Mosteller, 1987).}$$

This formula has been considered as the standardized estimation for comparing the FLRV between other patients. Some other methods for predicting based on *SBA* and biological metrics were also introduced in (Vauthey et al., 2002). Most of them rely on the weight or height of an individual. Alternatively, another technique based on the medical image obtained from CT or MRI modality is useful for measuring TLV (Soyer, Roche, Elias, & Levesque, 1992). It differs from the previous approaches that, this technique directly measures the size of liver volume on images. It thus requires the contour of the liver manually segmented by user for all slices. The set of contours

and the distance of two adjacent slices was then used to compute the TLV (Martel et al., 2015). Although, both methods have been utilized for calculating the TLV, the estimation should not be recommended in general use. An analysis of the difference between these methods on 116 patients have been reported in (Martel et al., 2015).

In addition to assessing TLV, the safety and efficiency of a surgical resection also depend upon the determining of the positioning of portal vein branch (PVB) in whole liver as well as the PVB in tumor. It has been established that, the liver is divided into eight-functional independent segments, depending on the distribution of the hepatic vascular system (3 hepatic vein branches located at left middle and right slide; and 2 portal vein branches located at upper and lower parts). The location of liver in abdomen and its vessel system are illustrated in **Figure 1.4**.

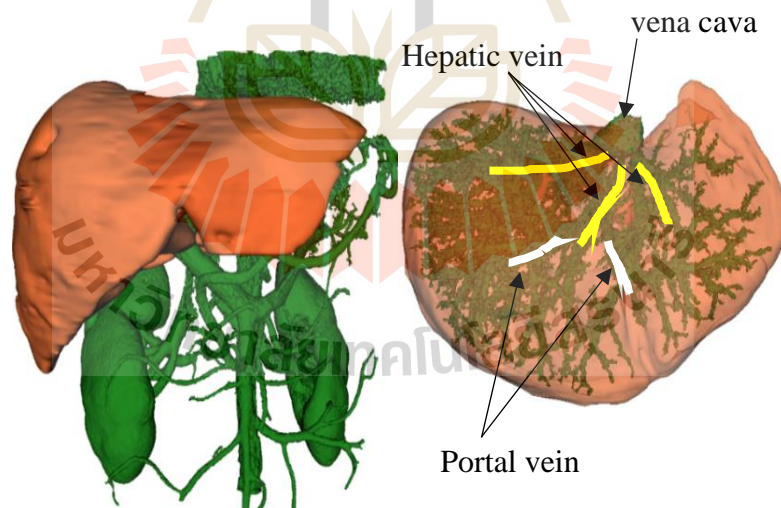


Figure 1.4 The segmentation of the liver in abdominal CT

(The liver is shown in the flesh color (a) and two main its vascular systems are drawn in yellow and white color (b))

Regarding the role of simulating surgical planning, using 3-D reconstruction model for indicating hepatectomy has become a standard in surgical training and maintaining patient's safety. A notable quote words stated here is "*Simulation is a technique not a technology - to replace or amplify real experience with guided experiences that evoke or replicate substantial aspects of the real world in a fully interactive manner*" (Gaba, 2004). In training, simulation enable trainees and experts to learn advanced methods and practice themselves on liver models. During the simulation procedure, they can immediately recognize mistakes and re-perform operations until it is satisfied. In real surgery, the simulation of the liver on specified patient allows clinicians to plan a complicated and predict preoperative risks. Additionally, it is also considered the best option in sharing visual information of the liver's anatomy as well as vital anatomic landmarks, among members in surgery team (Oshiro et al., 2015). It is reported that, lacking of the communication between surgeons may lead to 43% surgical errors (Agha & Fowler, 2015). Recently, there are several 3-D liver surgery simulation systems have been developed in advanced countries, especially Japan. Among of these systems are: OVA (Hitachi Medical Corporation), SYNAPSE VINCENT (Fujifilm Medical), Ziostation (Ziosoft) and VitualPlace (AZE) from Japan; HepaVision (Mevis) from Germany and VR-Render (IRCAD) from France (Mise et al., 2013).

In summary, there is an indirect but notable relationship between the segmentation, 3-D simulation task and surgical planning of the liver. An efficient segmentation of the liver leads to the accurate of liver volumetric measurement. As a consequence, a an efficient 3-D visual simulation leads to a significant improvement of operation planning in liver surgery (Gotra et al., 2017).

1.2 Motivation

In traditional surgical planning, the surgeons used a series of 2-D gray-scale images acquired by *CT scanner*, *MRI*, or *Ultrasound* as an important information channel for the pre-operative volumetric analysis of livers. However, 2-D images neither sufficiently provide the depth in view nor the correspondence between liver and adjacent organs, as well as the volume of organs and the structure of vascular system. By using a stack of 2-D images, a 3-D liver model can be rendered by several different approaches, including *Multi-planar*, *Surface (Contour based surface reconstruction, Isosurface Extraction based on Marching Cube)*, *Volume representation* (T. S. Kumar & Vijai, 2012). It is worth to note that, the reconstructed 3-D model comprises not only the liver but also a number of surrounding tissues, such as heart, kidney, spleen. Therefore, the segmenting of liver in 2-D images to separate the liver and vessel system from other surrounding structures, is typically considered as the first step of toward computer-aided diagnostic and intervention. Generally, the contours of the liver in 2-D images are manually extracted by radiologists using a graphical user interface tool. It depends on the area of the body imaged and the radiologist's setting about the slice thickness, the number of slices in CT images commonly varies from 100 to 500. This number can reach up to 2000 slices for a fully body scanning procedure (Pescia, 2011). Therefore, one of the most shortcomings of the manual segmenting of liver is significant time-consumption since the radiologist need to draw liver contours in all slices. This makes the segmentation more subjective and generally not reproducible. Due to limitations previously mentioned, the building of an effective and accurate segmentation, modeling, and simulation of the liver from medical images are very useful for both surgeons and patients with or without underlying liver disease.

In recent decades, LDLT is the best choice for treatment with patient in end-stage. By the way, a proportion of disease liver could be replaced by the one from donor. Beside some requirements of the health screening, such as blood testing, medical evaluation, the risks of complication of liver, i.e. liver disease, incompatibility of graft size, are also excluded (Gong & Chen, 2011). For example, the FLRV greater than 30% is safety for donor, while the graft body weight is about 1% for recipient. Moreover, it is mentioned that (Namgoong et al., 2020; Schukfeh et al., 2018), the shape of graft will affect to outcome of a surgery in LDLT with infants. Thus, the pre-operative estimation of GV is essential in finding suitable donor. Another important factor in hepatectomy is, to retain the recovery ability of remaining liver, the resection should reduce the blood losing. This means that the cutting path must parallel to hepatic veins and maintain portal vein(Gong & Chen, 2011). Thus, a method for segmentation of liver into independent functional area is critical for the success of surgery.

1.3 The purposes

Motived by benefits and challenges above, and in an attempt to assist the radiologist and surgeon in building 3-D liver model and 3-D hepatic surgical planning simulating of liver on computer, the expected purposes of this study are two folds. Firstly, the liver will be segmented and presented under a set of 2-D contours; then the 3-D liver model can be reconstructed; second, the surgeons would use the information of the location, and surface of the liver for modeling and simulating an operation. Lastly, the segmentation of liver into segments allows surgeons plain a surgery. In order to achieve these goals, the thesis focuses on solving following issues:

- Building a method for extracting features of liver region from abdominal CT scan based on the probability map; applying a local information-based model for enhancing the probability map; improving the efficiency of the graph-based model in binary classification; proposing a liver anatomy-based technique to refine the segmentation result. After segmented into 2-D contours which separate liver and surround tissues, the 3D model of liver was then reconstructed in high resolution.

- Having 3D model of liver, the functional segments of liver were obtained by using anatomical landmarks and vascular network. Each segment has its own inflow and outflow blood by Couinaud's scheme. In LDLT, the FLVR is important. Therefore, calculating graft size in liver of donor is firstly considered to avoid causing of malfunctioning liver to donor. Given some landmarks on both recipient and donor's liver, the volume of the graft may be estimated based on spherical conformal map (SCM) and rigid body transformation. This assists surgeons to simulate on computer before performing a major surgery on real individual.

1.4 Scope of research

Although CT image has been shown advantages in medical applications, the segmentation of medical image is non-trivial because of complexity as well as the representation of multiple organs. For example, the CT image of liver may contain other objects such as heart, stomach, kidney, etc.... Some of them have similar intensity with liver. They are separated in abdominal region but will be shown overlaid in CT slice. Additionally, it can be noted that, CT liver image may contain healthy liver, liver with lesion and vascular systems.

The development of an integrated segmenting system of all parts is still a challenge. Although this study aimed at developing a method for 3-D reconstruction and surgical planning simulation, it only focuses on segmenting of *normal (healthy) liver* which used for LDLT application (see in **Figure 1.5**) and *liver in which lesions (if exist) must lay entirely inside it*. Because of the similarity of intensity of lesion region and background, the boundary between may be destroyed, it leads to the deformation of overall liver shape. Actually, the tumor and vessel segmentation are yet other different problems that are relevant to liver segmentation, specially, the tumor and vascular system are sectioned from normal parenchyma.

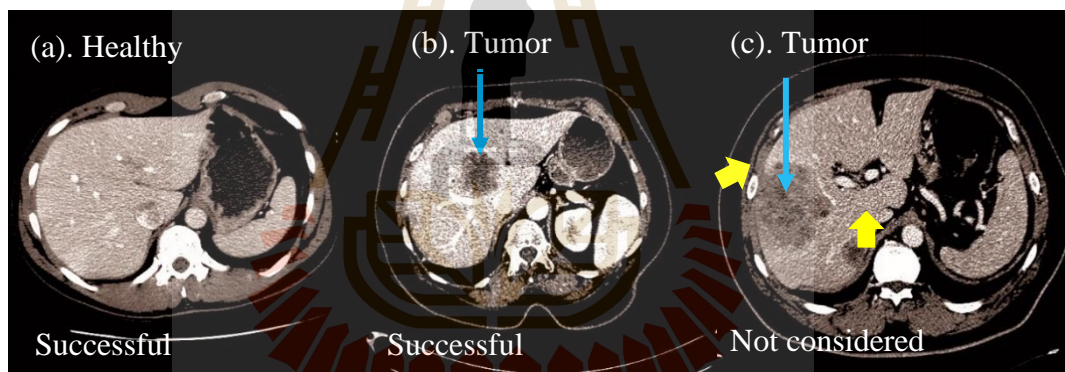


Figure 1.5 Some cases of CT image of the liver

As mentioned above, the objective of current research is to apply in LDLT. The liver in **Figure 1.5 c.** contains major tumors which is not suitable for liver transplantation, therefore it is not consider in this study. Liver in **Figure 1.5 b** has tumor enclosed by healthy parenchyma thus the boundary is retained and could be successfully segmented, but it is up to specified situation, the surgeons will have a decision which liver

is suitable in transplantation. In opposite, the liver in **Figure 1.5** a is healthy and could be considered as a candidate for transplantation surgery.

1.5 Outline of the thesis

The thesis proposal is structured in five chapters. The content of each chapter is summarized as follows.

Chapter 1 presents the objective of this work, anatomy of liver as well as basic knowledge in surgical intervention of liver. The role of segmentation, and surgical planning simulation are also discussed before entering the description of the purposes and scope of the thesis.

Chapter 2 provides an overview of the most common medical image modalities (CT and MRI), image processing, popular segmentation method. A discussion of recent approaches liver segmentation, functional segmentation, and mesh parameterization are also given in this chapter.

Chapter 3 proposes a novel framework for liver segmentation, functional segmentation of liver by Couinaud's scheme. A method for estimation of graft on donor's liver is presented in the last part.

Chapter 4 presents a discussion on the preliminary results on segmentation and 3D reconstruction using a public database. In detail, the qualitative and quantitative comparison between related approaches are evaluated based on five errors metric and time-consuming.

Chapter 5 gives a conclusion in strong/weak points of the proposed methods and proposes future works.

CHAPTER 2

LITERATURE REVIEW

This chapter begins with an overview of medical image and basic image processing techniques that utilized as the pre-processing, post-processing as well as a crucial process in medical image segmentation, particularly in liver segmentation. They are organized as follows: The overview of medical imaging modalities is shown in section 2. 1. The filtering algorithms that were applied to reduce noise and preserve edge of objects in image, morphological operator, common texture features, such as Gray-level Co-occurrence Matrix (GLCM), Local Binary Patterns (LBP), and basic methods for general segmentation image are presented in section 2. 2. In the section 2. 3, state-of-the art methods for liver segmentation are reviewed and criticized to find out the most suitable way for the objectives of the thesis. Numerous techniques for representation, and re-processing are given in the section 2. 4. Section 2. 5 surveys recent literature on major approaches to functional segmentations. Section 2. 6 gives brief description of mesh parameterization of liver. Section 2. 7 presents the liver surgical simulation.

2.1 Medical imaging

The human abdomen is structured by a number of 3-D complex tissues, most of them are inside the body and take most crucial roles to human life. Once these organs are malfunctioned, the diagnosis and treatment of diseases of them are the challenges with radiologists and surgeons. To tackle this problem, the ability of the observation internal organs inside the body is the critical condition. The advancements of the modern medicine and the developments in electrical device have allow to actualize this ability in practice by constructing images of organs and show them in monitor. By this concept, the medical imaging as a non-invasive technique have been used to acquire the image of organs inside body without opening up the body. There have been a number of medical imaging techniques with their own risks and benefits have been developed and applied in clinics during recent decades. Some of them are Computed tomography (CT), Magnetic Resonance Imaging (MRI), Ultrasound (US), Positron Emission Tomography (PET), Single Photon Emission Computed Tomography (SPECT)(Ganguly, Chakraborty, Balitanas, & Kim, 2010). Each of them provides different medical information about tissues being studied or observed related to possible disease, injury, or the effectiveness of medical treatment. Two most common medical imaging modalities and their benefits/risks are presented below.

2.1.1 Computed Tomography

X-ray, commonly referred as Röntgen radiation, have been discovered by a German physics professor Wilhelm Röntgen in his experiment in 1895. Due to the ability of the passing through several different matter, x-ray have been used in many fields of medicine and physics. In medicine, X-ray is used in taking images of tissues inside the human body, this technique is called Computed Tomography or Computer

Axial tomography (CAT). CT has been first introduced by Hounsfield et al in 1972 (Hounsfield, 1973), it uses special X-ray taken from different angles to capture detailed image. The process of a CT scanner can be described as follows: The x-ray passes through the body of the patient in many different directions, a detector or multi-detector located opposite site will record this signal and store them as a temporal “image”. A computer then combines these “images” into a completed image, referred to as a slice. A motorized table will move the patient forward to continue to capture another slice. The number of slices in a CT image depends upon the numbers of the detector and radiologist’s configuration (Sunder, Howard, Kyoko, Wolfgang, & David, 2019). The CT data are generally saved in the matrix format.

Due to the advantages of the CT scan technique, it has become increasingly popular in clinical practices over recent years. It is well-known that, the CT image allows the radiologists to delineate several different tissues based on the linear attenuation coefficient of the radiodensity after X-ray passes through them, using a quantitative scale (called the Hounsfield scale or CT number) (Hounsfield, 1973). The Hounsfield scale is then renormalized and scaled in a Hounsfield Unit (HU) scale. Assume the radiodensity of distilled water (μ_{water}) and the air (μ_{air}) at standard pressure and temperature (SPT) are 0 HU and -1000 HU, respectively. The HU scale of a linear attenuation coefficient (μ) is a linear transformation defined as (Kalra, 2018)

$$HU = 1000 \times \frac{\mu - \mu_{water}}{\mu_{water} - \mu_{air}}$$

Table 2.1 Examples of Hounsfield Units (Wilson, 2005)

Tissues	The average CT number or HU
Bone	700 to 3000
Clotted blood	80
Liver	40-60
Fresh blood	55
White matter	46
Gray matter	43
Muscle	10 to 40
Kidney	30
Cerebral spinal fluid	15
Water	0
Fat	-50 to -100
Lung	-500
Air	-1000

The HU values shown in **Table 2.1** approximately varies from -1024HU to 1368HU depend upon the density of tissues. The CT number of the air is -1000HU because it is the least dense structure. The soft tissues are higher density than water, whereas the bone is the highest density on the CT image. Furthermore, most digital image detectors in the advanced CT scanner can produce images with 4096 different gray-tones (from -1024 HU to 3071 HU). However, the human eye can approximately discriminate around 30 gray-tones (Wilson, 2005). To highlight for a tissue of interest

in the original image, a process based the HU value, called by the windowing, is applied. It aims to increase the image contrast of this tissue and eliminate the irrelevant areas by cropping the “view” of CT number and maps it into a gray-scale intensity image, as seen in **Figure 2.1**. This process defines two parameters referred as window width and window level. The first parameter is the range of CT number to be displayed, whereas the second parameter refers the mean (the middle) of CT number. Accordingly, HU values of tissue that are not in the range of the predefined window are set to black, if these values are less than the window, or white if they are greater than the window. The soft tissue in abdomen is set by “soft tissues-window” (window width, ~400; window level: 30-50). Regarding the liver CT image in abdomen, the values of window width and level may also be inspected in range (100-150) and (70-80), respectively, meanwhile the inspection of bone using “bone window” (width,~ 2000; level, ~600) may useful in detecting pathologic within the abdomen and pelvis (Baumgarten, 2006; Larbi et al., 2018; Sahi et al., 2014). The differences of the contrast of the CT liver image after applying the windowing process are demonstrated in **Figure 2.2**.

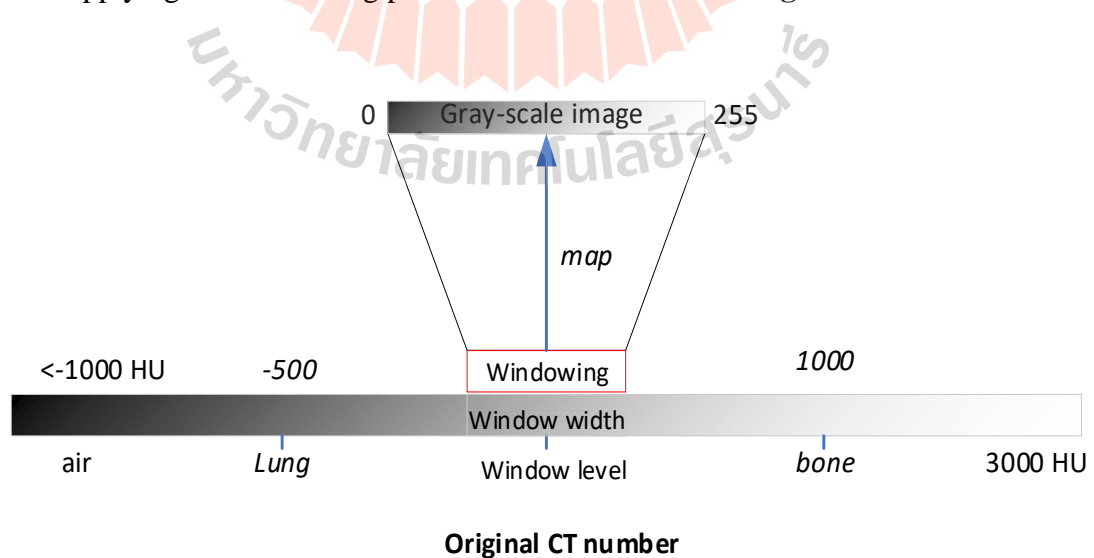


Figure 2.1 The windowing of CT image

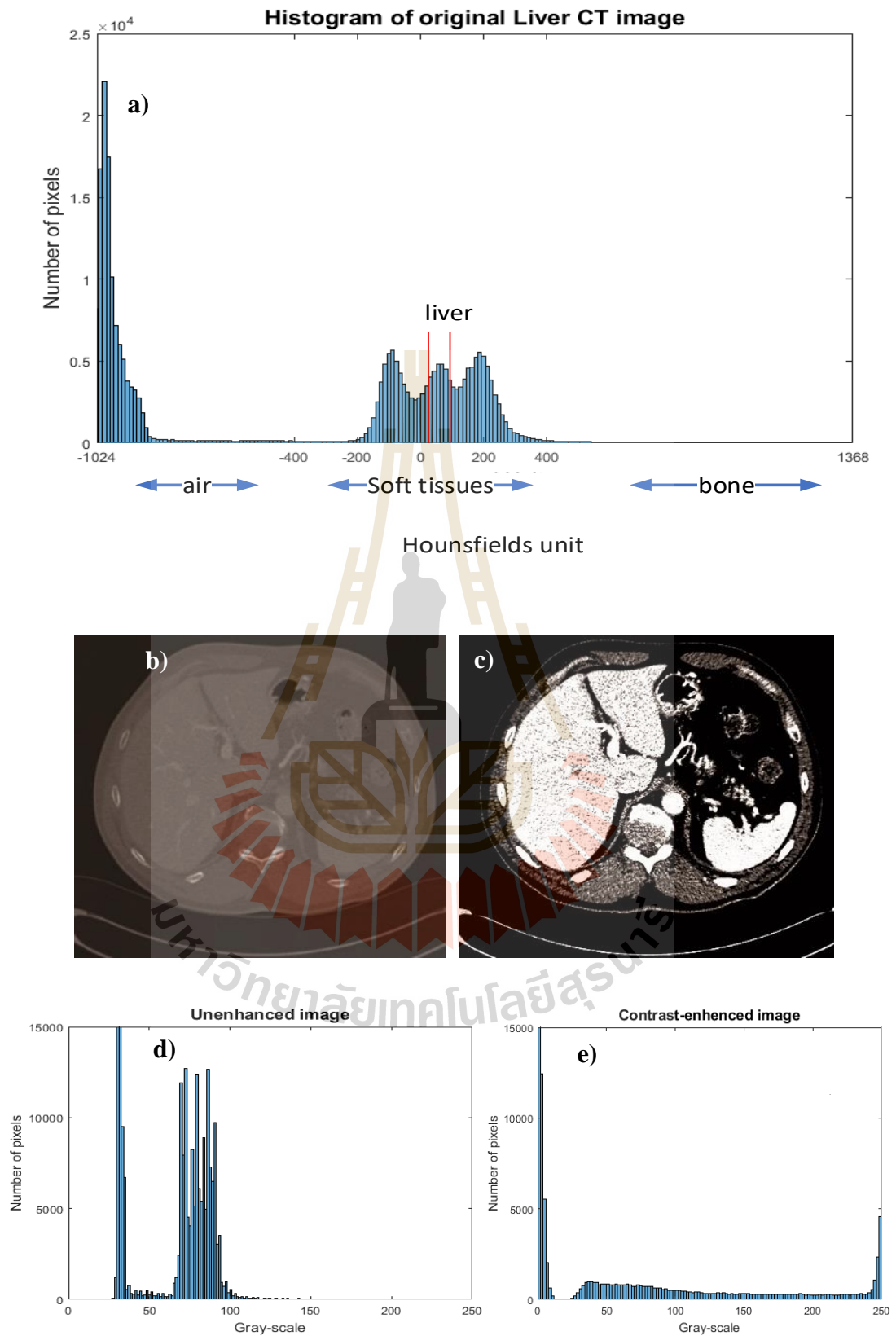


Figure 2.2 The distribution of CT number

(Soft tissues and original liver in CT image is shown in (a). The unenhanced image, contrast-enhanced image (with window width=150, window level=88) and their histograms are shown in (b), (c), (d) and (e), respectively)

2. 1. 2 Magnetic Resonance Imaging

It differs from CT imaging. Magnetic Resonance Imaging is medical imaging technique for creating images by producing a strong magnetic field surrounding the body and radio waves. Under a powerful magnetic field, the magnetic direction of atoms in the body will be realigned. After that, a radio wave will spin them in an opposite direction. Once the radio wave is turned off, atoms will return to their original direction. Based on the emitting energy from the changing of magnetic field, the physician can identify tissue types.

Applying each technique in patients primarily depends on the patient's case history, the radiologist's target and type of tissues being imaged. Nonetheless, it is worth noting that, there is no the best modality for all cases. Based on the analyzing of risks and benefits of imaging modalities, the radiologists and surgeons will propose an appropriated technique to capture images of organs. Some advantages and disadvantages of two techniques are shown in **Table 2.2**.

Table 2.2 A comparison between CT and MRI technique

Feature	CT	MRI
Technique	Use X-ray Radiation	Use powerful magnetic and Radio-wave
	Considerable cost	Costlier than CT scan (about twice)
Result	Used for capturing of the bone fractures, tumors, cancer monitoring, finding internal bleeding	Provide a detailed image of soft tissues (herniated disks torn ligaments soft tissue issues)
Risk	Harm to unborn child The gravity from a small radiation from CT scanner	The loud noise from closed system The increase of the temperature in patient's body The claustrophobia
Benefit	Painless Quickly	Painless Provide good detail of tissues
Time	5 - 10 minutes	10 minutes to 1 hour

(Jason & Stacy, 2017; Richard & Goergen, 2018; Sunder, Howard, Kyoko, Wolfgang, & David, 2018; Sunder et al., 2019).

Two examples of CT, MRI images illustrated in **Figure 2.3** show the differences in appearances between two modalities.

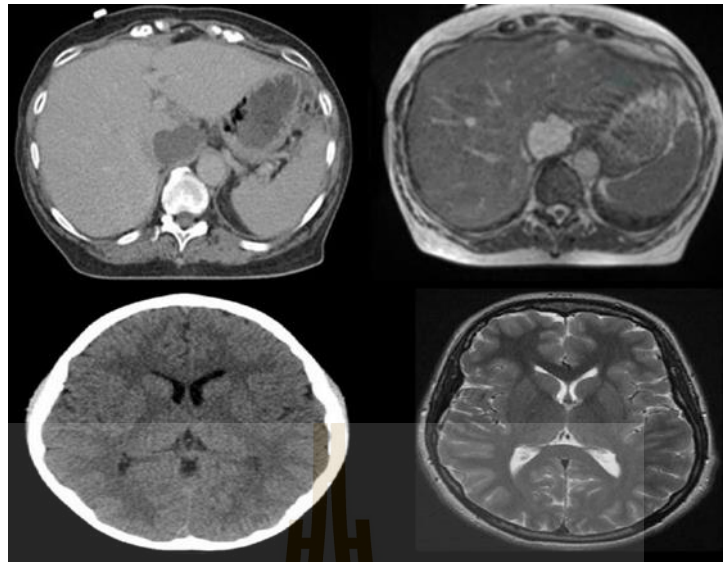


Figure 2.3 The CT and MRI image of liver, brain

(U. Kishan & Lee, 2016)(Datar, M., & Stebbins, 2019)

2. 1. 3 Digital Imaging and Communications

Due to the differences of the medical equipment from various manufacturers, a medical image of individual recorded by a specified scanner from one vendor may be incompatible to that by another scanner. Digital Imaging and Communication in Medicine (DICOM), developed by the American College of Radiology (ACR) and National Electrical Manufacturers Association (NEMA) in 1993, is the special standard for storing, printing, transmitting (Bidgood & Horii, 1992; R. N. Graham, Perriss, & Scarsbrook, 2005). During recent years, this format has been conformed by many medical imaging modalities, such as CT, MRI, mammography, etc. The header of DICOM file format contains not only the image data but also various important information relevant to the patient, study, physician, and image description. An example of DICOM header file of CT image is given in **Table 2.3**.

Table 2.3 The important information in DICOM head file

Patient	Study	Physician	Image
Accession number	Study date/time	Referring physi-	Image type
Patient's name	Series date	cian's Name	Image date
Patient ID	Study description	Performing physi-	Image time
Patient's Birthday	Series description	cian's Name	Image number
Patient's sex	Study ID	Name of physi-	Rows, Columns
Another patient ID	Study instance UID	cian(s) reading	Pixel spacing
Patient age	Series instance UID	study	Slice Thickness
		Operator's Name	

In clinical practice, to track the patient's history, all medical images relevant to this patient are stored. Each study corresponds to medical image technique (CT, MRI, Ultrasound) have been applied on the patient. Generally, each study may contain multiple series (axial, coronal), for example, the radiologists can use a CT scanner to capture various tissues of the same individual. Thus, each series should include many images, in which information of organs is present by numbers. The hierarchy of DICOM is divided in four levels, i.e., patient information, study information, series information and data image (Bidgood, Horii, Prior, & Van Syckle, 1997). An illustration of a common structure of DICOM is shown in **Figure 2.4**.

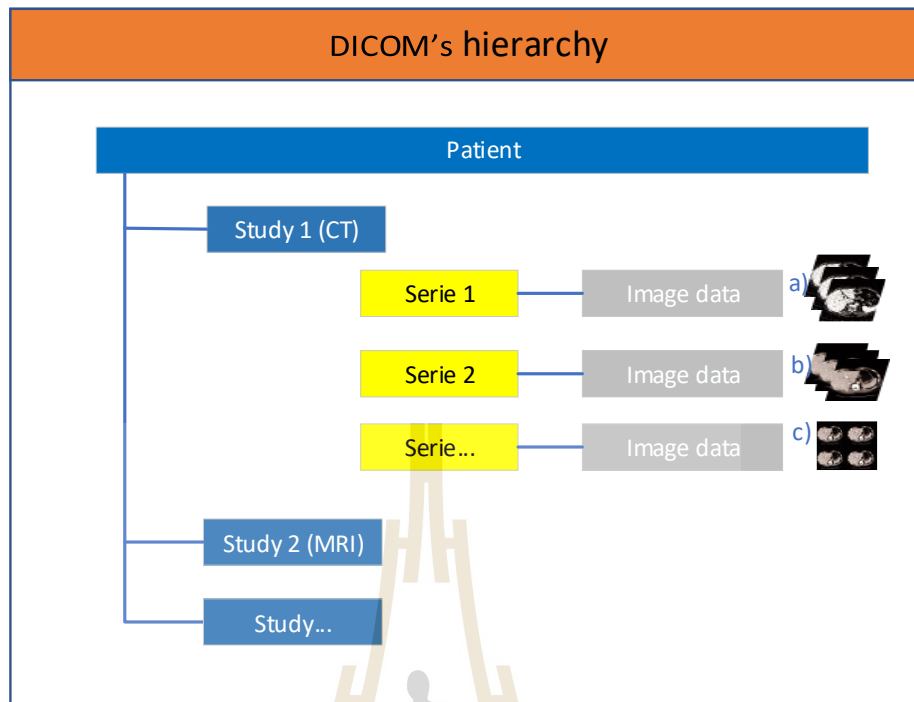


Figure 2.4 The organization of a DICOM

(The image data is presented by multiple images (a, b) or multiple-slices image (c))

2.2 Digital image processing

To have a better understanding about techniques that recently used for liver segmentation, definitions and basic knowledge of image processing and segmentation methods are presented. Due to the limitation of scope of this thesis, it only summarizes the most popular methods that were directly/ indirectly included into research related to liver segmentation. More details on each method were found in original studies listed in references.

2. 2. 1 Digital image

Image processing is referred as a set of processes that used for enhancing, analyzing, and extracting of useful information from image to apply in other fields, such as art, medicine, education, astronomy, etc. Nowadays, most of such manipulations are generally performed on a computer or other electronic devices. An image is first loaded into memory of the computer. It is then processed to make useful information associated with that image. Due to resource limitations, a computer can only present information under numbers with finite precision. Therefore, an image must be discretized to be presented digitally, a such image is called by the digital image (da Silva & Mendonça, 2005).

A digital image is defined as a 2-D function $f(x, y)$ of two discrete spatial variables x, y . In gray-scale image, the magnitude f at a given point shows the variation of the intensity of the image at that point. For a color image which contains three channels (Red, Green, Blue), the magnitude of f composes f_R, f_G, f_B which referred as the value of red, green, blue color in the image. Generally, the size of an image is limited by a pair (M, N) which indicate for the height and width of the image.

2. 2. 2 Fourier transform

An alternative image presentation based on frequency has been widely used in image processing. This technique has been derived from Fourier transform of two variables (Gonzalez & Woods, 2002). Fourier theorem stated that any periodic function can be analyze as the sum of sine and/or cosine function of different frequency (called Fourier series). Instead, the non-periodic function can be also expressed by the integral of sine and/or cosine for all frequency. This presentation is referred as the Fourier Transform.

Assume that $F(x, y)$ is the continuous function defined on spatial domain of two continuous variables (x, y) . The Fourier transform of $F(x, y)$ is given by the following expression.

$$F(u, v) = \int_{-\infty}^{\infty} \int_{-\infty}^{\infty} F(x, y) e^{-i2\pi(ux+vy)} dx dy \quad (2.1)$$

where i is the complex number, $i^2 = -1$. This equation is called by the toward transform. The original of function $F(x, y)$ can be obtained from its transform by the following equation

$$F(x, y) = \int_{-\infty}^{\infty} \int_{-\infty}^{\infty} F(u, v) e^{i2\pi(ux+vy)} du dv \quad (2.2)$$

The frequency component in (2.1) is expressed as a complex exponential function that may be re-written as a combination of sine and cosine function. According to the Euler's theory

$$e^{i\theta} = \cos \theta + i \sin \theta \quad (2.3)$$

Equation has two parts: real (Re) and imaginary (Im) parts. By substituting (2.3) into (2.1), it can re-write the Fourier transform equation of continuous function under complex as follow

$$F(x, y) = \int_{-\infty}^{\infty} \int_{-\infty}^{\infty} F(u, v) [\cos 2\pi(ux + vy) - i \sin 2\pi(ux + vy)] dudv \quad (2.4)$$

The spectrum which is defined as the magnitude, and phase of transform are computed by

$$|F(u, v)| = [Re^2(u, v) + Im^2(u, v)]^2 \quad (2.5)$$

$$\omega(u, v) = \tan^{-1} \frac{Im(u, v)}{Re(u, v)} \quad (2.6)$$

where $Re(u, v)$ and $Im(u, v)$ presents for the real and imaginary component in Fourier, respectively. **Figure 2.5** shows an example of Fourier transform of a CT image.

Given a discrete function $f(x, y)$ of a digital image of size $(M \times N)$ on spatial domain. The Fourier transform of that image on frequency domain is defined by equation (Gonzalez & Woods, 2002)

$$F(u, v) = \frac{1}{MN} \sum_{y=0}^{M-1} \sum_{x=0}^{N-1} f(x, y) e^{-i2\pi(\frac{ux}{M} + \frac{vy}{N})} \quad (2.7)$$

The original image on spatial domain is inverted from the Fourier transform as the expression:

$$f(x, y) = \sum_{y=0}^{M-1} \sum_{x=0}^{N-1} F(u, v) e^{i2\pi\left(\frac{ux}{M} + \frac{vy}{N}\right)} \quad (2.8)$$

where u, v, x, y are discrete variables, in that $u, x \in [0, M - 1], v, y \in [0, N - 1]$.

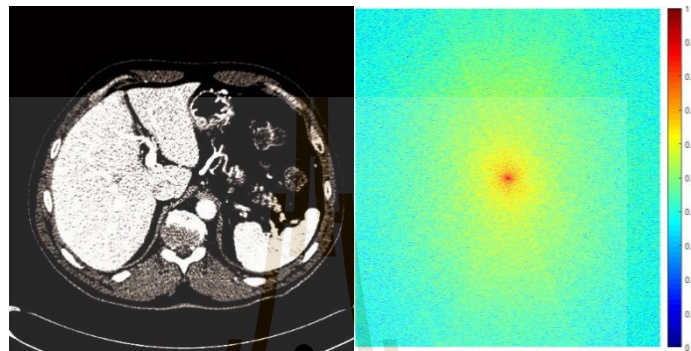


Figure 2.5 An example of Fourier transform

(The original image is showed in the first column. The magnitude of frequencies extracted from Fourier transform is showed in the second column)

Fourier transform has been widely used in various applications of digital signal and digital image processing. In image processing field it can be used in image enhancement, image filtration, image restoration, image compression (Smith, 1997). In medical image processing, Fourier transform can be applied in low-pass filter that reduce noise of CT image (Mihaylova & Georgieva, 2016; Tang & Tang, 2012). Shape descriptor based on Fourier transform can be used to smooth contour (Gloger, Kuhn, Stanski, Volzke, & Puls, 2010). In signal processing, Fourier transform is utilized to compress the signal of the audio.

2. 2. 3 Image processing

Generally, digital image processing can be grouped in to three level: low-level, middle-level, and high-level. Processing of image at low-level invokes the basic processes to enhance, reduce noise, smooth and sharp image. Most algorithms in this group require input images and outputs ones. The next process level refers to techniques for extracting information present in an image. It requires the input that are images, whereas its output returns features, segmentations, classifications of objects in image that characterized by feature vectors, contours, edges, segments, or what the object is. The higher and more difficult level, the higher-level processing, that are used for analyzing the meaning of an image.

There exists consistency among levels of processes that ensures that an efficiency process in lower level will improve the accuracy for next level processes. The windowing process mentioned in section 2. 1 is an example of this statement. As a consequence, the segmentation in CT image is not an exception. Next items in this section will present some techniques of filtering, morphology operation, feature description before coming to approaches for basic segmentation.

2.2.3.1 *Filtering*

The image data contains not only the useful information that describe objects but also noise (referred as noise image) which is not easy to remove from image. Noise image normally comes from the image acquisition (sensor), transmission, storage process. It is recognized by the abrupt variation of the intensity at a few regions or whole image. Most noise image can destroy the structure of image, as well as cause lacking important information. It leads to low accurate image processing. The best solution for reducing/removing noise is the detection of noisy model. Based

on the distribution of image noise, the noise model can be classified into the following groups: Impulse noise (salt and pepper), Gaussian noise, Rayleigh noise, Erlang noise, Exponential noise, Uniform noise, Periodic noise (Gonzalez & Woods, 2002).

The filter is one of popular methods used for reducing/ removing noise. For example, the median filter is used to eliminate a noise image of salt and pepper, whereas the Gaussian filter is used for denoising in Gaussian noise. In another aspect, the filters in frequency domain are more efficient in resolving periodic noise model.

In many image processing applications, the distinction of objects in adjacent regions in image is equivalent to detecting boundary (edge) between those objects. As their properties, filters can be used to smooth image, such as mean filter, Gaussian filter. They are isotropic filters that do not take into account local information while reducing noise. This means that the kernel size of filter is independent of the underlying pattern direction. Consequently, isotropic filters reduce the detail and blur the boundary. Inspired by the heat diffusion, Perona et al (Perona & Malik, 1990) introduced an efficient tool for smoothing image without removing details, also called Perona–Malik diffusion (see in **Figure 2.6**). The main idea of this method can be summarized as follow.

Assume $I_{i,j}^t$ be the intensity of pixel at location (i, j) at time t , the updating of that pixel at $t + 1$ is given by

$$I_{i,j}^{t+1} = I_{i,j}^t + \varepsilon \sum_{z \in \{Upper, Lower, Left, Right\}} [c_z I_z^*]_{i,j}^t \quad (2.9)$$

where $\varepsilon \in [0, \frac{1}{4}]$; $I_{i,j}^{*t}$ is the intensity of the pixel at the upper, lower, left, right of $I_{i,j}^t$; $c_{i,j}^t$ is the conduction coefficient that is defined as the follow.

$$c_{i,j}^t = g(|I_{i,j}^{*t}|) \quad (2.10)$$

The function $g(\cdot)$ is given by two the following formulate.

$$g(|I_{i,j}^{*t}|) = e^{-\left(\frac{\|\nabla I_{i,j}^{*t}\|}{K}\right)^2} \quad (2.11)$$

Or

$$g(|I_{i,j}^{*t}|) = \frac{1}{1 + \left(\frac{\|\nabla I_{i,j}^{*t}\|}{K}\right)^2} \quad (2.12)$$

with K is a threshold, $\|\nabla I_{i,j}\|$ is the magnitude of gradient vector at pixel located (i, j) .

A modified version of (Perona & Malik, 1990) has been introduced in (Whitaker & Xinwei, 2001). It is based on the calculating of the level-set curvature to control the conduction coefficient. According to the authors, this method is more aggressive than anisotropic diffusion at enhancing and preserving edges, and it less sensitive to the edge contrast parameter.

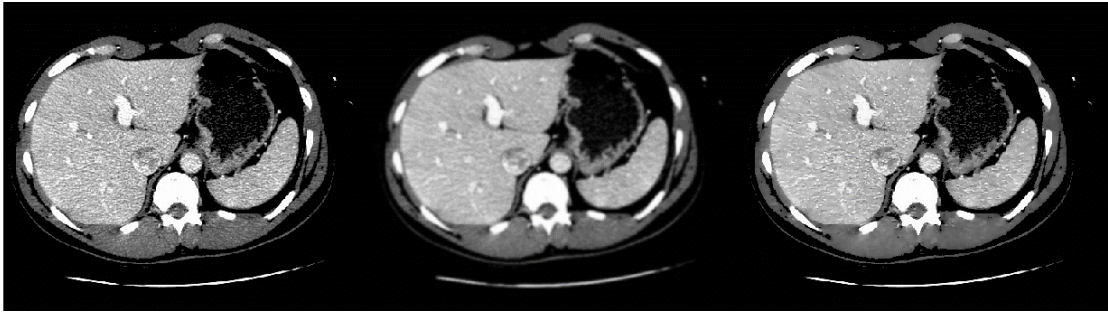


Figure 2.6 An example of smoothing image

(The original is shown in the first column. The second and third column present filtered images using isotropic (Gauss filter) and anisotropic diffusion filter, where $t = 10$, $K = 20$ and g is defined as (2.11))

2.2.3.2 Morphological operators

Morphological operators are collection of techniques for image processing based on the ordering of pixel values. They can be used for both binary and grey-scale image. The input of morphological operators is an image, structure element and a set of operators, such as intersection, union, complement and inclusion. The structure element that serves as the kernel of an operator consists of numbers located in a shape of disc, square or cross. The center of structure element is placed at its origin.

In terms of segmentation, most morphological operations have been used in post-processing as a simple method refinement segmentation result, such as dilation and erosion operator. The dilation operator is commonly applied to fill holes, for example holes caused by vessel system in liver as well as connect broken line. Whereas erosion is useful for removing isolated pixels. **Figure 2.7** and **Figure 2.8** demonstrate the efficiency of dilation and erosion operator.

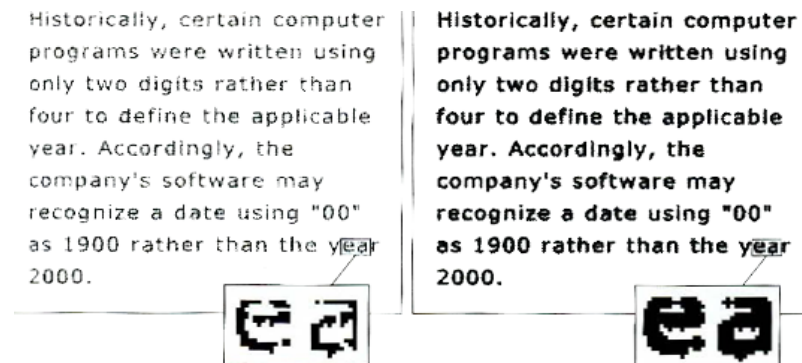


Figure 2.7 Dilation operator

(The broken text (left) can be recovered by dilation process (right) (Gonzalez & Woods, 2002)).



Figure 2.8 Erosion operator

(The first column is the input image. The second one shows the result of erosion. The last column shows the dilation of image in the second column (Gonzalez & Woods, 2002). Both structure element size of dilation and erosion are set with the same structuring element).

2.2.3.3 *Texture feature*

Extraction and descriptor information in through texture features presented in image play a crucial role in digital image processing tasks. Depending on the kind of applications, information in image can be extracted as global or local features, that convey essence information about object and serve as the basis for a variety of image processing tasks. Global feature is used to describe an image as a whole and generalize an entire as a feature vector or shape descriptor (i.e., the liver can be drawn as closed contour). In opposite aspect, local feature in image is extracted at the pixel or region level (Awad & Hassaballah, 2016). It aims to recognize or distinguish objects in image based on the difference of information of points or regions. In gray-scale image, the difference is generally presented by the variation of intensity that characterize for each object. Unfortunately, due to noise image, low contrast in intensity, the extracting of global or local feature is still a challenge. In term of liver segmentation in medial image, we investigate some texture features that have been popularly used in related research. They are *Grey Level Co-occurrence Matrix*, *Local binary pattern*.

Grey Level Co-occurrence Matrix

As shown by its name, Gray Level Co-occurrence Matrix (GLCM) is used to reveal the spatial structure of texture in image. It evaluates statistics of the occurrence frequency in a pair of two pixels with the same level of gray value at a specified direction and distance (Haralick, Shanmugam, & Dinstein, 1973). GLCM is a matrix of size of $L \times L$, where L is the number of levels of gray.

An element $c_{\Delta x, \Delta y}(i, j)$ in GLCM matrix is calculated by

$$c_{\Delta x, \Delta y}(i, j) = \sum_{y=1}^M \sum_x^N \begin{cases} 1 & I(x, y) = i \wedge I(x + \Delta x, y + \Delta y) = j \\ 0 & \text{otherwise} \end{cases} \quad (2.13)$$

where $i, j \in [1, L]$; M, N are the height and width of image I ; $I(x, y)$ is the intensity of pixel at row y , column x in image, respectively. See in **Figure 2.9**.

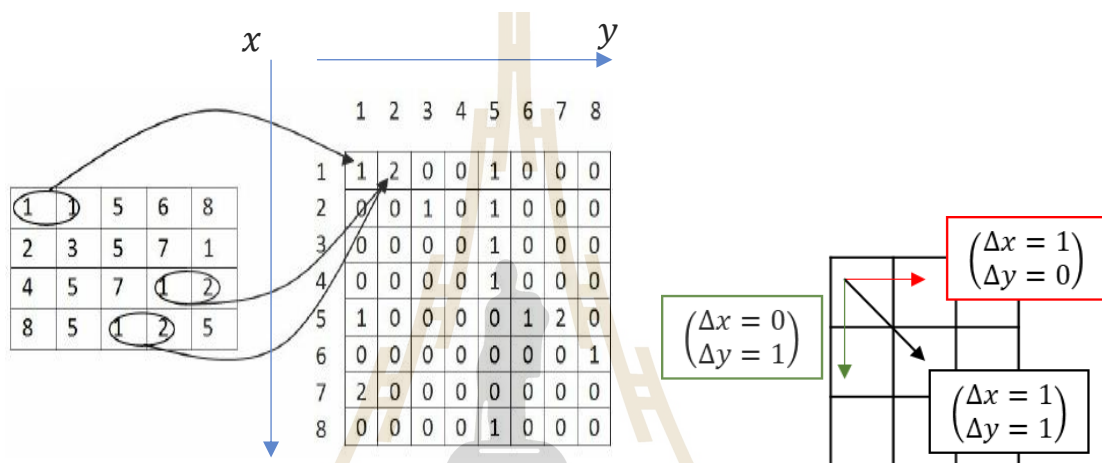


Figure 2.9 An example of computing GLCM

(with $L=8, \Delta x = 1, \Delta y=0$)

Haralick et al (Haralick et al., 1973) have suggested 14 texture features that can be extracted from GLCM matrix. They are *Angular second moment*, *Contrast* (**Figure 2.10 b**), *Correlation*, *Sum of squares* (**Figure 2.10 c**), *Inverse difference moment*, *Sum average*, *Sum variance*, *Sum entropy*, *Entropy*, *Difference variance*, *Difference entropy*, *Information of correlation* (2 features), *Maximum correlation coefficient*. Some of them specify the textural characteristics, while others present the complexity and nature of image.

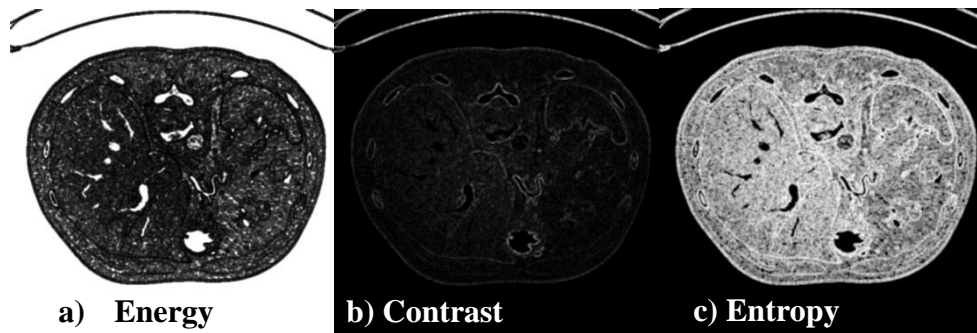


Figure 2.10 An example of GLCM

Local binary pattern

Local binary pattern (LBP) is a simple and efficient texture operator for presenting a grayscale. It is based on comparing the value of current pixel with its 8-neighbors along a circle of clockwise or counterclockwise and gives the results as binary values. Then eight-binary values are converted into decimal (ranged 0 to 255) and their histogram can be used to describe the texture image. **Figure 2.11** illustrates the determining of LBP with 3-by-3 neighbors.

The original LBP introduced by Ojala et al in 1996 (Timo Ojala, Pietikäinen, & Harwood, 1996) considers 3-by-3 neighbors in a square shape. In their improved version in 2002 (T. Ojala, Pietikainen, & Maenpaa, 2002), they have extended LBP operator by using a neighbor of different size and shape (circle, instead of square) with a non-integer radius which referred as $VAR_{P,R}$ (rotation invariant local variance), where P is the number of element in circle radius of R (as given in **Figure 2.12**). LBP is also re-written as $LBP_{P,R}$, with P=8 and R=1.

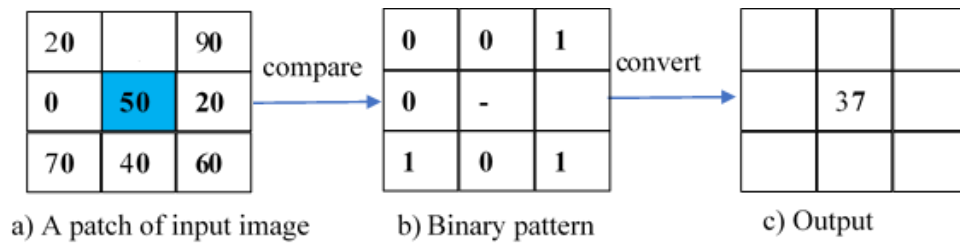


Figure 2.11 An example of LBP

(The value of current pixel (50) is compared to its neighbors values (a). The binary value (00100101) (b) is converted into decimal number (37)(c).

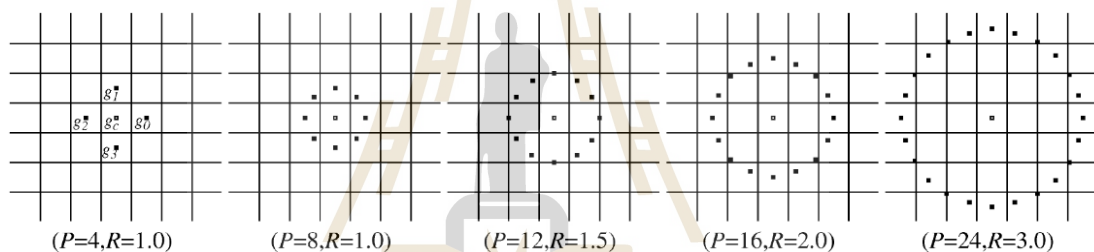


Figure 2.12 The structure of neighbors by different parameters (P, R)

2. 2. 4 Image segmentation

Over the years, segmentation image has been a main task in image processing and computer vision field due to its useful applications, particularly, object detection, object recognition and medical image processing. It is a process of subdivision an image into multiple regions base on some characteristics, such as color, intensity, boundary. The segmentation in nontrivial image, nevertheless, is the most difficult process among different digital image processing tasks. Due to the variability in shape and size of objects in image, low contrast intensity, blurred edge (boundary), overlapping between objects, segmentation is still an open problem, and the accuracy segmentation

strongly relies on many factors, such as time consumption, applied technique, field. There exist numerous methods that used for segmenting in common image. Regarding segmentation in medical image, some popular techniques are reviewed in following paragraphs before coming a discussion of state-of-art method.

Region growing

Seeded region growing was firstly introduced by (Adams & Bischof, 1994). It is a simple method for segmentation in image based on grouping pixel into a regions using predefined constrains (Gonzalez & Woods, 2002). This algorithm starts from a region which includes a given pixel, also referred as seed points, neighbor pixels are added into a list if they satisfy some criteria, such as the similarity of intensity, color. Each candidate in list is considered as a seed point for the next step. The growth of regions stops once the list is empty. **Figure 2.13** show an example of region growing in CT liver image.

Assuming I is the entire image, the goal of region growing is to partitions I into subregions $\{I_1, I_2, \dots, I_n\}$ that satisfy the following conditions

- (1) The pixel in image is segmented: $\bigcup_{i=1}^n I_i = I$
- (2) I_i is connected region, $\forall i \in [1, n]$
- (3) There is no overlap between regions: $I_i \cap I_j = \emptyset, \forall i \neq j$
- (4) Each pixel in a region must be stratified a pre-defined constrain:

$$P(I_i) = true, \forall i \in [1, n]$$
- (5) If two pixels have different properties, they should belong to different regions: $P(I_i \cup I_j) = false, \forall i \neq j$

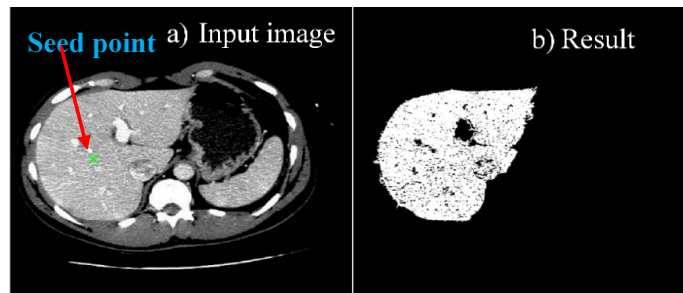


Figure 2.13 An example of region growing

Thresholding

The threshold based – segmentation method is defined as labeling of a pixel based on the comparison between intensity of this pixel ($I(x, y)$) with a threshold T . The pixels for which $I(x, y) > T$ is called by object; otherwise, this pixel is referred as background. The thresholding technique can be classified into three groups: global thresholding, local thresholding and adaptive thresholding (Gonzalez & Woods, 2002). The first group uses single or multi-threshold which is fixed or directly estimated from image in the entire image. Otsu has been known as an efficient method for estimating threshold based on minimizing the intra-class variance (Otsu, 1979). The second group, adaptive thresholding, bases on dividing original image into sub-regions, then a different threshold is applied for each sub-region. The last group only considers pixels that lie on the boundary between objects based on gradient and Laplacian operator. It enables to improve the shape of histogram as well as make histogram to be less dependent on the size of objects and background. Some examples of thresholding are illustrated in **Figure 2.14**.

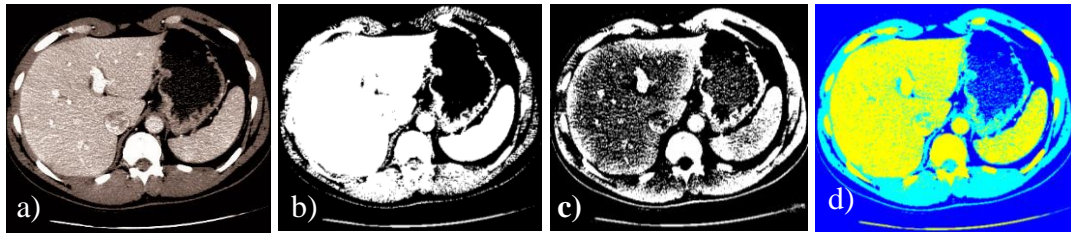


Figure 2.14 A result of thresholding

(The original image is shown in (a). the results of Otsu method with single thresholding(b), adaptive thresholding and Otsu method with multi thresholding are given in (b, c, d), respectively).

Statistical shape model

Statistical shape model (SSM) has been commonly used in many applications of computer vision recognition, reconstruction, classification. It is a useful tool for modeling shape of object based on the analyzing the normal shape variation of a class of shape (J. Graham & Baldock, 2000). This model is built from a collection of training shape set, in which each sample is characterized by a landmark vector which manually defined by experts. The corresponding between each element in feature vector is constrained for all samples in training set. A new shape is reconstructed by the linear combination of principal shape variations associated with their parameters. Therefore, in order to capture a various shape, the training set must contain enough variation. However, this leads to the under-fitting problem. To have an efficient description of shape of samples in a training set, a conventional method is applied for extracting the important/ characteristic features in dataset. It has been well-known that Principal Components Analysis (PCA) is a powerful tool that is used to represent data by projecting

them into a new space, in which the variation in original data is presented more clearly (Gonzalez & Woods, 2002).

Let \bar{s} mean shape of a training set $\{s_1, s_2 \dots s_M\}$. The feature vector of each sample is presented by $s_i = [x_1, s_2, \dots, s_N]^T$, where M is the number of samples; N is number of features; the superscript “ T ” means the transform operator of a matrix. The mean shape and covariance matrix C are given respectively by

$$\bar{s} = \frac{1}{M} \sum_{i=1}^M s_i \quad (2.14)$$

$$C = \frac{1}{M-1} \sum_{i=1}^M (s_i - \bar{s})(s_i - \bar{s})^T \quad (2.15)$$

Eigenvectors (P_j) and their eigenvalue (λ_j) associated to P_j can be computed from covariance matrix C . Let $P = [p_1 p_2 \dots p_K]$ be a matrix whose K columns corresponding to K eigenvectors, so that $\lambda_{j-1} \geq \lambda_j, \forall j \in [1, K]$ and $K \in [1, M]$. A presentation of new shape in this basis can be given by

$$s = \bar{s} + P\alpha \quad (2.16)$$

where $\alpha = [\alpha_1, \alpha_2, \dots, \alpha_K]^T$ is the parameter of the new shape.

Active shape model (ASM) (Cootes, Taylor, Cooper, & Graham, 1995) is an application of SSM, which presents a new shape based on principal component. The ASM processes image and that matches a new shape to a model. It can be described as follows:

Let s_* be the current shape (s_0 is generally the mean shape).

- (1) For each point (x) in initial shape, search in image points (y) which is the best fit to (x).
- (2) Find parameter b : $b = P^T(s - \bar{s})$
- (3) Reconstruct a new shape: $s = \bar{s} + Pb$
- (4) Update current shape $s_* = s$
- (5) Repeat from (1) to (4) until convergence

Level set method

Segmentation is defined as dividing an image into disjoint regions or objects (Gonzalez & Woods, 2002). On the other hand, it can be considered as a problem of determining closed contours of regions or objects. Level set method introduced by Sethian (Osher & Sethian, 1988) is a mathematical method that is used to implicitly describe a contour based on tracking the propagation of a surface a specified level.

Let $\phi(\chi)$ be a surface defined on $\chi = (x_1, x_2, \dots, x_n)$. The l -level set of surface $\phi(\chi)$ is given by

$$C_l = \{\chi | \phi(\chi) = l\} \quad (2.17)$$

In a special case, $n = 2$, the l -level set present a contour. The evolution of surface can be considered as the propagation of contour at time t with *zero*-level. Assuming $\chi(t)$ is the position of χ at time t , C_l in (2.17) is re-written by the equation.

$$C_l = \{\chi | \phi(\chi(t), t) = 0\} \quad (2.18)$$

The curve C_l divides surface ϕ into partitions, including internal partition consists points inside contour, external partition consists points outside contour. The propagation of surface with respect to t is represented by

$$\frac{\partial \phi(\chi(t), t)}{\partial t} = 0 \quad (2.19)$$

It has been proven that, if $f(x, y)$ is a differentiable function, the change of f can be approximated by the linear combination of its components as

$$\Delta f \approx f_x \Delta x + f_y \Delta y \quad (2.20)$$

By applying (2.20), equation (2.19) is approximated by

$$\begin{aligned} \frac{\partial \phi}{\partial \chi(t)} \frac{\partial \chi(t)}{\partial t} + \frac{\partial \phi}{\partial t} \frac{\partial t}{\partial t} &= 0 \\ \Leftrightarrow \frac{\partial \phi}{\partial \chi(t)} \frac{\partial \chi(t)}{\partial t} + \frac{\partial \phi}{\partial t} &= 0 \text{ or } \nabla \phi \chi_t + \phi_t = 0 \end{aligned} \quad (2.21)$$

where $\nabla \phi = \frac{\partial \phi}{\partial \chi(t)}$, $\chi_t = \frac{\partial \chi(t)}{\partial t}$ and $\phi_t = \frac{\partial \phi}{\partial t}$. Note that, ∇ is the gradient operator, ∂ is the derivation. Equation (2.21) gives the movement of surface ϕ at time t . χ_t is the velocity of movement. Let F be the force normal to surface, where $F = \chi(t) \frac{\nabla \phi}{|\nabla \phi|}$. Equation (2.21) is re-written as follow

$$F |\nabla \phi| + \phi_t = 0 \text{ or } \phi_t = -F |\nabla \phi| \quad (2.22)$$

The derivation of a function $f(x)$ on finite domain has following form

$$f'(x) = \frac{f(x + \Delta x) - f(x)}{\Delta x} \quad (2.23)$$

In this way, the level set equation can be approximated by

$$\phi_t = \frac{\partial \phi}{\partial t} = \frac{\phi(t + \Delta t) - \phi(t)}{\Delta t} \quad (2.24)$$

$$\Leftrightarrow \Delta t \phi_t = \phi(t + \Delta t) - \phi(t) \Leftrightarrow \phi(t + \Delta t) = \phi(t) + \Delta t \phi_t$$

By substituting (2.22) into (2.24), we have the equation for the evolution of ϕ at time $t + \Delta t$

$$\phi(t + \Delta t) = \phi(t) + -\Delta t F |\nabla \phi| \quad (2.25)$$

In image processing, the key element of level set method is under the definition of $\phi(t = 0)$ and speed function F . Generally, the initial $\phi(t)$ is given by a coast contour. Value of F can be directly obtained from the curvature measurement or the edge strength in image. For example, $F = 1 / (1 + |\nabla G_\sigma I|^2)$, where G_σ is Gaussian filter, with standard derivation of σ . **Figure 2.15** shows an example of level set method on CT liver image using initial contour of square.

The high computational cost is the most disadvantage of level set method. The reason is because the evolution of zero level set is calculated from the evolution for all the level set. In order to reducing time consumption, an improvement of original level set has been introduced in (Sethian, 1996). In this model, the processing of updating the surface at time t of zero level set is based on its neighbors. It was also known as the “narrow band approach”.

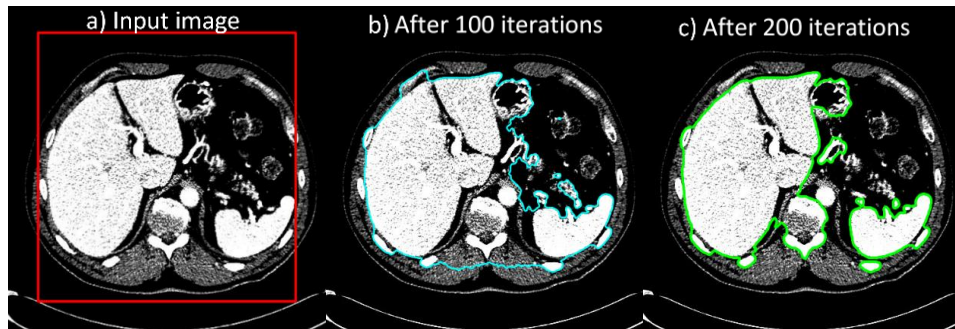


Figure 2.15 The result of level set method

2.3 Liver segmentation approaches

One of interesting applications of image segmentation, which have been extensively explored during a few decades in medical field is liver segmentation. Liver is the biggest organ in abdomen and plays a vital role as a filter to release impurities from blood. Consequently, liver is easily to prone to various disease such as hepatitis and cancer (N. M. Altarawneh, S. Luo, B. Regan, & G. Tang, 2015). Liver segmentation in CT image is crucial and necessary step for disease diagnosis, surgical planning, chemical treatment, 3D liver visualization and volumetric measurement, and treatment. It allows radiologist to detect internal structure of human body without opening body. Currently, this is one of the most common methods for modelling internal organs in abdomen because of the high signal-to-noise ratio, the high resolution, and the considerable cost. The images acquired from a CT scanner, however, also include liver and adjacent organs such as stomach, heart, and vessel. Additionally, as a 3D complex structure, the liver itself is soft and inhomogeneous; the shape and size may be change due to pathology; the intensity of surrounding organs is quite similar to liver (E. L. Chen, Chung, Chen, Tsai, & Chang, 1998; Y. Chen, Wang, Zhao, & Yang, 2009; Foruzan,

Zoroofi, Hori, & Sato, 2009; S. J. Lim, Jeong, & Ho, 2005; R. G. Mohamed, Seada, Hamdy, & Mostafa, 2017; Withey & Koles, 2007); in some CT images, the liver may lie alternately with other organs and far from main region. This leads to the low accuracy segmentation. The manual segmentation process is the golden standard for liver segmentation. However, it is tedious, time-consuming, and often performed by radiological specialists who have insights of the shape, location and size of liver; therefore, the results totally rely on the experience and skill of these experts. **Figure 2.16** illustrates some challenges of liver segmentation.

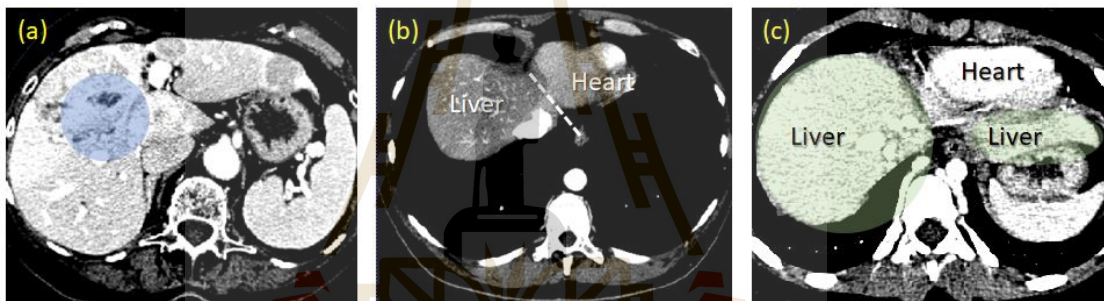


Figure 2.16 Challenges associated with liver segmentation

(Inhomogeneity of intensity in the liver region (a), fuzzy separation between liver and heart (b) and the multi-segments geometry within single slide (c). In addition, these cases exhibit different intensity ranges of liver tissue)

With increasing of the number of CT images and the need of reduction of time consumption, the computer-aided segmentation system has been widely used in more clinical practices. It handles the tasks with the same accuracy, achieves fast and accurate results and supports faster communication. However, there is no the best solution that applied for all problems. An overview of recent approaches for liver segmentation can

be found in (Gotra et al., 2017; Khan, Ahmed, Kiran, & Adnan, 2016; Luo, Li, & Li, 2014; Mharib, Ramli, Mashohor, & Mahmood, 2012; F. Mohamed, A. & Viriri, 2017; Zaitoun & Aqel, 2015). However, some of the prominent studies are reviewed here. They can be divided into groups, including thresholding, region growing, level set – deformable model and statistical shape model. More detail of these approaches is presented in below items.

2.3.1 Thresholding

Selver et al (Selver et al., 2008) proposed parallel learning and segmenting liver from abdominal CT angiography (CTA). In this work, CTA images were divided into low and high contrast groups. It made use of knowledge on the anatomy of kidneys, ribs, and livers, in combination with thresholding technique, to remove irrelevant parts and to highlight the region of interest (ROI). K-Means and Multi-Layer Perceptron (MLP) classifiers were subsequently applied to high and low contrast data, respectively, depending on their histogram appearances, based on automatic switching mechanism. Heuristic post processing was finally used to remove over-segments, while remaining errors may be manually corrected. A prior knowledge of anatomy of liver is useful for segmentation. In (Foruzan et al., 2009), authors introduced a multi-step heuristics method using thresholding and anatomy of liver. First, based location of liver and intensity of bone, initial boundary was first estimated in largest slice. The histogram of liver that has been learned from different datasets was divided into two parts. Then, a technique, called by “split thresholding” is employed to find true boundary of liver. Several basic image processing methods, such as morphology operator, filter, fill hole, smoothing filters, largest connected component, were used to refine the result. Anatomy of liver was also used in (Yussof & Burkhardt, 2009) to remove non-liver regions based

on 3D-connected component. Anisotropic diffusion method filter was applied to smooth image before building histogram of liver image. Liver was then segmented using thresholding on this histogram. Similar studies were found in (Antonidoss & Kaliyamurthie, 2014; Zayane, Jouini, & Mohamed, 2011). In recent research (Avşar & Arıca, 2018), Avşar et al proposed a three-stages based method for liver segmentation. Firstly, a bilateral filter was employed to smooth image, then edges were extracted using gradient operator. Authors introduced two different models to segment images into five parts (liver, vertebra, tumor, lining, and others). They are watershed and thresholding. Texture features, such as pixel value, directional derivative, LBP, difference of pixel with its neighbors were utilized to classify liver and non-liver.

2. 3. 2 Region growing

Selection of the initial seed point and stop condition are the key factors of this approach. Beck et al (Beck & Aurich, 2007) used a graphic user interface tool (HepaTux) that enables user to click a seed point voxel on three-dimensions planer view. The growth of regions will be stop when the intensity in neighbors significantly differs from seed point, otherwise, a voxel will be included into the region. During this process, a “virtual knife” can be used to remove over-segmentation. A postprocessing step is used to extend the segmentation result by computing a “limited” convex hull. Seed points can be automatically specified based on analyzing histogram of intensities of CT image (S. S. Kumar, Moni, & Rajeesh, 2011; Ruskó, Bekes, Németh, & Fidrich, 2007). In (Ruskó et al., 2007), the upper and lower values of intensity were used to threshold in order to build a binary mask. Erosion operator was applied on this mask. Last, the largest isolate region at center of liver is considered as initial seed point. Heart was separated from liver by constructing curves connecting the bottom of both lung lobes

along large gradient values. Tumor and vessel were added to liver region by hole filling algorithm. Kumar (S. S. Kumar et al., 2011) estimated seed point based on the range of histogram. Lesion in liver was extracted using Fuzzy C Mean (FCM). It differs from previous approach, Chen et al (Y. Chen et al., 2009) employed mean and standard derivation of the intensity of previous slice as a condition for stop function, whereas seed point was calculated from centroid of liver region of this slice. However, the initial seed point was manually selected by user. Basic image processing, such as anisotropic diffusion, morphology, hole filling was also used in denoising image and refining result. In (Maklad et al., 2013), a seed point was manually placed on IVC for extracting abdominal blood-vessels (ABV), which was classified into hepatic (HPV) and non-hepatic (non-HPV) blood-vessels. These vessels were then exploited for liver segmentation. This method achieved the highest score in its class. However, should any errors arise, interventions were required from the user. These included re-selecting the seed point, separating kidneys from a liver, untangling HBV from non-HBV, or removing IVC at the entry and exit points. While Lu (X. Q. Lu, Wu, Ren, Zhang, & Li, 2014) used Quasi-Monte Carlo method for selecting seed and growth of region. The stop function was given by average gradient using Robert operator.

2. 3. 3 Contour delineation

Contour -based segmentation, including active contour and level set method, have been increasingly used in liver segmentation. Additionally, initialization of contour is the first and significant step of this technique. Lim et al (S. J. Lim et al., 2005) explored the prior knowledge of liver, such as position, shape and intensity, followed by multiscale morphology operator to search initial boundary. Liver contours were classified into three groups based on gradient-label map. The intensity and

gradient-map value were utilized to optimize liver contour. Chi et al (Chi, Cashman, Bello, & Kitney, 2007) proposed a combinational strategy of rotational template matching, k-mean clustering and gradient vector flow geodesic snake. First, template matching method learned from a training set was integrated with thresholding to automatically find initial contour, followed by edge enhancement process. K-mean clustering was then applied to reduce the confusion of the boundary between liver and heart, vessel, kidney. Last, the evolution of contour was constrained by Laplacian diffusion of gradient of intensity and curvature, that are referred as external and interforce of contour. Method introduced by Dawant (M Dawant, Li, Lennon, & Li, 2007) required initial contour must be specified by user on one slice at middle slice of CT image. However, speed function of level set was defined as function of the path of the contour. A group of operators, such as thresholding, morphology, region labeling, were employed to prevent the growth of the front to skin and the ribs. Initial contour is also determined by integrating of thresholding method on the image of gradient, called by gradient level set image and seed point (J. Lee et al., 2007). The ROI of liver was manually selected to decrease the computation time. The stop function of level set was derived from the curvature diffusion filter. Instead, Wimmer defined a 3-D rough surface that pass through some given contours (from 6 to 8 contours, which drawn by user in image-planes). Both image and shape information, which were used to determine the distance between input contour to a current point, were included to the energy function of level set. Chartrand' rough mesh was generated in the same way (Chartrand et al., 2017; Chartrand et al., 2014). Template matching was implemented to initialize, whereas Laplacian was applied for segmentation phase. On the contrary, Garamendi (Garamendi, Malpica, Martel, & Schiavi, 2007) defined the energy function based on the mean of

region of interest (ROI) inside liver, which specified by expert. Then, Chan-Vese's Algorithm, another version of level set, was employed for segmentation. Li (D. Li, Liu, Chen, Li, & Yin, 2014) introduced a method for initializing level set using L1 norm, whereas GLCM was employed in refinement step. Yang et al (X. Yang et al., 2014) manually initialized a few seed points from specified slices, then fast marching threshold-based level set was applied in these seed points. However, the low contrast between foreground and background made it difficult to stop the level set evolution. Additionally, the number of seed point could be normally up to 10–15 points, specified on 4–5 slices, to sufficiently capture their variations. Another level set -based method by (Nuseiba M. Altarawneh, S. Luo, Brian Regan, & Guijin Tang, 2015), built initial contour at the middle slice using a distribution model, which learned from training set, and level set method. For other slices, the similarity between distribution of region inside contour and prior distribution model, the prior shape information, and previous contour, were employed to define energy function for level set. A recent study (Le & Tran, 2018) built 3-D surface using some segmented contours by user. This surface is then used as the initial condition for segmenting adjacent slices. Edge information combined with region information obtained from 3-D voxel on surface, were used to generated energy function for level set in 3-D space. In Hu 'study (Hu, Wu, Peng, Liang, & Kong, 2016), initial contour of liver was estimated by the convolutional neural network (CNN) and thresholding. Then anatomy of liver and probability map were used to drive initial surface to optimal position. Marcin (Ciecholewski, 2014) constructed 2D liver contour by combining both left and right-hand side ones, defined by 5 and 3 polylines, respectively. Provided a centroid of an image, a starting point of a contour was first located by comparing its intensity with that of lumbar spine section. Subsequent points were iteratively

traced on respective polyline, based on their geometric distance to a current point and its intensity within discretized ranges. A shortcoming of this method was being dependent on the location of lumbar spine and symmetry of an input image. Additionally, directly comparing intensities between points on a polyline was sensitive to imaging noise.

2.3.4 Graph based segmentation

The main idea of graph - based approach is to define region term and boundary term of graph cut (GC). To this end, Beichel (Reinhard Beichel, Bauer, Bornik, Sorantin, & Bischof, 2007) defined region term based on the difference between current voxel and distribution of given see point, whereas boundary term was calculated from image gradient, also referred as “surfaceness” measurement. Two refinement models include chunk -based refinement and mesh-base refinement were employed to optimize the segmentation results Another study with same technique also can be found in (R. Beichel, Bornik, Bauer, & Sorantin, 2012). Energy function can be obtained from the binary image of input image (Yusof & Burkhardt, 2011). First, input image was converted to binary mask, after anisotropic diffusion applied. A sequence operator of morphology, 3-D and 2-D largest connected component were used to refine binary image before GC was performed in it. Peng (Peng et al., 2015) extracted three texture features(intensity, LBP, VAR) for building GC energy function. Boundary term was calculated from intensity of image, whereas second term was measured by Wasserstein distance from current pixel to seed point of liver region and seed point of non-liver region. additionally, balance parameter for energy function was learned from a training set. To obtain better appearance of liver, using a seed point selected by user Liao (Liao et al., 2016) built both intensity and PCA model that were integrated into boundary function of GC. Location of pixel in liver region of previous slice supported

for reducing searching space of GC. Bottleneck detection removed segmentation before hole filling algorithm was performed. To make automation of proposed technique, (Liao et al., 2017) used density peak clustering algorithm to specify seed point. Graph cut applied on super-voxel, instead pixel was an approach proposed in (W. Wu, Zhou, Wu, & Zhang, 2016). Several image processing methods, such as maximum intensity projection (MIP), adaptive thresholding, morphological operator, were used to extract liver region in abdominal CT image. Then super voxels of input image were generated by simple linear iterative clustering (SLIC). Lastly, Gaussian mixture model (GMM) mapped voxels into probabilistic values, which were later integrated into energy function. Unlike previous model, Lu et al (F. Lu, Wu, Hu, Peng, & Kong, 2017) built probability map using CNN, which trained from some training set. Initial liver was first located by CNN model after filtered input image by anisotropic diffusion filter. The combination of initial liver and probability map were employed in GC function. Huang et al. (Q. Huang, Ding, Wang, & Wang, 2018) divided a CT image into subregions by using K-Mean, computed on an initial slice. A contour was then roughly estimated as that enclosing one with the highest number of pixels. Graph-cut with Gaussian parameters and inter-slice gradient being incorporated into region and boundary terms, respectively, were applied to assemble small regions. Vena cava was detached by a rectangular template. Other over-segments were removed, if they were less overlapped with a specified template and their average intensities fell out of a specified range. Interior void due to tumor was discarded by concave filling, except, however, those on boundary.

2. 3. 5 Statistical shape model

This approach requires a prior model learned from a training set of landmarks extracted from shape samples. Principal analysis components were generally used to build statistical shape mode (SSM). To do so, Heimann (Tobias Heimann, Meinzer, & Wolf, 2007) employed 20 training volumes of liver to build 3-D model. Each model characterized 2500 landmarks was used as SSM for liver segmentation. Local search was utilized to find initial parameters for SSM before coming local search which deforms mesh to input image. At each interaction, external force which controls the moving of a vertex to boundary and internal force which ensures the fitting between deformable mesh and SSM, were used to updated vertices based on Lagrangian equation of motion. Similarly, Kainmuller (Kainmüller, Lange, & Lamecker, 2007) built SSM with 7000 landmarks from 102 samples. The initial parameter of SSM was estimated using histogram of region inside liver and the liver after growing 5 voxels, whereas the location of liver was given by anatomy of liver. The initial mesh then used to input for freeform deformable segmentation procedure. Seghers' model (Seghers et al., 2007) consists 20 samples with 2004 landmarks and 6000 edges that connect two landmarks. The initial model was generated based on the affine registration of input image to reference image. For each landmark, 100 candidate points that are best matched were selected before an optimal strategy was employed to keep only one candidate. Alternatively, Saddi (Kinda, Saddi, Rousson, & Cheriet, 2007) generated SSM from 50 samples, using sign distance function to present for shape information instead of landmark. Pose and shape of liver was estimated by prior shape information based on intensity distribution inside or outside of liver before segmentation results were refined by template matching algorithm. Erdt (Erdt, Steger, Kirschner, & Wesarg, 2010)

constrained the initial model, which was built from 220 sample with 3612 landmarks, using prior shape information and curvature of model. A four-steps iteration was employed to deform image to model. The first step was to find a boundary points that best matched to current model points. These points were then used to reconstruct new model. Third and fourth steps aimed to constrains the free-form deformation and reconstruct model. The SSM, included 35 samples (from IR-CAB and MICCAI(T. Heimann et al., 2009)), was built using Multimodal Prior Appearance Model (MPAM) (Chung & Delingette, 2013) instead of PCA. Firstly, intensity profiled extracted from image used to build similarity graph, followed by build of Laplacian matrix. Expectation maximization (EM) was employed on Spectral which given by eigenvector of Laplacian matrix. This study used MPAM to model liver. Cheng et al. (X. Chen, Udupa, Bagci, Zhuge, & Yao, 2012), proposed a combination of active appearance model (AAM), live wire (LW), and graph-cut for learning textual model, recognizing object of interest, and obtaining its final clustering, respectively. Similarly, Li et al. (G. Li et al., 2015), imposed morphological constraint on an initial boundary for anatomically plausible liver, by means of principal component analysis (PCA). Any excessive variations left in unseen instances was regulated by deformable GC. Considering pathological cases, Li et al. (X. Li et al., 2018) adopted hybrid (2D and 3D) densely connected UNet (referred to as H-DenseUNet) for segmenting both liver and liver tumor. The 2D DenseUNet was used to extract their features within a slice, while 3D DenseUNet allowed learning of spatial information between consecutive ones. These DenseUNet models were fused and optimized to obtain final liver and tumor segmentation. Despite relatively high scores in its class, these models took 9 hours to converge and 30 hours in total for training. Once completed, a new instance could be segmented within 30 to 200 seconds per image.

Conclusion

Unlike MRI, imaging tissue with CT often exhibits ambiguous boundaries between adjacent organs, due to similar X-ray absorption. Priors on liver shape and size could very well offer spatial cue in segmentation. Therefore, several studies exploited gradual variation across consecutive slices, covering the anatomical structure (Chartrand et al., 2017; Y. Chen et al., 2009; Liao et al., 2017; Liao et al., 2016; W. Wu et al., 2016), to improve segmenting accuracy. For instances (Liao et al., 2017; Liao et al., 2016) localization from the previous slice was incorporated into the GC energy function to limit the search space, during optimization. Meanwhile, spatial information gathered from neighboring slices were found exploited to seek suitable seed points (Y. Chen et al., 2009), to determine VOI via MIP (W. Wu et al., 2016), or to build a 3D model from a user defined contour stack (Chartrand et al., 2017). Depending on the amount of user interaction, it is possible to classify mentioned approaches into two class: *fully automatic* and *semiautomatic* method. It has long been debated whether a fully or semi-automatic method is suitable for a given CAD problem.

Despite several attempts to accelerate the process by automatic seed point selection (S. S. Kumar et al., 2011),(W. Wu et al., 2016),(Liao et al., 2017), if an underlying CT image includes multiple regions, its localization may be less accurate or even lie completely in non-liver areas (e.g., tumor, or dark object). It was, therefore, pointed out in [13] that interactive methods and those based on statistical deformable model outperform their automatic counterparts, especially those without prior model. Thus far, due to particularly diverse morphology of a liver, universal model would require prohibitively large sample collection for training. On the other hand, with limited known liver samples, higher interaction would be required from user's part. Depending on

specific purpose and expected degree of confidence, care must be observed when balancing these requirements and devising a liver segmentation scheme. Previous studies have attempted liver segmenting methods, implemented on various medical systems. It was generally perceived that those with higher degree of user interaction involved outperforms their counterparts, inevitably at a cost of greater time consuming and endeavor required. Beichel's study, for example, reach to score of 82/100 with time consumption of 36 minute and high degree of user interaction (T. Heimann et al., 2009). Maklab's work (Maklad et al., 2013) obtained high score in the leaderboard, but user may be asked to fix some errors during process. It has been mentioned in (T. Heimann et al., 2009) that, the higher of user interaction, the better of segmentation result. On the other hand, improving segmenting accuracy of fully automatic liver extraction often relied on supervised machine learning (ML) strategies and expert systems that required model training, and thus large amount of data, which is not always available. As can be seen in Kainmuller's method, **112** samples with **7000** landmarks were required for building SSM model. Li's research (X. Li et al., 2018) reached to highest score in comparing to others. However, this system required 131 samples for training the model, and took 30 hours for training and 30-200 second for evaluating an image. Inspired by the dilemma, this study considered the balance between segmenting accuracy and user interaction, suitable for typical clinical setting with limited domain of experts. It proposes a semi-automatic liver segmentation from 3D CT images.

2.4 3-D representation and pre-processing

2.4.1 Volumetric data

Image data acquired from CT or MRI scan are usually stacked as a set of 2-D images, also called as volume grid. A volume grid is a regular grid with a number of volume pixels (called by voxel) ordered in a regular pattern. In contrast to a vertex on polygon, voxels themselves are not associated with information regarding their positions (coordinate), instead, they are often 3-D scalar values which correspond to pixel values in 2-D image (e.g., the intensity). The location of a voxel can be designated from positions relative of surrounding voxels. Volume data contains either surface or internal structure that overlaid by voxels at surface. An example of 3-D volume data is illustrated in **Figure 2.17**.

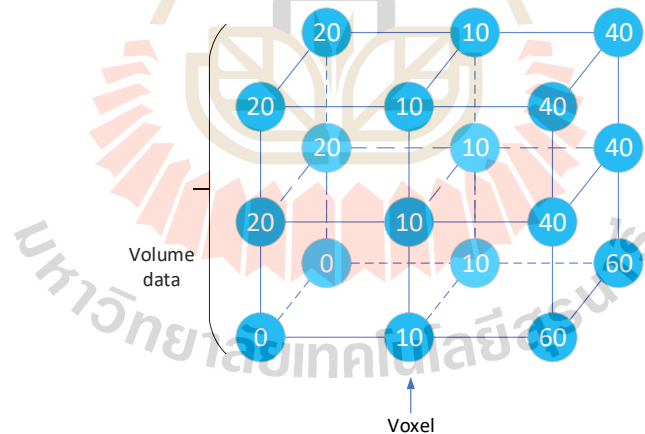


Figure 2.17 The 18 voxels of scalar values composed from 3 slices.

2.4.2 Volumetric visualization

Volumetric visualization is a process for generating a 2-D graphical presentation of a 3-D volume data. It is useful in many applications, particularly in

medical field. Volume described by voxels can be visualized by various techniques, such as multiplanar rendering, surface rendering (contour-based surface reconstruction, isosurface extraction based on marching cube), volume rendering (ray casting, shear warp factorization and splatting) (Kaufman, 2003; T. S. Kumar & Vijai, 2012). Both benefits and drawbacks of each technique will be discussed in next item.

2.4.2.1 *Multi planar visualization*

This is a simple method used to visualize structure of an object by a combination of planes across volume data at a specified intersection line. There is no constrain on the number of planes required in this method. The output of this method is a 2-D presentation and the amount of information depend on the number of planes. Usually, there are three planes, include axial, coronal and sagittal which provide information of width, height, depth of an object in 3-D space (as seen in **Figure 2.18**). It enables surgeons to locate tumor inside liver as well as relationship of tumor with surrounding tissues. The most important advantage of multi planar visualization is the simplicity and efficient execution time. However, the fully 3-D structure of object cannot be presented by using a few planes.

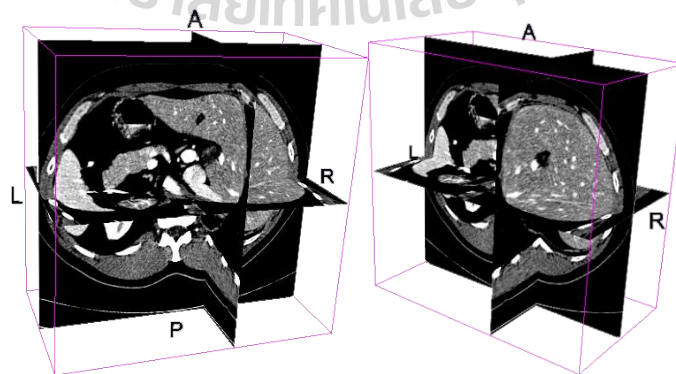


Figure 2.18 Multiplanar visualization of liver

2.4.2.2 *Surface rendering*

Surface rendering is invoked to techniques used to generate a 3-D presentation of an object, based on associated geometric information, such as vertex, edge, triangle, polygonal mesh. Its objective is to define an approximated surface contains within volumetric data based on interpolation. There are two most popular techniques for building surface of volumetric image from medical image, i.e., contours based – surface reconstruction and iso-surface reconstruction (T. S. Kumar & Vijai, 2012).

Contour-based reconstruction is a technique based connecting of 2-D parallel contour extracted from each slice in a volume to generate a 3-D surface of volumetric data. The reconstruction of 3-D surface using a set of iso-contour has to address three main issues, including the valid connection between a contour with its neighbors (how to connect vertices between contours), creating a set of triangles from edges, and the branching problem calls for a serious attempt when the numbers of contours in each plane are different (D. S. Wang, Hassan, Morgan, & Weatherill, 2006). This technique is divided into sub-categories, including contour stitching method and field-based method (Nilsson, Breen, & Museth, 2005).

The second technique generates 3-D surface based on the construction of polygon mesh of an iso-surface with predefined threshold. To this end, each voxel on rectangle grid, usually presented by a scalar value, will match to fixed threshold (T). Assume v is value of a voxel on grid, $P(v, T)$ is a binary function, where $v, T \in R^2$. Voxel i^{th} is inside surface if $P(v_i, T)=1$, otherwise, this voxel is outside surface. A surface can be implicit defined as a set of faces formed intersection points between internal and external voxels. A surface is considered as an *iso-surface* if T is

applied for entire volume data, T is called by *iso-value*. Among methods for extracting of iso-surface from volumetric data, Marching Cubes, introduced in (Lorensen & Cline, 1987), have been widely used in medical applications. A detail description of the technique will be given in section 2. 4. 4.

2.4.2.3 Volumetric rendering

Volumetric rendering is a set of methods for visualizing volume data without imposing any geometric structure of data. It differs from iso-surface rendering technique, which generates a hard surface based on iso-value. This technique allows one to observe internal structure by a combination of setting up a camera and the opacity and color of each voxel. Volume rendering technique can be categorized into four sub-methods: ray-casting, resampling or shear-warp factorization, texture slicing, and splatting (McReynolds & Blythe, 2005). However, the most disadvantage of volumetric rendering-based visualization is complexity. Regarding liver segmentation task, to have a better of visualization of 3-D anatomy of liver, vascular systems and tumor should be independently segmented by another process. By using segmentation result, liver and its components are clearly visualized and processed.

2. 4. 3 Three-dimensional file format

Three-dimensional model can be used for visualization, printed out and store in computer under a document. In order ensure the consistency between systems used to create or present 3-D models, there exist many file formats designed for generating and storing them. They are different in the way of structure elements of a 3-D object, such as datatype, list of vertices, edges, faces, color normal, topology and others. Most 3-D visualization tools support a conversion between file formats. Some of them

are Stereo Lithography (STL), Polygon File Format or the Stanford Triangle Format (PLY) and Visualization Toolkit (VTK) file format.

Stereo lithography

Created by 3D systems (<https://www.3dsystems.com/>) in 1988. This file format is useful for rapid prototyping, 3D printing and computer-aided manufacturing. It allows one to present the surface geometric of 3-D object by vertices, normal and face. The color presentation of object is not included in this type of file format. Content of file can be given either in ASCII or binary format.

Polygon File Format

Polygon File Format is designed by Stanford graphics lab in the mid-90s. It is used to described 3-D data obtained from a scanner. This file format can either present topology of 3-D object, such as datatype, list or vertices, edges, faces, normal, texture coordinate or color of vertices, color of face in ASCII or binary format.

Visualization Toolkit file format

This file format is introduced by Visualization Toolkit (<https://vtk.org/>). It is divided into two sub-formats, include *serial format* that easy for reading/writing data in file by hand and programmatically, XML format that optimize for random accessing and compressing. VTK file format supports both ASCII and binary type.

The ASCII format presents data by ASCII characters which is convenient to read or write by human. However, to reduce file size and increase reading/writing speed, it is recommended to use binary format. There are many 3-D visualization tools available that support most file formats under ASCII or binary format, such as Meshlab (<http://www.meshlab.net/>), Paraview (<https://www.paraview.org/>),

PointCloud (<http://pointclouds.org/>), .etc. They are open source and cross-platform tools that can be used for research purpose and application.

2. 4. 4 Marching cubes

Marching Cube has been widely used in medical applications for volume rendering from CT or MRI images. It allows one to create a 3-D surface of the high resolution by triangular mesh. The process of marching cube begins from dividing volume data into discrete cubes. Each cube in the grid is presented by 8-vertices which correspond to voxels. By using a binary function, a vertex of cube can either inside or outside a surface. Thus, there are 2^8 of cases that a surface pass through a cube. Due to the symmetric property of cube, the number of cases reduced to 15 unique configurations, as showed in **Figure 2.19**.

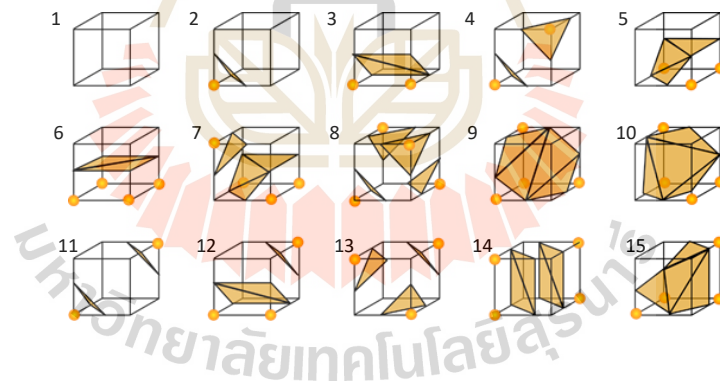


Figure 2.19 Fifteen unique configurations of marching cube

(The orange circles on cubes present for voxels inside surface. (Image downloaded from source and edited by adding numbers: https://en.wikipedia.org/wiki/Marching_cubes, accessed on 20/5/2021)).

In order to manage the above cases, an 8-bits number (also considered as cube-index) is used as a lookup value, where each bit in sequence number will

correspond to a state (inside or outside) of a vertex. Additionally, each configuration will form a set of different edges and triangles. By using cube-index, one can determine list of edges as well as triangles based on lookup edge-by-cube-index table and triangle-by-cube-index table. **Figure 2.20** illustrate building cube-index, edge, and triangle lookup table for one configuration of marching cube.

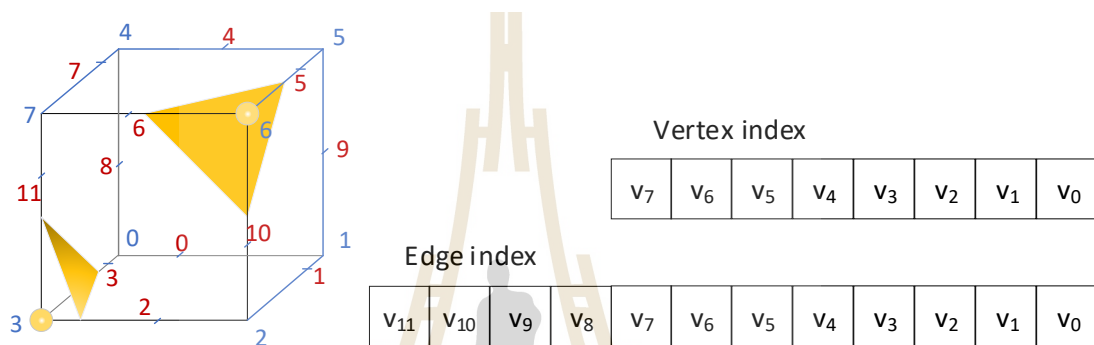


Figure 2.20 An example of build marching cube for configuration 4

Assume that the index of vertices on a cube are given by **Figure 2.20**, the cube-index for this configuration can be written as a sequence of follow binary number 00010010. Two-bit value of one mean 3th and 6th vertices inside surface, others outside vertices are set to zero. Edge indices fixed to each vertex can be numbered as a 12-bits number, each bit indicates whether an edge to be processed or ignored. Similarly, a triangle is generated from vertices by cube-index. For example, edge index and table index of two vertices in **Figure 2.20** are given by:

$$edgeTable[00010010] = 110001101100$$

$$triangletable[00010010] = \{2,3,11,10,6,5, -1, -1, -1, -1, -1, -1, -1, -1, -1\}$$

Let T be iso-value to be used to build 3-D isosurface, the intersection point P between P_1 and P_2 are computed through linear interpolation as follow

$$P_x = P_{1x} \frac{|T - v_2|}{|v_2 - v_1|} + P_{2x} \frac{|T - v_1|}{|v_2 - v_1|}$$

$$P_y = P_{1y} \frac{|T - v_2|}{|v_2 - v_1|} + P_{2y} \frac{|T - v_1|}{|v_2 - v_1|}$$

$$P_z = P_{1z} \frac{|T - v_2|}{|v_2 - v_1|} + P_{2z} \frac{|T - v_1|}{|v_2 - v_1|}$$
(2.26)

where v_i is the scalar value associated vertex i on volumetric data; $|\cdot|$ is absolute value.

To maintain realistic visualization of 3-D object, the normal vector of each triangle face can be calculated from its three vertices (P_1, P_2, P_3) as the equation:

$$\vec{N} = \vec{U} \times \vec{V}$$
(2.27)

where “ \times ” is cross product operator, $U = P_2 - P_1$ and $V = P_3 - P_1$. **Figure 2.21** illustrates for calculation of intersection point and normal vector.

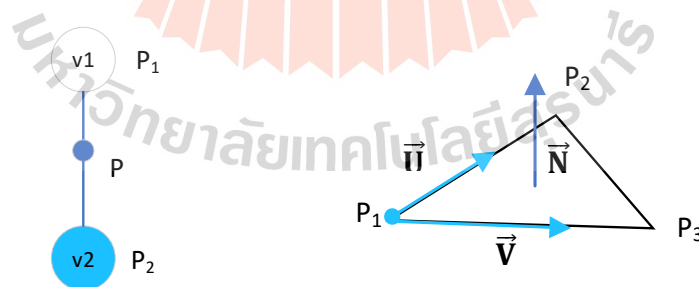


Figure 2.21 The intersection point and normal vector

The segmentation results from previous step are store as a binary volume, each slice in volume is presented a binary image ordered as in original, the object

regions are set the value of 1, whereas the background is set to 0. The size of pixel in each image and slice thickness are well-known. The 3-D surface of liver is reconstructed by Marching cube method with iso-value of 0.5.

2. 4. 5 Mesh smoothing

Due the large thickness between slices in CT or MRI images, to produce a faithful 3-D model of liver, reconstructed surface should be smoothed. The problem of mesh smoothing invokes to address two properties, denoising and anti-shrinking. This section introduces some techniques used for smoothing surface.

Let S be a mesh surface and v_i be a vertex on S ; N_i be a neighbour of v_i , such that for each v_j in N_i , there exist an edge directly connect between v_i and v_j . It is pointed out that, the smoothing of a surface can be controlled by the diffusion equation as follow

$$\frac{\partial X}{\partial t} = \alpha \Delta^2 X \quad (2.28)$$

where Δ^2 is the Laplacian operator on X ; α , a small positive number, is used to control speed of smoothing. The linear approximation of Laplacian on a vertex v_i of a mesh, also called by umbrella operator, is given by the following equation:

$$U(v_i) = \frac{1}{\sum_j \omega_j} \sum_{j \in N_i} \omega_j (v_j - v_i) \quad (2.29)$$

where ω_j is the positive weight; v_j is the neighbor of v_i . If $\omega_j = \|v_j - v_i\|^{-1}$, then (2.30) is referred as scale-dependent smoothing or Fujiwara smoothing.

The updating process applied for X is computed by:

$$X^{t+1} = X^t + \alpha U(X^t) \quad (2.30)$$

However, the applying of (2.30) for smoothing leads to shrinkage on surface. It is because the same weight is applied for all neighbours of v_i . To solve this problem, Taubin (Taubin, 1999) has proposed a new method that uses two coefficients. One is to control the shrinkage, and the other is used to inflate the mesh (Zhao & Xu, 2006). This technique was based upon explicit Laplacian. The advantages of this model are the eliminating shrinkage effects. It performs in linear time and consumes linear memory. However, the reducing of time step leads to the increasing of the number of computations.

Instead of using Laplacian from diffusion equation, Desbrun (Desbrun, Meyer, Schröder, & Barr, 1999) et al used the mean curvature flow for updating mesh in smoothing procedure. It used implicit Laplacian technique. The calculating of mean curvature was given in (Meyer, Desbrun, Schröder, & Barr, 2003).

Each vertex $v(x, y, z)$ on 3-D surface S can locally be approximated by a tangent plane. Planes contain normal vector are call by planes of principal curvatures/ normal planes. The intersection between normal plane corresponding to direction θ and surface forms a curve. Then the curvature of this curve is referred as the normal curvature $k^N(\theta)$. Let \vec{n} be the normal vector at that point; k_1, k_2 be the maximum and minimum curvature once normal plane rotates around normal vector (see in **Figure 2.22**).

The mean curvature is defined by

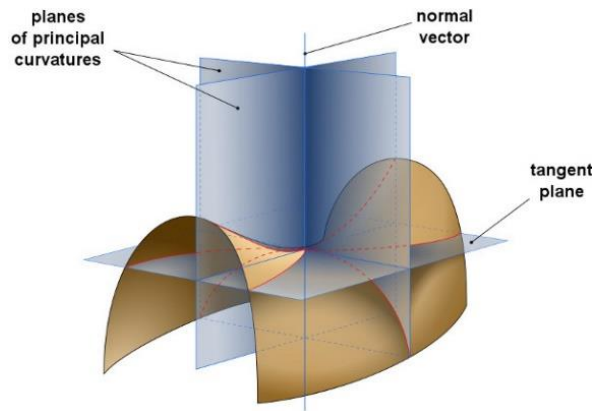


Figure 2.22 Tangent planes, and directions of principal curvatures

(Image source: <https://en.wikipedia.org/wiki/Curvature>, accessed on 20/5/2021)).

$$k_H = \frac{1}{2\pi} \int_0^{2\pi} k^N(\theta) d\theta = \frac{1}{2\pi} \int_0^{2\pi} (k_1 \cos^2(\theta) + k_2 \sin^2(\theta)) d\theta \quad (2.31)$$

Euler's theorem stated that the mean curvature can also be computed an average of principal curvatures, i.e.,

$$k_H = \frac{k_1 + k_2}{2} \quad (2.32)$$

Let A be the area of small region around; $diam(A)$ be its diameter; ∇A be the gradient operator of A respect to (x, y, z) , then mean curvature is calculated by

$$2k_H \vec{n} = \lim_{diam(A)} \frac{\nabla A}{A} \quad (2.33)$$

Meyer has proposed the equation for computing mean curvature at point v_i on surface S as following equation:

$$2k_H \vec{n} = \frac{1}{2A} \sum_{j \in N_i} (\cot \alpha_{ij} + \cot \beta_{ij})(v_i - v_j) \quad (2.34)$$

where α_{ij} and β_{ij} are determined as **Figure 2.23**.

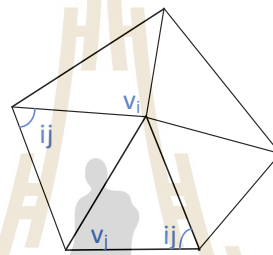


Figure 2.23 The neighbour of a vertex and inter-angles

Let $K = k_H \vec{n}$, the updating for mesh is based on solving the following linear system (Desbrun et al., 1999)

$$(I - \alpha dt K) X^{n+1} = X^n \quad (2.35)$$

2.5 Functional segmentation for preoperative liver

Liver resection has shown great outcomes in therapeutic intervention of various hepatic diseases. For example, patients suffered from hepatocellular carcinoma, mass-forming cholangiocarcinoma, and hepatic metastasis, have significantly improved prognosis, after underwent the procedure. Nonetheless, its success particularly depends on preoperative assessment of liver volume. When making surgical decision, care must

be taken to ensure that remaining liver is adequate to maintain its normal function, otherwise the patient would be put at great risks of liver failure. A number of techniques have been proposed to determine postoperative liver sufficiency. In particular, future liver remnant volume (FLRV) can be estimated and employed as standardized determinant of postoperative outcome. Research by Kishi (Kishi et al., 2009) and Abdalla (Eddie K. Abdalla, Barnett, Doherty, Curley, & Vauthey, 2002) et al., reported that this ratio correlates well with risks of liver failure, morbidity, and death. Resection has also been found operated on both donors and recipients in liver transplantation, for treating a patient with chronic liver diseases. In this surgical procedure, the size of a transplanted liver must fit to that of the recipient body. As general criterion, the graft weight (GW) threshold must be 0.8-1.0% (Ben-Haim et al., 2001) (or 0.6-1.2 (S. Breitenstein et al., 2009; Clavien et al., 2010; Clavien et al., 2007; Gotra et al., 2017; Ribero et al., 2007)) of recipient's weight. On the other hand, postoperative complications are likely when the ratio exceeds 4.0% (Akdur et al., 2015; Allard et al., 2017), or falls below 0.8%. GF percentage is also applied in other contexts, e.g., preoperative portal vein embolization and post-transplantation assessment of graft regeneration, etc.

Traditionally, estimation of liver volume and functional segmentation were done manually on preoperative imaging, such as computed tomography (CT) (M. C. Lim, Tan, Cai, Zheng, & Kow, 2014). Hand delineation of anatomical structure on medical images is tedious, time consuming, and prone to inter- and intra-observer variability (Keegan et al., 2004). Therefore, developing automated computer software to assist the maneuver could be beneficial in clinical usages.

Liver functions as an active filter by excreting wastes and toxin from oxygen and nutrition from the gastrointestinal circulatory system to the kidneys (Vekemans &

Braet, 2005). Contacting with excessive toxin carried via portal vein (PV) usually causes liver diseases, such as cirrhosis, fibrosis, and cancer. Unlike some other abdominal organs, a deteriorated liver cannot be substituted by any artificial prosthesis, but graft and regeneration of liver remnant. It is well received that a crucial part in successful clinical diagnosis, surgical planning, preoperative resection, and postoperative monitoring is played by understanding of subject specific functional structure of the liver and major hepatic vasculature.

As the standardized language among radiologists and surgeons, external shape of a liver is divided into two hemi-livers, i.e., left, and right lobes, by hepatic vein (HV). Anatomically, Couinaud's work indicated that a liver comprises of eight functionally independent segments, each of which has its own vascular in- and out-flow, biliary drainage, and lymphatic drainage (Couinaud, 1999; Jones, 2018). With Couinaud's scheme, the subdivisions are based on the distribution of the two internal venous systems, i.e., three HVs and two PVs. Particularly, the right (RHV), middle (MHV) and left (LHV) hepatic veins divided a liver into the right posterior, right anterior, left medial and left lateral sections, respectively. These segments are further separated into interior and superior parts, by the left (LPV) and right (RPV) portal veins. Eight functional segments of a liver are labelled accordingly as follow: The anterosuperior and posteroinferior sectors of the right lobes which contain the segments V, VI, VII, and VIII are demarcated by RHV. This plane runs from inferior vena cava (IVC) to the gallbladder fossa, also called Cantlie's line. The falciform ligament separates the left lobe into media (the segment IV) and lateral parts (the segments II and III). Finally, the segment I, also referred to as caudate, is bounded posterior laterally by the fossa for the inferior vena cava, anteriorly by the ligamentum venosum, and inferiorly by porta hepatis.

Generally, functional comprehension and corresponding classification enable successful surgical procedures, such as accurate removal of only damaged section without causing risks to healthy ones. As such, with self-recovery, an operated liver may be able to regenerate within 3-12 months after a major resection surgery (M. F. Chen et al., 1991).

With the recent advances in computerized translational medicine, especially computer assisted diagnosis (CAD) and intervention (CAI), a number of methods were proposed to reduce time consuming and tedious traditional preoperative planning by means of anatomical models and virtual reality (Lamade et al., 2000; Oshiro & Ohkohchi, 2017; Reitingner et al., 2006; Yeo et al., 2018). Thus far, existing techniques remained yet to be enhanced. Therefore, this work proposes a novel method that is able to localize the hepatic vascular networks more accurately and efficiently, and to effectively delineate all functional segments (I-VIII) of a liver on its reconstructed 3D surface, prior to resection surgery. These are in order to better reduce adverse effects on patients and complications, thus extending their life expectancy.

A liver, extracted from 3D tomography, may be described by either a set of binary interior voxels (\mathbb{R}^3) or a 2-manifold (\mathbb{R}^2) of enclosing ones. Accordingly, classifying its element into one of Couinaud's segments can be categorized, by these 3D descriptors, into those based on geometric functions on the respective domains, i.e., voxel and surface-based approaches. Reviews on the state-of-the-art liver functional segmentation are made in the next subsections.

2. 5. 1 Voxel-based approach

With this approach, liver voxels are assigned to these segments based on the distances between their locations to a specific branch in the venous network. For

example, Selle et al. (Selle, Preim, Schenk, & Peitgen, 2002), determined memberships of a segment, in reference to LPV and RPV. Therein, region growing was first applied to find a suitable threshold to extract the hepatic vascular network from the images. Thinning algorithm was then applied to skeletonize the extracted vessels, to define the network geometry, from which a vascular tree was created. After having HV removed from this tree using directed graph, a voxel was labelled by Laplacian (LSA) or nearest neighbor (NNSA) segment approximation. Nevertheless, computing the Laplacian on a voxel domain was intensive. A simpler and more straightforward method was proposed by Huang et al. (S.-h. Huang et al., 2008), where both vessels and liver itself were projected onto planes. Firstly, three principal vectors were each defined by the intersection of the three major HV branches and the nearest point along the respective one. On labeling segments on both hemi-livers, two additional planes were each defined by separate normal vector. The one on the left plane was the average of the three principal vectors, while the right one was that of MHV and RHV. Evidently, vessel extraction was the key element in both methods. Yang, et al. (X. Yang, Yang, Hwang, et al., 2018) improved over Selle's one. In Yang's work, region growing was similarly applied to intensity images, but up to six Gaussian mixture models (GMM) were estimated. Among these GMM, the most suitable threshold interval was chosen to extract venous tree, whose major branches were then identified by using local searching. Couinaud segments of the liver were finally labelled following (Selle et al., 2002). In addition to categorical search, Voronoi algorithm was adopted by Debarba (Debarba, Zanchet, Fracaro, Maciel, & Kalil, 2010) and Chen (Y. Chen, Yue, Zhong, & Wang, 2016), et al., to classify voxels with their segments. Their difference was in calculating a Voronoi diagram. The first method used the distance from a voxel to seed points, handpicked on

HV and PV, whereas the other considered only PV, when building eight vascular trees, from which distances to each voxel were measured. Zhang et al. (Zhang, Fan, Wan, & Liu, 2017), adopted similar strategy, but focused on enhancing vessel segmentations.

2.5.2 Surface-based approach

Unlike voxel-based ones, methods in this group classify hepatic segments directly on a reconstructed 3D liver surface, by various geometric elements, mostly ordinary planes. Similar to the previous approach, however, these elements were typically derived from main vascular branches. As one of a few exceptions, Boltcheva et al. (Boltcheva et al., 2006) defined Couinaud's regions based on six landmarks, automatically detected on a liver, instead of its vascular network. Differential geometry was employed to detect two points on vena cava, two others on gallbladder bed, and two more points on inferior liver border of the left lobe. Five planes were constructed from these points and finally used to separate the liver volume. In other similar works, a liver was separated by using four (Oliveira, Feitosa, & Correia, 2008) and three (Butdee, Pluempitiwiriyaewej, & Tanpowpong, 2017) planes. The former fitted the planes to three major HVs and PV, while the latter defined the planes from seven manually specified points on RHV, MHV, and LHV. In (Butdee et al., 2017), superior and inferior regions were divided by another plane on an imaging slice, where PV was most visible. On this plane, caudate lobe was also cut by a Bézier curve, whose four control points were manually defined by a user. Specifying these landmarks on a liver is, however, subjective, and dependent on user's experience. More consistent approach is to do so on salient features, e.g., those on main vascular networks. Provided skeletonized HVs and PV, but with their small branches removed, Lebre et al. (Lebre et al., 2019) computed four corresponding directional vectors. The first three vectors originated

from HV root and pointed along respective hepatic veins, within close proximity to their root. The last one was computed from the longest chain of vertical points along Z-axis. Liver subdividing planes were created from these vectors. Instead of cutting a liver by planes, some studies performed subdivision directly on an extracted liver surface into patches, corresponding to Couinaud's regions. For instance, Pamulapati et al. (Pamulapati, Venkatesan, Wood, & Linguraru, 2011) first segmented hepatic vessels, from which undirected graph was then built, by using GC and skeletonization, respectively. Vessel sections were labelled with either RHV, MHV, LHV, PV, or RPV, depending on their positions and orientations. Surface patches were traced from root to ends, via respective branching points in the sub-trees. Much straightforward interactive method was proposed by Rusko et al. (Rusko, Mateka, & Kriston, 2013), where B-spline surfaces were interpolated from user defined control points on 2D slices. These control points were placed on the venous traces, provided that: 1) Each surface must be interpolated by at least three traces, each of which contained at least three points. 2) There was no self-intersection in any trace. 3) The view on which a trace was drawn must be consistent, i.e., either axial, coronal, or sagittal. In 2020, the most recent study by Alirr and Rahni (Alirr & Abd Rahni, 2020), connected the vena cava with HV centerlines, defined on individual slices, to build three hepatic planes, while the portal plane was defined by a selected image slice. Therein, the veins bifurcations were located by deforming statistically trained atlas to match extracted vasculature on CT images.

2. 5. 3 Summary of latest algorithms

Some remarks may be drawn from the above surveys. The methods in the former group (Y. Chen et al., 2016; Debarba et al., 2010; S.-h. Huang et al., 2008;

Selle et al., 2002; X. Yang, Yang, Hwang, et al., 2018; Zhang et al., 2017) partitioned a liver based on membership values associated with interior voxels. Thus, their major hinderance was evaluation of membership function for each voxel with respect to relevant features, such as vascular structures, was computationally intensive. In addition, no topological violation of any resulted segment was asserted either on individual voxels or their aggregation. Nor did they consider exterior anatomical landmarks, such as falciform ligament and gallbladder fossa, or liver appearance in general (Selle et al., 2002). Although Zhang et al. (Zhang et al., 2017) specifically followed Couinaud's theory, but their empirical assumptions on vasculature were not adequate to completely avoid post-process correction by an expert. With much less data involved, when only extracted liver surface and vascular outlines were considered, even greater user interaction was inevitable for methods in the second group (Boltcheva et al., 2006; Butdee et al., 2017; Lebre et al., 2019; Oliveira et al., 2008; Pamulapati et al., 2011; Rusko et al., 2013). Take Butdee's and Rusko's method (Butdee et al., 2017) (Rusko et al., 2013) for examples. Segmenting required at least ten user defined points, and at least three traces, each with at least three points, for creating sectional planes and B-spline surfaces, respectively. These subjective processes caused not only fatigue during batch analyses, but also significant observer variability. A deformable statistical atlas [28] could help elevating manual intervention, provided that sufficiently large training set was available. Unlike other methods in its group, the one, suggested by Boltcheva et al. (Boltcheva et al., 2006), relied solely on the shape of liver, while neglecting its interior vasculature. Lastly, most of works in both groups, except (Boltcheva et al., 2006; Butdee et al., 2017; Y. Chen et al., 2016; Zhang et al., 2017), did not report any annotation of caudate lobe (segment I).

2.6 Mesh parameterization

The 3-D liver surface reconstructed by Marching Cube contains a large number of triangular meshes. It provides a detail of 3-D liver model that is useful for diagnostic and surgical operation. Generally, the resolution of 3-D liver model depends on the number of slices captured by the scanner, i.e., a volumetric data of 394 slices can approximately produce a mesh of 250k vertices and 500k triangles. Such a mesh is notoriously expensive to process, store, render and real-time simulation. Mesh parameterization offers a simple and efficient approach to dealing these drawbacks.

The parameterization of a mesh is considered as determining a bijective, uniform mapping to map a given mesh in a domain into suitable domain, i.e., unit sphere. The mapping must contain two characteristics, minimization of the distortions and preservation of area (Brechtbuehler, Gerig, & Kuebler, 1992). Mesh parametrization have been used in numerous applications of image processing, such as texture mapping, mesh completion, mesh compression, mesh editing, surface fitting, morphing (Rose, Praun, & Sheffer, 2006). In medical imaging, it is useful in analyzing and comparing biological materials, such as the brain, carotid artery and hippocampus (Pui Tung Choi, 2016), and the modeling of muscles, such as those of the levator ani (S.-L. Lee, Horkaew, Darzi, & Yang, 2004) and face (Qian, Su, Zhang, & Li, 2018; Yueh, Gu, Lin, Wu, & Yau, 2015). Base on the technique that is used to minimize distortion on parametric domain, the mapping can be classified four groups (Floater & Hormann, 2005), including *planar* mapping (ignore all distortion), *conformal mapping* (minimize angle distortion), *equiareal mapping* (minimize area distortion) and *isometric mapping* (minimize a combination of angle and area distortion). Among of these approaches, the *conformal spherical mapping* has been established as a convenient method to retain local

geometric information when mapping a *genus zero surface to spherical domain* (Gu, Wang, Chan, Thompson, & Yau, 2004; Y. Wang, Gu, Chan, Thompson, & Yau, 2004). It has been commonly accepted that conformal mapping minimizes the angular distortion of surface elements, and thus their geometrical formation (Gu et al., 2004; Y. Wang et al., 2004). It has been demonstrated elsewhere (Gu et al., 2004; Y. Wang et al., 2004) that, when provided with a mesh with specified topology, it can be mapped onto a structure with the same diffeomorphism, regardless of its geometry.

To obtain the SCM of a mesh (Gu et al., 2004; Y. Wang et al., 2004), the Gauss map is firstly calculated and used as the input for Tuette map. The conformal spherical map is built using the Tuette map. Given a genus zero mesh M , and a normal vector $\vec{n}(v)$ at each vertex v on M . A Gauss map $N: M \rightarrow S^2$ is defined as

$$N(v) = \vec{n}(v) \quad (2.36)$$

Let (K, f) be a mesh defined on a simplicial complex K , and f be a function which embed $|K|$ in R^3 , $f: |K| \rightarrow R^3$, \vec{f} denoted for the vector value function; u, v be vertices. All piecewise linear functions f defined on K form a linear space, denoted by C^Δ . The string energy for each edge $\{u, v\}$ is presented by

$$E(f) = \langle f, f \rangle = \sum_{\{u,v\} \in K} k_{u,v} (f(u) - f(v))^2 \quad (2.37)$$

where $k_{u,v}$ is the string constant. Suppose T_α, T_β are two faces shared the same edge, with $T_\alpha = \{v_1, v_2, v_3\}$, define the parameters,

$$\begin{aligned}
a_{v_1, v_2}^\alpha &= \frac{1}{2} \frac{(v_1 - v_3) \cdot (v_2 - v_3)}{|(v_1 - v_3) \times (v_2 - v_3)|} \\
a_{v_2, v_3}^\alpha &= \frac{1}{2} \frac{(v_2 - v_1) \cdot (v_3 - v_1)}{|(v_2 - v_1) \times (v_3 - v_1)|} \\
a_{v_3, v_1}^\alpha &= \frac{1}{2} \frac{(v_3 - v_2) \cdot (v_1 - v_2)}{|(v_3 - v_2) \times (v_1 - v_2)|}
\end{aligned} \tag{2.38}$$

T_β is defined similarly. If $k_{u,v} = a_{u,v}^\alpha + a_{u,v}^\beta$, the string energy is called by the harmony energy. In the trivial case, $k_{u,v} = 1$, the string energy is known as Tuette energy. These processes are described in (Gu et al., 2004; Y. Wang et al., 2004).

Parameterization has many applications in different fields, such as computer graphics, medical image analysis, and computational biology (Shen & Chung, 2006). In computing, it is useful for several applications, such as texture mapping, smoothing, morphing, compression, and so on (Ying Li, Yang, & Deng, 2006). Mesh parameterization associated with spherical harmonics is used in mesh resampling as well as comparing between models (Y. Wang et al., 2004). In this study, parametric mesh is performed to map 3-D liver surface to spherical domain, then spherical harmonics is applied to resample this model.

However, particularly for anatomical shapes, a conformal mapping between two genus-0 surfaces is not unique but forms a Möbius group. Moreover, the alignment of their salient features is not necessarily guaranteed. To resolve this uncertainty, optimized Möbius transformation by explicit landmark matching or by modified mesh energy function was proposed (Lui, Wang, Chan, & Thompson, 2007; Y. Wang, Lui, Chan, & Thompson, 2005). While they both created conformal mapping with correspondences,

the latter is superior in terms of alignment error, and was hence adopted in this study. To define an optimal mapping between two liver surfaces S_1 and S_2 , let K denote a triangular simplex of a liver surface and $[u, v]$ be an edge connecting two vertices, u and v . Then, let $f_s: S_s \rightarrow \mathbb{S}$ be the SCM of a surface $S_{s,(s=1,2)}$ onto a unit sphere; $p_{i,i=1\dots n}$, and $q_{i,i=1\dots n}$ are landmarks defined on both surfaces, respectively, where p_i corresponds to q_i . Following (Lui et al., 2007; Y. Wang et al., 2005), the harmonic energy function that minimizes both distortion and landmark differences is given by Equation (2.39):

$$E(f_1) = \sum_{[u,v] \in K} k_{uv} \|f_1(u) - f_1(v)\|^2 + \gamma \sum_{1 \leq i \leq n} \|f_1(p_i) - f_2(q_i)\|^2 \quad (2.39)$$

where $k_{uv} = \cot \alpha + \cot \beta$ with α and β are the opposite angles of an edge $[u, v]$; γ is a balancing factor. The correspondence, which registered landmarks of S_1 to S_2 , is given by $g = f_2^{-1} \circ f_1$. It may be observed that (2.39) can be scaled to different mesh sizes, $\|K\|$, and does not depend on physical coordinates. Therefore, this mapping could handle variability in both the shape and size of the liver.

It was pointed out (P. T. Choi, Lam, & Lui, 2015) that with conventional approaches, numerical instability may occur near the spherical poles (where a large number of vertices are mapped onto a small region), and near the landmarks. These result in severe distortion and even loss of bijection. To resolve these issues, a Gauss map (Gu et al., 2004; Y. Wang et al., 2004) was first applied to initialize uniform distribution, then the Fast Landmark Aligned Spherical Harmonics (FLASH) proposed by Choi et al. (P. T. Choi et al., 2015) were utilized. This linearized Equation (13), based on the north-south poles iterative model, while adjusting the Beltrami differential to recover bijective mapping. The detailed implementation of FLASH can be found in (P. T. Choi et al., 2015).

In this study, a liver surface was assumed topologically spherical and hence, of genus-0 form. Thus, it was possible to determine a conditioned SCM, when provided with a few anatomical landmarks, that aligned two corresponding liver surfaces (e.g., that of donor and recipient). The potential application of such low-distortion mapping is demonstrated in a simulation by faithfully projecting functional resections of one liver onto another during a preoperative hepatectomy.

2.7 Liver and general surgical simulation

The surgery in the past based on the experiments of surgeons in which the liver model, vessel and liver's structure were built in their mind based on medical image. This not only led to lack of sharing information between members in team but also subjective and instable. The development in medical and computer-assisted liver surgery allowed visualization of objects in 3D environment. It was reported that (Nakayama et al., 2017) the using of preoperative simulation also allow to reduce surgery time of repeated hepatectomy and segmentectomy. Generally, it includes three sub-techniques: 3D reconstruction, volumetric analysis and surgical simulation (Mise et al., 2013).

Surgical simulation has been developed since 2005 and used for liver tumor surgery in 2007 (Oshiro & Ohkohchi, 2017). Afterward, there were several software have been available for liver simulation, such as SYNAPSE VINCENT (Fujifilm medical, Japan), HepaVision (Mevis, Germany), syngo.via (Siemens Co., Germany). These tools enabled to visualize the structure of liver and vascular network. However, the using of this tool depends on the experiences of user. For example, SYNAPSE VINCENT and syngo.via, user is required to select the vessel or trace the portal vein or hepatic vein for volumetry analysis. While HepaVision software is an online service,

which the operation is performed by host of software. To non-rigid modeling, LiverSim (Oshiro & Ohkohchi, 2017; Oshiro et al., 2015) was developed for tracking the deformation of parenchyma and vessel. This tool enabled to visualize, change color, deform, and track the motion. Another software, Myrian (France) allowed automatically measure volume of right lobe, however it takes 10-15 min to access the volume of graft (Bozkurt et al., 2019). However, surgeon is required to draw tracing lines in a few 2D images, then the hyperplane is obtained. Dr. Liver (Humanopia Co. Ltd, Pohang, Korea), a software for surgical planning (Xiaopeng Yang, Wonsup Lee, Younggeun Choi, & Heecheon You, 2012; X. Yang, Yang, Yu, et al., 2018) was developed. It includes sub-models such as liver extraction, vessel segmentation, virtual resection, etc.... However, the separation of right and left lobes is performed by a 3D cutting sphere. In comparison to other tools which only supported to correctly measure liver and GV (X. Yang, Yang, Yu, et al., 2018), both Dr. Liver and syngo.via allowed to estimate GW. The former used regression equation, while the latter based on liver volume, volume of blood and liver density to calculate GW. To our knowledge, although the available software allowed to measure the GV or GW, the compatible of graft shape is not considered. It was reported that (Kasahara et al., 2008; Namgoong et al., 2020; Schukfeh et al., 2018), the shape graft will affect the success of surgery in segment II/III in infants. For example, the “*thickness-to-anteroposterior diameter in the recipient’s abdominal cavity ratio*” is less than 1.0%, the donor may be required to reduce size of graft. Thus, this study may help improve the available systems by supporting of estimation of graft shape.

CHAPTER 3

METHODOLOGY

This chapter presents three main contents: Liver segmentation, functional segmentation, and parameterization.

Section 3.1 focuses on the building of a semi-automatic liver segmentation method. It begins with an introduction of two schemes and proposed workflows. A novel framework for liver segmentation using probability map, relaxation labeling, GC and anatomy-based constrain model, referred as model 1, is presented in next section. Some improvements of model 1 based 3-D relaxation labeling, and anisotropic GC are proposed to increase the accuracy of system, referred as model 2. Two most popular datasets for liver segmentation are used for testing algorithm, followed by a description of some segmentation metrics that used to quantitatively evaluate the performance of proposed techniques.

Section 3.2 describes the proposed scheme, which was based on subject specific hepatic vascular network and by using differentiable geometry computing.

Section 3.3 presents the conformal parameterization of liver and application of estimation of the GV size in LDLT.

3.1 Liver segmentation

3.1.1 Proposed schemes

In this thesis, there are two schemes are proposed for segmentation liver. They are described as followings:

In the first scheme, the local mean and standard derivation of a seed point specified by user will be utilized to build probability map based on multivariable normal distribution model. In the next step, an adaptive thresholding technique, Otsu's method, is applied to probabilistic image to extract the largest contour among images in CT volume. Simultaneously, relaxation labeling, a labeling algorithm based on contextual information, is used to enhance the probabilistic map. It aims to reduce the ambiguity of the boundary between liver and surrounding tissues. Then, GC is automatically implemented on enhanced probabilistic image to segment liver. Due to the complexity of the anatomy of liver, both of segmented livers and the largest contour extracted from previous procedures are integrated into last step to remove over-segmentation before the 3-D liver model is reconstructed.

The latter scheme, there are two improvements to be introduced. The first improvement is embedded into the enhancing process of probabilistic map, whereas the second one is taken place in the segmenting step conveyed by GC. The relaxation labeling algorithm mentioned in above considers the contextual information of a pixel from its neighbors in the same slice, so it is 2-D relaxation labeling. In medical imaging, the image of a specified organ is captured in continuous ordered slices, the distance between slices is fixed and typically small, and object shape do not remarkably differ among them. Therefore, the contextual information of pixels in adjacent slices could be used to support for the calculation of the probabilistic map of a specified pixel.

Such technique is referred to as 3-D relaxation labeling in this study. The next improvement is relevant to computing of GC energy function. The main idea is the using anisotropic diffusion of intensity at the edge of object to build boundary term in max flow/min cut algorithm. The workflows of proposed schemes are illustrated in **Figure 3.1** and **Figure 3.2**.

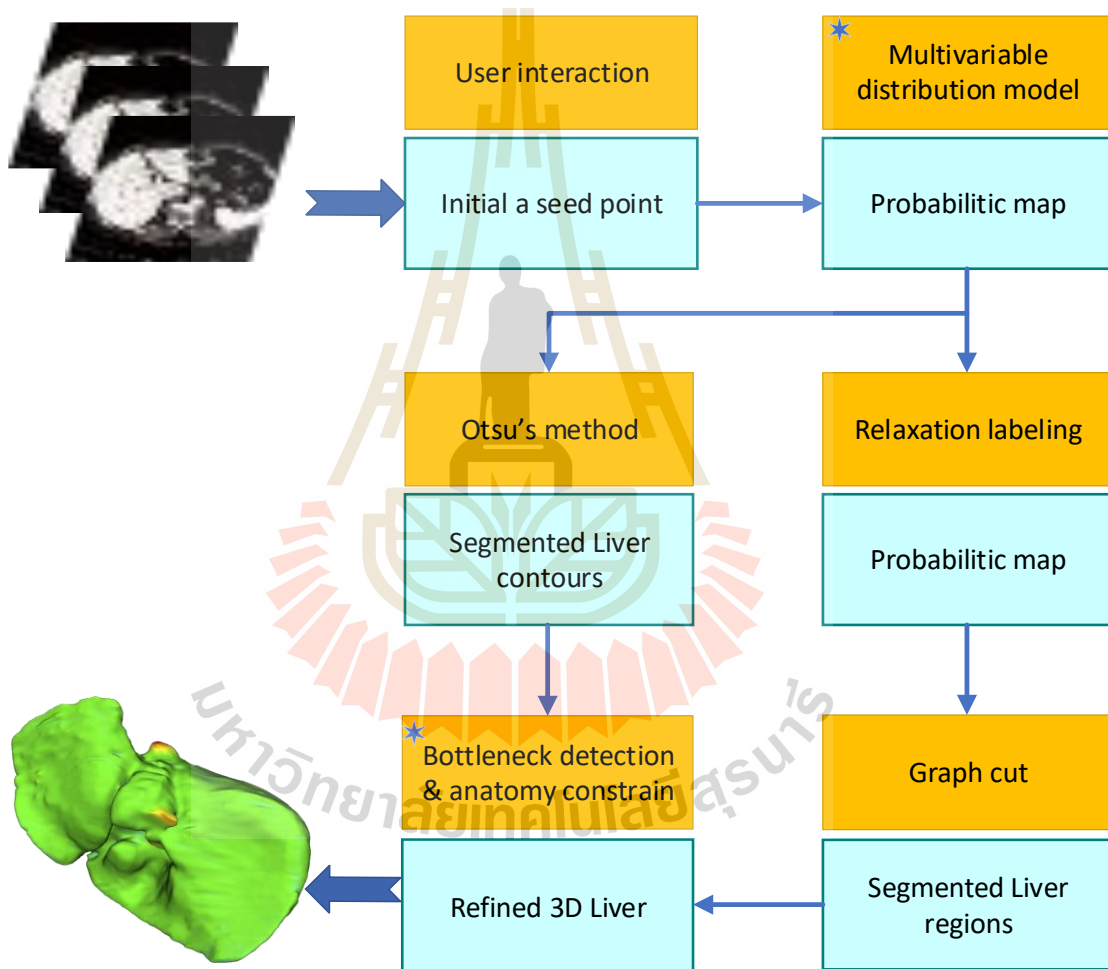


Figure 3.1 The workflow of proposed method by model 1.

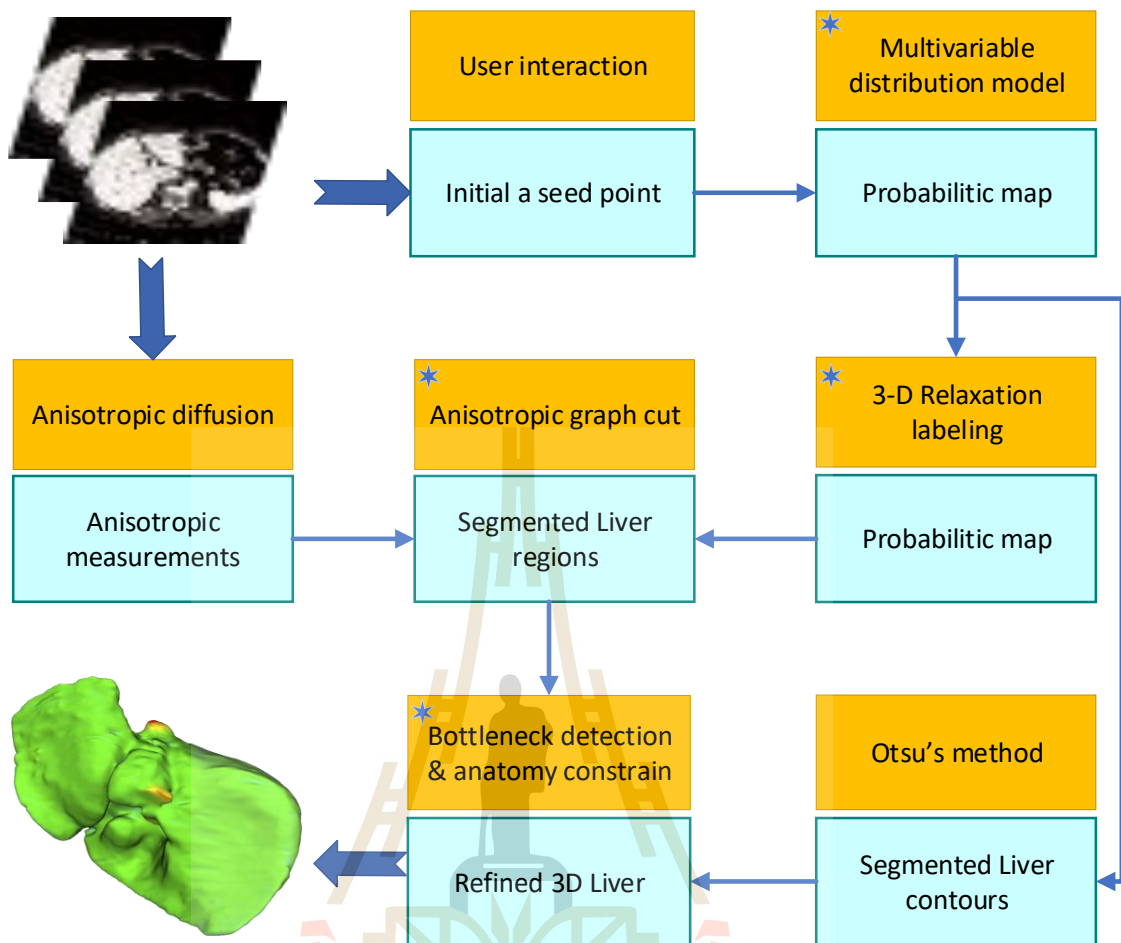


Figure 3.2 The workflow of proposed method by model 2.

In both schemes, the input is a series of abdominal images. Orange blocks present for the processes. Cyan blocks present for results of corresponding processes. The output is the 3-D Liver. The details of proposed method and its improvement are presented in next section.

3. 1. 2 Probabilistic model

It is noted that the input of the system comes from the probability a pixel belongs to liver region based on specified features. In(Liao et al., 2017; Liao et al., 2016), Liao et al directly used intensity value to build appearance and PCA model. Peng (Peng et al., 2015), Lu (F. Lu et al., 2017) and (Zheng et al., 2017) based local binary pattern (LBP) and an improved of LBP called by VAR, proposed by Ojala et al (T. Ojala et al., 2002), which are invariant to grey scale difference and rotation. It differs from other methods in that, instead of using intensity value, this study characterizes each pixel by two features: mean and standard deviation (SD) of this pixel and its neighbors. In order to build the initial probability map of liver region, a significant but simple method, called by mean - standard deviation based multivariate Gaussian distribution model is proposed. This process is separated into two-sub steps: model instantiation and probabilistic map building.

Model instantiation: A probability of a point \mathbf{p} being of liver was determined based on a patch (Φ) of size $m \times n$ centered by that point. To begin with, for each pixel $\mathbf{q}_i \in \Phi$, the local mean (μ_i) and standard deviation (σ_i) of the intensities, within its $m \times n$ neighbors (Ω) are computed. In this study, the extent of neighbors in x and y directions, i.e., m and n , respectively, were equally set to 11 pixels (approx. 2.75 – 4.00 mm, either side). The local (μ_i) and standard deviation (σ_i) were then averaged over the members, $\mathbf{q}_i \in \Phi$. The resultant averages constituted to a 2D vector values characterizing the given point \mathbf{p} , as expressed in (3.1)

Let a vector function $\mathbf{f}: \mathbf{R}^2 \rightarrow \mathbf{R}^2$ map a point \mathbf{p} to its feature space as follows:

$$\mathbf{f}(\mathbf{p}) = \left[\frac{\sum_{i \in \Phi} \mu_i}{\|\Phi\|} \quad \frac{\sum_{i \in \Phi} \sigma_i}{\|\Phi\|} \right]^T \quad (3.1)$$

where local mean (μ_i) and standard deviation (σ_i) were evaluated for each $\mathbf{q}_i \in \Phi$ over its neighbors (Ω).

A normal distribution of a k -dimensional random variable (RV), expressed by $\mathbf{f} = [f_1, f_2, \dots, f_k]^T$, was defined as:

$$\mathcal{P}(\mathbf{f}) = \frac{1}{2\pi^{k/2} |\Sigma|^{1/2}} e^{-\frac{1}{2}(\mathbf{f}-\bar{\mathbf{f}})^T \Sigma^{-1} (\mathbf{f}-\bar{\mathbf{f}})} \quad (3.2)$$

where $\bar{\mathbf{f}} \in \mathbb{R}^k, \Sigma \in \mathbb{R}^{k \times k}$ were the mean and covariance matrices of \mathbf{f} , respectively. It was computed from a set of few manually specified points. In this study, they were evaluated by (1) at the seed point. Provided the definition of a vector function of feature, $\mathbf{f}(\mathbf{p}) = [f_1, f_2]^T$, having $k = 2$ dimensions, the corresponding covariance matrix was thus given by:

$$\Sigma = \begin{bmatrix} \text{cov}(f_1, f_1) & \text{cov}(f_1, f_2) \\ \text{cov}(f_2, f_1) & \text{cov}(f_2, f_2) \end{bmatrix} \quad (3.3)$$

Probabilistic map building: For each pixel \mathbf{p} in image (I), the feature $F = [f_1, f_2]^T$, where $\bar{\mathbf{f}}$ is mean and SD of a path size of $m' \times n'$ centred at \mathbf{p} , are determined, then the probability of pixel is computed using MGM. The detail of building the model is described in **Table 3.1**.

Table 3.1 Process of building a multivariate probability density function.

Input	Seed point \bar{p} , image I
	Build model let Φ be a patch of size of $w \times w$ pixels, centered at \bar{p} foreach pixel q_i in patch Φ do let Ω be a patch size of $w \times w$ pixels, centered at q_i compute mean (μ_i) and standard deviation (σ_i) at q_i end for calculate $f(\bar{p}) = [\bar{f}_1 \quad \bar{f}_2]^T$, following (3.1) calculate Σ , following (3.3) Build probabilistic map foreach pixel p in image I do let Φ be a patch of size 11×11 pixels, centered at p foreach pixel q_i in a patch Φ do let Ω be a patch of size 11×11 pixels, centered at q_i compute mean (μ_i) and standard deviation (σ_i) at q_i end for calculate $f(p) = [f_1 \quad f_2]^T$, following (3.1) calculate $\mathcal{P}(f)$, for the point p , following (3.3) end for
Output	The probability density function of image I

3. 1. 3 Relaxation labeling

It has been well accepted over many decades that relaxation labeling (RL) is a probabilistic labeling technique for an object based on contextual information (Rosenfeld, Hummel, & Zucker, 1976). Namely, an initial local probability of an object belongs to all classes is given, then an iteration will be performed to update this value using both the previous probability of current object and the previous values of its neighbors until the difference error between current and estimated value is less a given threshold or having been run for a number of given iterations. Its aim is to reduce the ambiguity of the labeling for an object. This method has been widely used in several of applications such as line and curve enhancement (Zucker, Hummel, & Rosenfeld, 1977), edge detection (Iyengar & Deng, 1995), image segmentation (Hansen & Higgins, 1997; Loukas & Linney, 2005), point matching (J. H. Lee & Won, 2011). A review of relaxation labeling and its applications can be found in (Kittler & Illingworth, 1985; Richards, Landgrebe, & Swain, 1981). Unlike other works, RL was adopted here to improve initial pixel-wise classification, obtained from the prior step. Since basic elements and their definitions can be found in (Rosenfeld et al., 1976), this section elaborates in detail only supports and compatibility functions

Two principal objects considered in RL algorithm in binary labeling problem are pixels of image I and a set of classes \mathcal{C} . Assume that, at t time, $\mathcal{P}_p^t(\lambda)$ is the probability a pixel $p \in I$ assigned label $\lambda \in \mathcal{C}$, according to the properties of probabilistic theory, we have

$$\sum_{\lambda \in \mathcal{C}} \mathcal{P}_p^t(\lambda) = 1, \forall p \in V, \mathcal{P}_p^t(\lambda) \in [0,1] \quad (3.4)$$

Updating of the probability for pixel p by label λ at stage $t + 1$ is computed as follow (Rosenfeld et al., 1976)

$$\mathcal{P}_p^{t+1}(\lambda) = \frac{\mathcal{P}_p^t(\lambda)(1 + S_p(\lambda))}{\sum_{\mu \in \mathcal{C}} \mathcal{P}_p^t(\mu)(1 + S_p(\mu))} \quad (3.5)$$

where $S_p(l)$ is the support function for pixel \mathbf{p} by a label, l .

Let \mathcal{N}_p be a set of neighbors of \mathbf{p} and $r_{pq}(\lambda, \mu)$ be the compability between pixels \mathbf{p} and $\mathbf{q} \in \mathcal{N}_p$ by labels λ and μ , respectively. The support function was derived from the compability by using following equation.

$$S_p(\lambda) = \sum_{q \in \mathcal{N}_p} w_{pq} \sum_{\mu \in \mathcal{C}} r_{pq}(\lambda, \mu) \mathcal{P}_q^t(\mu) \quad (3.6)$$

where $r_{pq}(\lambda, \mu)$ was 1, if λ and μ were of the same class, or -1 otherwise. The inter-object weight w_{pq} was defined as an inversed Euclident distance between \mathbf{p} and \mathbf{q} . It was also normalized such that its sum over the neighbours \mathcal{N}_p were unity.

The denominator in (3.5) guarantees the properties of probability, it means that (3.5) is always satisfied. A detail of discussion on the accuracy of (3.5) can be found in (Richards et al., 1981).

To ensure the performance of the system, the neighborhood size was set to only within one-pixel proximity in 8 directions. It is also worth noting that, with trivial features, pixel-wise classification may result in vague definitions along connective tissues. To sufficiently enhance such separation prior to the next stage, probabilistic

convergence and hence finalized labeling, was not yet required here. The RL was therefore let to update only for a few iterations. **Figure 3.3** depicted an example configuration of pixel p and its neighbor q , the initial probabilistic map, and the resultant RL enhancement. It is clear that fallacies along the boundary were effectively reduced (red circles).

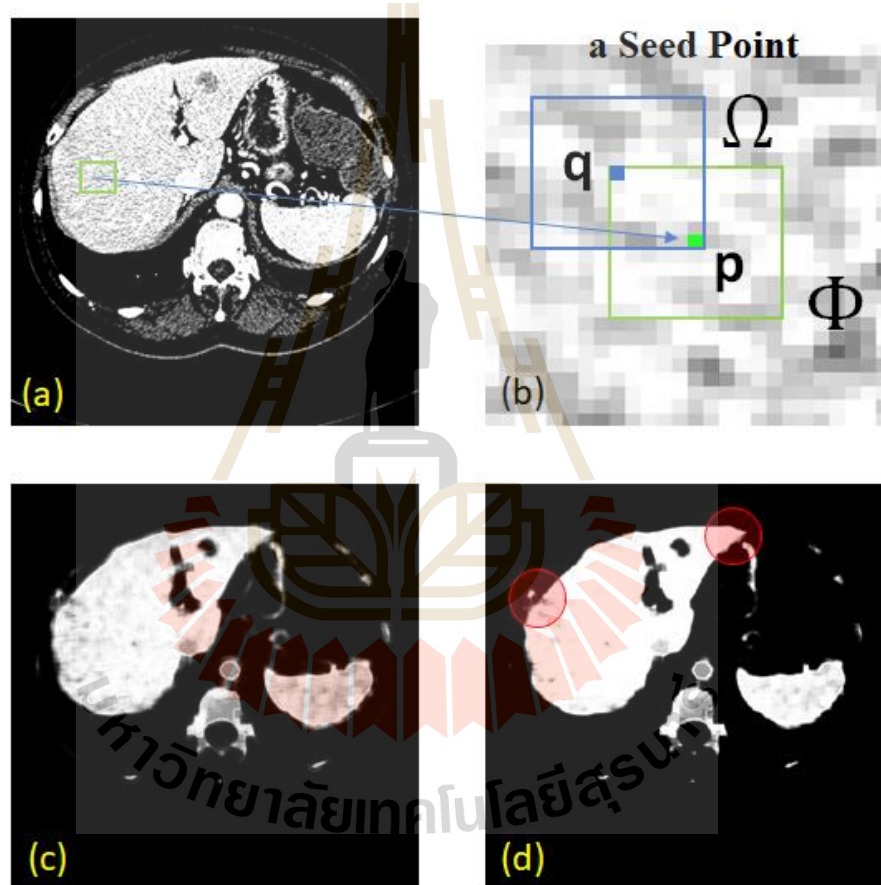


Figure 3.3 An example of probability map and relaxation labeling

The original CT image (a) with a seed point (green) is shown in (b), the probability map image and RL enhanced results are shown in (c) and (d), respectively. The probability values from 0 to 1 are scaled to 0 to 255 for visualization purpose.

3.1.4 Graph cut

Consider an undirected graph denoted by $\mathcal{G} = \{\mathcal{V}, \mathcal{E}\}$, where \mathcal{V} is a set of vertices and \mathcal{E} is the edges connect two vertices by a nonnegative weight w . According to (Boykov & Jolly, 2001), a minimum cut (referred as min-cuts) partitions \mathcal{V} into two disjoint subsets \mathcal{V}_1 and \mathcal{V}_2 ($\mathcal{V}_1 \cup \mathcal{V}_2 = \mathcal{V} \wedge \mathcal{V}_1 \cap \mathcal{V}_2 = \emptyset$) is given by $\mathcal{K} \subset \mathcal{E}$ so that the following function is minimized $|\mathcal{K}| = \sum_{e \in \mathcal{K}} w_e$

In binary image segmentation problem, \mathcal{V} now corresponds to a series of pixels p in image I and \mathcal{E} is the links of two adjacency pixels. Additionally, there are two special terminals which present for the *object* and *background* are added to graph, called by s (source or object) and t (sink or background). Two kinds of links are considered in the graph. The first kind of link denoted by *n-link* is the edge connecting two adjacency pixels within an image. The other kind connecting two terminals to all pixels is denoted by *t-link*. Assume that each pixel $p \in I$ is labeled to one of considerable labels l_p in binary label set \mathcal{L} , $\mathcal{L} = \{c_1, c_2, \dots, c_{|I|}\}$, $c_i \in \{0: \text{object}, 1: \text{background}\}$ Boykov et al (Boykov & Jolly, 2001; Boykov & Kolmogorov, 2004) proposed an efficient algorithm known as Min-Cut/Max-Flow for solving the min-cuts problem by minimization combinational energy (Boykov & Kolmogorov, 2004), i.e.,

$$E(\mathcal{L}) = \alpha \sum_{p \in I} R(c_p) + (1 - \alpha) \sum_{p \in I, q \in \mathcal{N}_p} B(c_p, c_q) \cdot T(c_p \neq c_q) \quad (3.7)$$

where α is the balanced coefficient between region $R(c_p)$ and boundary term $B(c_p, c_q)$. If $\alpha > 0.5$, the region information is more important than boundary information and vice versa. The size of labels, $|I|$, equaled the number of pixels in the image.

\mathcal{N}_p is defined following that in section 3.1.3. The conditional probabilities in (3.7) was given as follow (Boykov & Jolly, 2001),

$$R(\mathcal{C}_p = c) = 1 - \mathcal{P}(p|c) \quad (3.8)$$

where c was a binary label assigning 0 or 1 to either a background or object pixel, respectively. The probabilistic map $\mathcal{P}(p)$ was obtained from the previous stage (3.5)

The second term is directly obtained from the intensity and the distance between two adjacent as follow (Boykov & Jolly, 2001),

$$B(c_p, c_q) = \exp\left(-\frac{(I_p - I_q)^2}{2\delta^2}\right) \cdot \frac{1}{dis(p, q)} \quad (3.9)$$

where I_p, I_q are the intensity value at pixel p and q , δ is the noise distribution, and $dis(p, q)$ is the Euclidian distance from p to q .

3.1.5 Bottleneck detection and anatomy-constraint

It is known that the liver has a smooth boundary. Additionally, the difference between the shape of liver in two adjacency slices in a volume depends upon the distance between these slices. RL enhanced probabilistic map and graph-cut provided a reliable and efficient segmentation of the liver, based on intensity distribution of the pixels and their spatial relationship. Thus far, due to rather complex geometry of the liver and its similar X-ray absorption properties to other organs, there remained over-segmentation. This led to low accuracy, commonly found in many existing untrained systems or those with inadequate samples. It was observed that over-segments often appeared as nodal shapes on the liver boundary. To further improve the results,

this study thus imposed an anatomical control over the segmented result, based on bottleneck detection and contour constraint (BN-CC)

Bottleneck detection

According to Wang et al (H. Wang, Zhang, & Ray, 2012), a potential bottleneck in 2-dimensions space is determined by a cost function (\mathcal{E}), defined by a pair of points (\mathbf{q}, \mathbf{p}) and $\mathbf{p} \neq \mathbf{q}$, such that

$$\mathcal{E} = \frac{\text{dist}(p, q)}{\min(\text{lenght}(p, q), \text{lenght}(q, p))} < \mathcal{T}_b \quad (3.10)$$

where $\text{dist}(p_1, p_2)$ was the Euclidian distance between p and q ; $\text{lenght}(p, q)$ and $\text{lenght}(q, p)$ were the length in clockwise direction along to contour; \mathcal{T}_b is a predefined threshold. For a liver shapes, it was typically set to 0.60. A drawback of the method was that as the threshold increased, it tended to smooth out the contour. In some instances, anatomical features such as that on the left lobe was partially brushed off. On the other hand, reducing the value caused substantial over-segments, mostly near the ligaments. In addition, to avoid concerns on contour modeling, a generic polygonal approximation was applied to extract key points. Depending on image resolution, this may result in too many points being generated. To simultaneously tackle these problems, this study introduced a criterion on a candidate point based on its outer angle. Specifically, only if its exterior angle was less than a given threshold, it would be considered in bottleneck detection, otherwise it remained on the segmented contour. In this study the threshold for nodal point candidate was set to 150° . **Figure 3.4** illustrates two examples of candidate point selections. Segments ($\mathbf{p}_1, \mathbf{p}_2$) and ($\mathbf{p}_3, \mathbf{p}_3$) had cost functions of 0.50 and 0.40, respectively, and would be both identified as bottlenecks. As such,

this would have incorrectly removed a salient point at the end of left lobe (b). However, only the segment (a) (fuzzy liver edge) satisfied the nodal candidate outer angle criterion and hence was removed but leaving the segment (b) untouched.

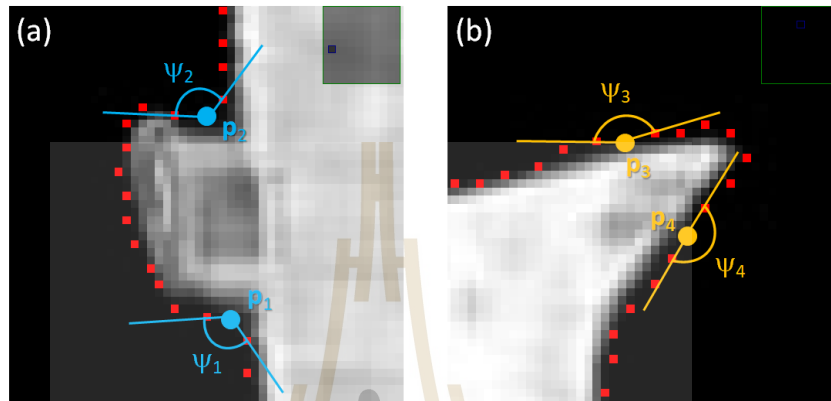


Figure 3.4 Bottle neck detection using exterior angle constraint.

Contour constraint

Nonetheless, it was found during a preliminary experiment that depending on the thresholds, not all bottlenecks could be successfully removed. Information on adjacent slices was thus also considered in post-processing. With modern CT imaging, slice thickness was typically small, and object shapes do not differ much between adjacent planes. Thus, a contour constraint was imposed on the segmented regions. To begin with, each probabilistic map of two adjacent slices were first converted to binary images, by using an Otsu's method. Complementary contours would be extracted from these images. Let $C_i = \{c_{i1}, c_{i2}, \dots\}$ and $C_j = \{c_{j1}, c_{j2}, \dots\}$ be the sets of contours (including bottleneck candidates), extracted from i^{th} and j^{th} slices, respectively. For any $(c_{ik}, c_{jl}) \in C_i \times C_j$ that satisfied the condition:

$$\mathcal{S} = \frac{|c_{ik} \cap c_{jl}|}{\min(|c_{ik}|, |c_{jl}|)} < \mathcal{T}_c \quad (3.11)$$

then the contour with the least area, i.e., $|c_{mn}|$, would be removed from the respective slice. In the preliminary experiment, a suitable threshold was empirically estimated by using simple linear least-square method. The suggested threshold \mathcal{T}_c was given as a function of slice distance, d_z .

$$\mathcal{T}_c = 0.8 - 0.05(d_z - 1) \quad (3.12)$$

To avoid inconsistency due to slice orders, post-processing started from a slice with the largest contour and stepped one slice at a time in both directions along the z axis. For any pair of slices being processed, BN-CC was first applied, following (3.9) and remaining contours were constrained, i.e., removed subject to the condition, given by Eq. (3.10) and (3.11).

Let $\mathcal{C}_i = \{c_{i1}, c_{i2}, \dots, c_{in}\}$ and $\mathcal{C}_j = \{c_{j1}, c_{j2}, \dots, c_{jm}\}$ be the set of contours in current slice and previous slice respectively; $S(c_{uv})$: area of the contour c_{uv} ; $S(c_{uv} \cap c_{u'v'})$: area of the intersection contour of c_{uv} and $c_{u'v'}$. The contour-constraint algorithm is showed as **Table 3.2**.

Table 3.2 The contour-constraint algorithm

Input	$\mathcal{C}_i, \mathcal{C}_j, \mathcal{T}_c$
	init $\mathcal{C} = \emptyset$
	foreach c_{ik} in \mathcal{C}_i

If exist a $c_{jl} \in \mathcal{C}_j$ such that $\left(\frac{S(c_{ik} \cap c_{jl})}{\min(S(c_{ik}), S(c_{jl}))} \geq \mathcal{T}_c \right)$

Add c_{ik} to \mathcal{C}

end if

End for

Output	\mathcal{C}
--------	---------------

Figure 3.5 demonstrates some examples of approximated contours from slices i and $i - 1$ and those after applying BN-CC. In the top row (a) – (c), there were 2 bottlenecks ($\mathbf{p}_1, \mathbf{p}_2$) and ($\mathbf{p}_3, \mathbf{p}_4$), whose areas were 242 and 52 pixels, respectively. They would be both detected by Eq. (9). When intersecting with the one in previous slice, whose area was 42670 pixels, the intersected areas were 42 and 51 pixels, respectively. With \mathcal{T}_c set to 0.8 (i.e., $d_z = 1$), only the former would be removed (circled in red), leaving the latter (circled in blue). Likewise, not all bottlenecks were removed by Eq. (3.9) in the bottom row (d) – (e), unless they satisfied Eq. (3.10).

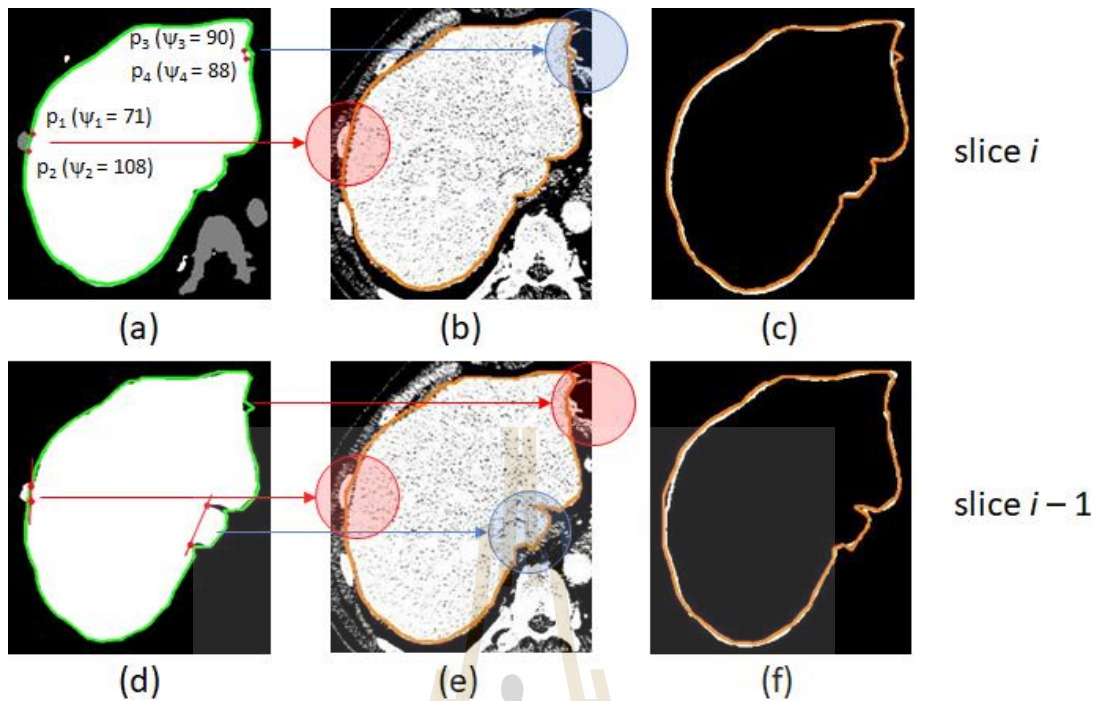


Figure 3.5 The performance of BN-CC

The previous and current contours are drawn in green and orange colors, respectively. The ground truth is drawn white. The first column (a and d) shows the bottle neck detecting in CT image after applying graph-cut. The second column (b and e) shows the results after applying adjacent contour constraint. The last column (c and f) shows the valid contours. Red and blue circles indicate the removed and remaining bottlenecks, respectively.

Figure 3.6 illustrates a parallel processing of BN-CC. The algorithm begins at the slice contains the largest contour and stepped one slice into both direction along the z axis.

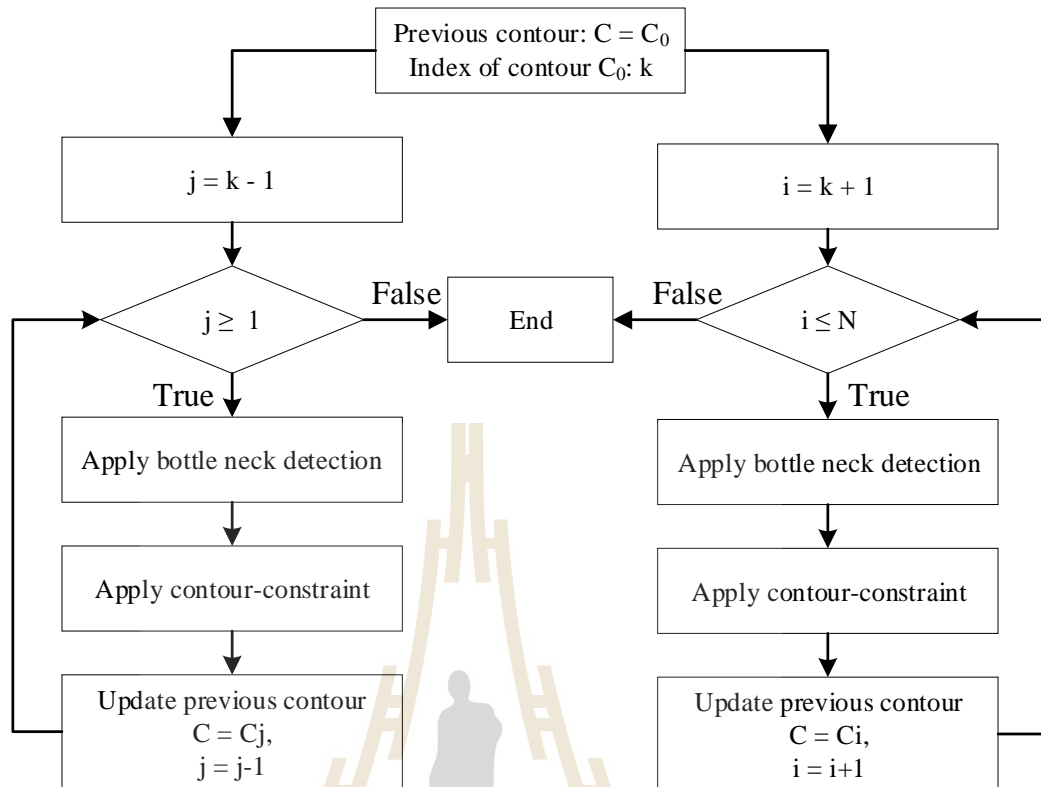


Figure 3.6 The flow chart of post processing

3.1.6 Improvements

3.1.6.1 3-D relaxation labeling

In 2-D image, the number of neighbors is usually set to 8, thus the estimated probability of each pixel is computed from 8-neighbors in this image. Motivated by the fact that CT image has low intensity, and the boundary of each tissue is not clear, but the liver is largest object in abdominal CT and shape of liver in adjacency slices changes lightly. An improved method for RL, called by Multi-slice Relaxation labeling MRL in CT image, is proposed. Instead of using single slice, we calculate support value for each pixel p in one slice from p 's neighbors in this slice and adjacency slices.

Let Π_{up} be a set neighbors of pixel p in slice u and its neighbors. It is now possible to rewrite the support for label λ at pixel p as follow

$$S_p(\lambda) = \sum_{q \in \Pi_{up}} w_{pq} \sum_{\mu \in \mathcal{C}} r_{pq}(\lambda, \mu) Pr_q(\mu) \quad (3.13)$$

The coefficient w_{pq} is the inversion of distance between pixel p in slice u and pixel q and slice v and can be defined by the equation:

$$w_{pq} = \frac{1}{\text{dist}(p, q)} \quad (3.14)$$

if pixel p and q are in the same slice

$$w_{pq} = \frac{1}{\sqrt{[\text{dist}(p, p')]^2 + [\text{dist}(p', q)]^2}} \quad (3.15)$$

if pixel p is in slice u , and q is in slice v

with p' is a pixel in slice v corresponds to position of p , and (x, y) is the location of pixel in 2D-space; d_z slice thickness; $\text{dist}(q, p') = d_z |u - v|$. **Figure 3.7** illustrates computing of the weight.

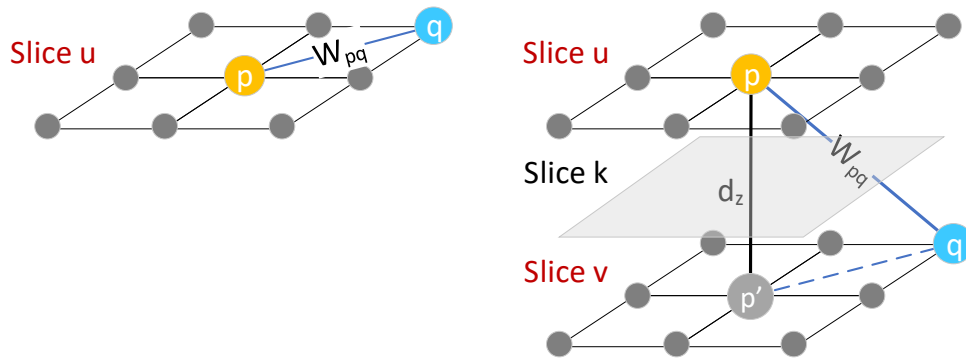


Figure 3.7 Two cases of neighbours of pixel p

A high value of $|u - v|$ corresponds to a low value of w_{pq} . It means that the support of slice v for slice u is stronger than slice v' , $\forall v' > v$. As proven in (Rosenfeld et al., 1976) that, the value of w_{pq} should satisfy $\sum_{q \in \Pi_{up}} w_{pq} = 1$ for all pixels p and it is normalized by the following equation

$$w_{pq} = \frac{w_{pq}}{\sum_{q' \in \Pi_{up}} w_{pq'}} \quad (3.16)$$

Given the number of elements in Π_{ui} , a dictionary of all weights (\mathcal{W}) parameterized by v and q can be firstly built and normalized. Then, computing of the support value is trivial, i.e., looking for the value of w_{pq} in dictionary. Let $\mathcal{P}^{t=0}$ be the initial probability of all pixels in image I , the process of 3-D RL for image I is described by **Table 3.3**.

Table 3.3 The algorithm of 3-D RL

Input	$\mathcal{P}^{t=0}, I, \mathcal{C}, d_z, T$
-------	---

	Build dictionary of weights \mathcal{W} by (3.14) or (3.15)
	Normalize \mathcal{W} by (3.16)
	for $t=1$ to T do
	foreach pixel p in I
	Compute the support for pixel p by (3.13)
	Update \mathcal{P}_p^t by (3.5)
	end for
	end for
Output	$\mathcal{P}^{t=T}$

3.1.6.2 *Anisotropic measurement*

Low-pass filter has been one of most common techniques used to denoise in image based on local gradients. However, it reduces the details of important information and blurs the boundary and corner in image. To tackle this issue, Yang et al (G. Z. Yang, Burger, Firmin, & Underwood, 1996) proposed an efficient method, called by structure-adaptive anisotropic filter, for smoothing image without decrease image contrast. The main concept of this approach is to build an elliptical kernel, whose orientation and shape adapt to the local information of each pixel in image.

Firstly, the orientation of kernel at pixel $p = (x, y)$, defined as the angle between normal vector \vec{n} of kernel and horizontal axis, is calculated based on local intensity as following equation:

$$\theta(p) = \frac{1}{2} \operatorname{atan} \left(\frac{\iint_{\mathcal{N}_p} 2f'_x f'_y \, dx dy}{\iint_{\mathcal{N}_p} ((f'_x)^2 - (f'_y)^2) \, dx dy} \right) + \frac{\pi}{2} \quad (3.17)$$

Then, anisotropic measurement and corner strength, used to estimate the shape of kernel are given respectively as follows:

$$g(p) = \frac{\left(\iint_{\mathcal{N}_p} ((f'_x)^2 - (f'_y)^2) \, dx dy \right)^2 + \left(\iint_{\mathcal{N}_p} 2f'_x f'_y \, dx dy \right)^2}{\left(\iint_{\mathcal{N}_p} ((f'_x)^2 + (f'_y)^2) \, dx dy \right)^2} \quad (3.18)$$

$$c(p) = (1 - g(p)) |\nabla f(p)|^2 \quad (3.19)$$

where $f'_x = \frac{\partial f}{\partial x}$, $f'_y = \frac{\partial f}{\partial y}$, $\nabla f(p)$ is the gradient at pixel p in image f ; \mathcal{N}_p is defined in section 3.1.3.

The shape of kernel at pixel p presented by two coefficients (s_1, s_2) is determined as follow:

$$s_1(p) = \frac{r}{1 + \frac{c(p)}{\lambda}} \quad (3.20)$$

$$s_2(p) = (1 - g(p)) \frac{r}{1 + \frac{c(p)}{\lambda}} \quad (3.21)$$

where r is the support radius of kernel, and λ is the normalization factor controls smoothing of the corner and boundary which is usually set to 75% of maximum value of corner strength. For flat regions, $s_1 = s_2$, $g \approx 0$, thus the shape of kernel is a circle,

whereas for inhomogeneous regions such as corner or boundary, $s_1 > s_2, 1 \geq g > 0$ and the kernel has ellipse form.

As shown in (3.7) that, the intensity value plays vital role in boundary function meanwhile the distance between two pixels is considered as weight. For example, the distance from a pixel to pixels in top, bottom, left, and right is the same. Take advantage of anisotropic measurement, it can be seen that if a pixel lies in homogenous area, the anisotropic measurement will be low, while it is high at the boundary (as shown in **Figure 3.8**). Thus, the boundary energy in combination with local pattern compatibility now can be formulated as the following equation:

$$B(c_p, c_q) = \exp\left(-F(p, q) \frac{(I_p - I_q)^2}{2\delta^2}\right) \frac{1}{dis(p, q)} \quad (3.22)$$

With $F(p, q) = \max(g(p), g(q))$

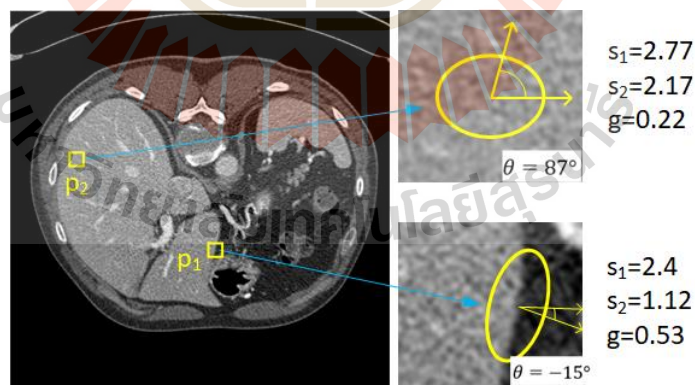


Figure 3.8 An example of anisotropic

(The normal vector direction (θ) and anisotropic measure(g), and shape coefficients (s_1, s_2) at p_1 and p_2 . However, $g(p_1) > g(p_2)$, this indicates

that p_1 lies in the boundary meanwhile p_2 belongs to a likely homogeneous region. The support radius r is set to 3 and scaled for visualization purpose).

3.2 Functional segmentation for preoperative liver

This work proposes an integration of salient features of a liver surface and concise representation of its vascular networks, both automatically reconstructed from 3D CT. This information was incorporated, as functional definitions and constraints, into segmenting a liver, strictly according to Couinaud's scheme. Compared to the works previously discussed, the proposed method was able to completely label all eight functional segments, including caudate, at greater precision, but with minimal user interaction involved.

Overview of the proposed scheme is depicted in **Figure 3.9**. Given volumetric CT images of a 3D liver scan, the liver and interior vasculature were first extracted automatically by using a CAD software written in the laboratory, based on off-the-shelf algorithms. Next, centerlines traversing through the vascular networks were reconstructed, while differential geometric properties were computed on the extracted liver surface, simultaneously. Subsequently, the surface properties would be analysed and used to characterize key anatomical landmarks, i.e., gallbladder fossa and inferior ridge sections. Later, a set of cutting planes were defined, based on vascular passages and landmarks. Finally, functional Couinaud's segments of the liver (I–VIII) were determined, by means of combinatorial operations on the liver surface and geometric descriptors.

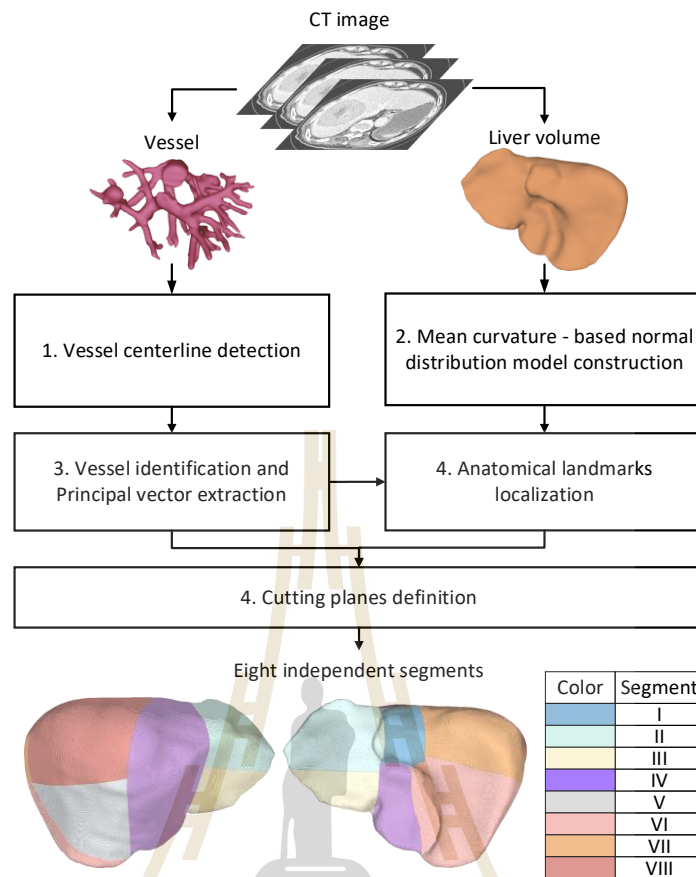


Figure 3.9 Key steps of functional liver segmenting scheme.

3. 2. 1 Liver and vessels segmentation

Segmenting a liver and its interior vascular network from volumetric CT is a challenging task due to inhomogeneous intensity and ambiguous boundaries in some areas. Several methods have been proposed in the literature (Moccia, De Momi, El Hadji, & Mattos, 2018; Moghbel, Mashohor, Mahmud, & Saripan, 2018). However, since their detailed treatment and analyses fell out of scope of this work, we adopted generic yet efficient off-the-shelf algorithms and implemented in-house software to perform these tasks. Firstly, multivariate mixture models (Yuekao Li et al., 2020), was applied to these CT images, to assign an individual voxel to abdominal tissue, vessel,

and background classes, with associated probabilities. Subsequently, to enhance the fidelity of multi-class labelling, relaxation labeling (RL) was performed to regularize the initial probabilities, based on contextual information (Rosenfeld et al., 1976). Graph cut (Boykov & Kolmogorov, 2004) algorithm was then used to extract the liver and enclosed vessels, based on their spatial relationship. The corresponding 3D surface meshes were finally reconstructed by the Marching Cubes (Lorensen & Cline, 1987) and later used as inputs to the subsequent steps in the proposed segmentation pipeline.

3. 2. 2 Tracing vascular centerlines

Referring parts of a liver to respective functional segments required not only its morphological cue but also accurate localization and measurement of enclosed vascular branches. To this end, skeletonization was a viable tool for consolidating voxelate data, while maintaining precise geometry and valid topology of the underlying network. Therefore, in this work, a method proposed by Antiga et al., (Antiga, 2002) was adopted. Once skeletonized, all but major branches were trimmed off, based on their regional radii. Subsequently, a user was asked to specify the starting and end points of the HV and PV. Generally, the former was located at the root, while the latter was at the first bifurcation point toward the end of a respective vein, as illustrated in **Figure 3.10**. It is worth noted that since their definitions were quite explicit, the criteria could be embedded in a computer program and hence having the markers specified automatically. That said, detailed implementation fell out of scope of this study but may be found elsewhere (Moccia et al., 2018; Zhang et al., 2017). Apart from this minimal intervention, the remaining of segmentation process was fully automatic.

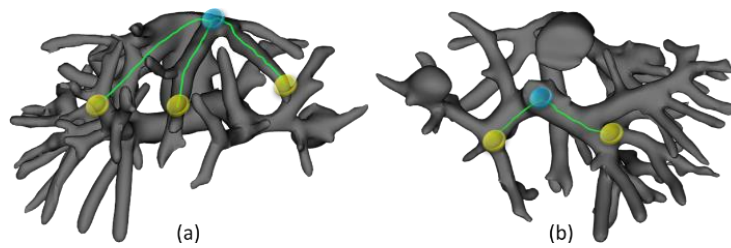


Figure 3.10 The extracted venous system with overlaid centerlines

(Seven manually specified starting (blue) and end (yellow) points on HV and PV are shown in an interior (a) and posterior views (b), respectively)

Given the extracted centerlines and respective markers on the primary venous system, their approximating vectors were next determined by principal component analysis (PCA) (Bartholomew, 2010) of all points within the corresponding vascular section.

3.2.3 Functional segmentation

Unlike existing methods, a main contribution of the proposed scheme is that, from this step onward, virtual resection was performed directly and automatically, by referring only to the specified interior vascular markers and differential geometries evaluated on the surface. This process was divided into five modules, whose details are explained as follow:

3.2.3.1 *Differential Geometry of the Features*

While other studies relied the separations of anterior from posterior segments and of left from right lobes on some approximating planes that were either inferred from distance functions and additional markers, or manually defined, the proposed method aimed at detecting discernible anatomical features, which were

gallbladder fossa and inferior ridge. Topologically, the gallbladder fossa appears as a narrow surface that spreads from the top of falciform ligament to the bottom of gallbladder area. The inferior ridge lies at the bottom of the liver, and extends from left to right lobe, passing under gallbladder fossa. Geometrically, the former may be characterized by the most concave partial surface on the posterior liver. Likewise, the latter corresponds to the most convex path along the inferior fringe. These features were identified accordingly by mean curvature expression, described as section 2.4.5.

The mean curvature is one of the most important intrinsic properties of a surface and is invariant to geometric transformation. It has been utilized in a range of applications, from computational science, medicine, and engineering (Horkaew & Yang, 2004; Magid, Soldea, & Rivlin, 2007; Zhao & Xu, 2006). In this study, it was evaluated on discrete triangular mesh of the extracted liver (Mesmoudi, De Floriani, & Magillo, 2012; Zhihong, Guo, Yanzhao, & Lee, 2011) and then employed as a determinant for anatomical feature classification.

Let $V = \{v_1, v_2, \dots, v_N | v_i \in \mathbb{R}^3, 0 \leq i \leq N\}$, be a set of N vertices constituting a whole liver surface, and $k(v_i)$ be the mean curvature at a vertex v_i . Assume further that the distribution of these curvatures over the surface is Gaussian, with mean and standard deviation (SD), μ_k and σ_k , respectively. Example of typical mean curvature distribution overlaid on a liver surface is shown in **Figure 3.11.a** and **Figure 3.11.b**.

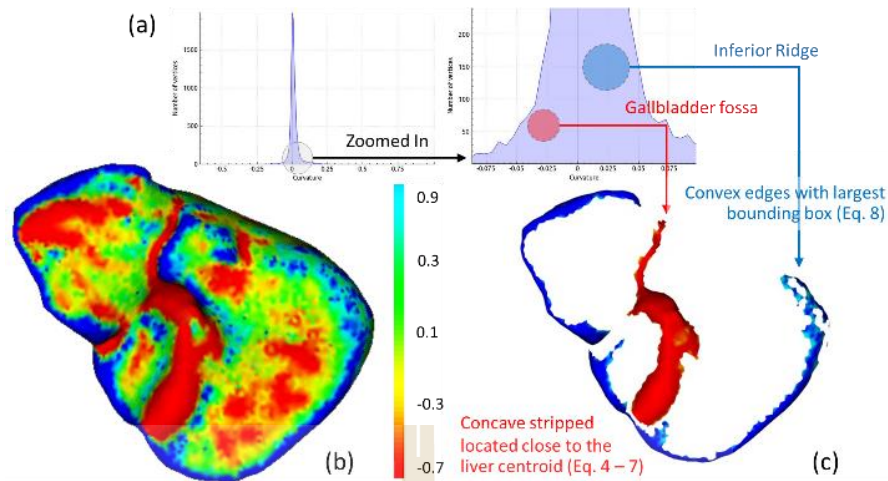


Figure 3.11 An example of mean curvature distribution

((a) on a liver surface (b), the corresponding extraction (c) of gallbladder fossa (red) and inferior ridge (blue) based on the thresholding and those based on anatomical criteria)

Firstly, to determine gallbladder fossa, let $V_c \subset V$, be a set of concave vertices, whose mean curvatures are lower than a threshold, given by a real positive constant a , and the Gaussian parameters, i.e.,

$$V_c(a) = \{v \in V \mid k(v) \leq \mu_k + a * \sigma_k\} \quad (3.23)$$

A concave set satisfying the above criterion (rendered in red) may consist of multiple connected regions (patches), each of which is denoted by v_j , i.e., $V_c(a) = \cup_j v_j$. As it appears in **Figure 3.11.b**, the gallbladder fossa is a narrow and highly concave strip, located approximately between left and right lobes. The

geometrical appearance of a j^{th} patch \mathbf{v}_j is characterized by a function of its normalized width and curvature, that is,

$$\mathcal{E}(\mathbf{v}_j) = \frac{1}{\|L_j\|} \cdot \frac{|V|}{|\mathbf{v}_j|} \sum_{v \in \mathbf{v}_j} d_{\perp}(v, L_j) \cdot e^{-\left(\frac{k(v)}{\sigma_k}\right)^2} \quad (3.24)$$

where L_j and $\|L_j\|$ are the principal axis passing through the centroid of \mathbf{v}_j , and its length, respectively. The norms, $|V|$ and $|\mathbf{v}_j|$ are the numbers of total vertices and those of the j^{th} connected patch, respectively. In addition, the distance function $d_{\perp}(p, L)$ is the shortest distance from a point p to a line L . The lower the \mathcal{E} value, the more likely the patch is of gallbladder fossa. To further ensure accurate identification of the structure, additional location constraint was imposed on its centroid being closest to that of the whole liver, that is,

$$d(\bar{\mathbf{v}}_j, \bar{\mathbf{V}}) = \|\bar{\mathbf{v}}_j - \bar{\mathbf{V}}\|_2 \quad (3.25)$$

where $\bar{\mathbf{v}}_j$ and $\bar{\mathbf{V}}$ are centroids of the respective surfaces and $d(\cdot, \cdot)$ is a Euclidean distance between two points.

For given a and hence $V_c(a)$ in Eq. (2.38), the surface patch, j^{th} that has both the lowest $\mathcal{E}(\mathbf{v}_j)$ and $d(\bar{\mathbf{v}}_j, \bar{\mathbf{V}})$ was chosen as a candidate. A grid search was run for $a \in [-0.5, 0]$. And once completed, the best candidate, whose costs were the lowest, was identified. Particularly, if $\mathbf{v}_j \in V_c(a_j)$ and $\mathbf{v}_i \in V_c(a_i)$ be the running candidates found at rounds j and i , with constants, a_j and a_i , respectively, then a patch \mathbf{v}_j would be identified as gallbladder fossa, denoted by \mathbf{v}_{gal} , only if, for $i \neq j$, they simultaneously satisfied the following conditions:

$$\mathcal{E}(\mathbf{v}_j) < \mathcal{E}(\mathbf{v}_i) \quad (3.26)$$

$$d(\bar{\mathbf{v}}_j, \bar{\mathbf{V}}) < d(\bar{\mathbf{v}}_i, \bar{\mathbf{V}}) \quad (3.27)$$

Secondly, the inferior ridge (rendered in blue), denoted by \mathbf{v}_{ird} , is simply defined as all connected regions, that are more convex than a specified threshold, given by a real positive constant b and the Gaussian parameters, i.e.,

$$\mathbf{V}_x(b) = \{v \in V \mid k(v) \geq \mu_k + b * \sigma_k\} \quad (3.28)$$

Unlike \mathbf{v}_{gal} that is defined as a singly connected region, \mathbf{v}_{ird} is all the regions, \mathbf{v}_k , that satisfy Eq. (8), that is, $\mathbf{V}_x = \cup_k \mathbf{v}_k$. However, similar to identifying gallbladder fossa, an optimal value of b and hence respective set $\mathbf{V}_x(b)$ were determined for $b \in [0, 0.5]$, by grid searching. In this case, the best candidate for the inferior ridge was that with the least number of vertices but the largest bounding box.

In preliminary trials, it was found that the optimal constants, a and b in Eq. (3) and (8), in a shape instance as shown in **Figure 3.11.c**, were -0.3 and $+0.3$ ($\sim 38.21\%$ at both ends), respectively. Likewise, the constants were computed automatically for the remaining of the dataset.

3.2.3.2 Locating Primary Functional Landmarks

Once the gallbladder fossa (\mathbf{v}_{gal}) and inferior ridge (\mathbf{v}_{ird}) were extracted from the liver surface, these cloud points were skeletonized by using global center technique (Guiqing Li et al., 2013). The resulted curves, i.e., \mathbf{C}_{gal} and \mathbf{C}_{ird} , respectively, consisted of ordered vertices, outlining the anatomical features, shown in **Figure 3.12.a**.

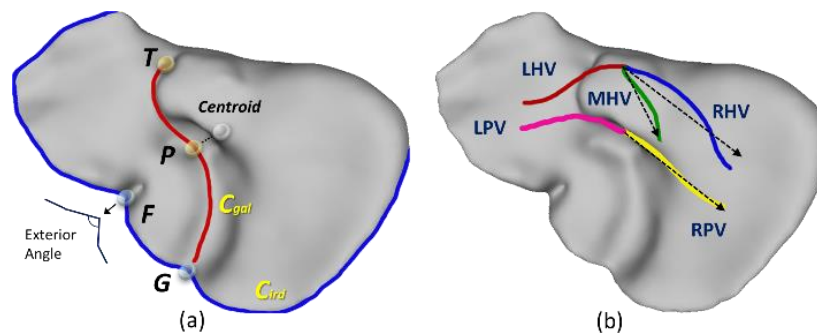


Figure 3.12 Location of landmarks

(Four functional landmarks on gallbladder fossa (T , P) and inferior ridge curves (G , F) (a), and three principal vectors, approximating MHV, RHV, and RPV (b))

A falciform ligament marker, denoted by a point T , was first placed at the tip of C_{gal} . Then, the entry point to the main PV, denoted by a point P , was placed on the same curve, but closest to the liver centroid. The latter, identified as hepatic hilum, featured as an inferior margin of the caudate segment. On the C_{ird} curve, a corner point G was placed closest to the bottom end of the C_{gal} . Finally, a point F was defined as the one that lied within a spherical neighbor of radius l_h to G and with minimal exterior angle. Anatomically, it was located on the same side as T and at the fissure on inferior surface between right and left lobes. The points T and F marked both ends of falciform ligaments that attaches the liver to the front body wall, and acts like a natural plane separating the left lobe into medial and lateral sections (Stehr & Gingalewski, 2012; V & BW, 2020).

3.2.3.3 Labeling Vessels and Extracting Vectors

Subsequently, the primary landmarks located in the previous module were used to label five major branches from the vascular network, extracted earlier. They were LHV, MHV, RHV, LPV and RPV. To this end, first let p_{HV}^S and p_{PV}^S be the starting points of hepatic and portal veins, respectively. In addition, let $d(\mathbf{P}, p_{HV}^S)$ and $d(\mathbf{P}, p_{PV}^S)$ be their Euclidean distances to the entry point of main portal vein, \mathbf{P} . Then, the HV and PV could be distinguished by their distances to this entry point, that is, $d(\mathbf{P}, p_{HV}^S) > d(\mathbf{P}, p_{PV}^S)$. Likewise, three and two branches of HV and PV could be labelled according to relative distances from their midpoints to the falciform ligament markers, \mathbf{T} and \mathbf{F} , following to Eq. (3.29) and (3.30), respectively.

$$d(\mathbf{T}, \bar{\mathbf{C}}_{LHV}) < d(\mathbf{T}, \bar{\mathbf{C}}_{MHV}) < d(\mathbf{T}, \bar{\mathbf{C}}_{RHV}) \quad (3.29)$$

$$d(\mathbf{F}, \bar{\mathbf{C}}_{LPV}) < d(\mathbf{F}, \bar{\mathbf{C}}_{MPV}) \quad (3.30)$$

where $\bar{\mathbf{C}}_V$ were the center points of a respective vein, V , i.e., LHV, MHV, RHV, LPV, and MPV.

Vascular geometries markedly differ across subjects but conformed to gross anatomy of the organ (Zhang et al., 2017). Therefore, to ensure adaptation to these variations, while maintaining gradual surface resection trajectory, and hence realistic preoperative simulation, these hepatic and portal branches were simplified by approximating vectors. Unfortunately, due to dissensions in the literature regarding characterization of the lateral segments, only MHV, RHV, and RPV were thus approximated, by using generic PCA, as illustrated in **Figure 3.12.b**. This statistical operation is useful in spanning orthogonal bases that best describes underlying data

points with respect to their spatial variances. That being said, unlike other resection methods, there was no cutting hyperplane reconstructed at this stage as yet, due to limited degrees of freedoms (DOF) of the vessels and their incurvate paths. Instead, in this work, these principal vectors, each of which approximated a major branch, were jointly considered with the previously labelled landmarks to better and more robustly determine the resection planes.

3.2.3.4 *Determining the Resections Planes*

One of the most crucial modules is determining the planes that separate the liver volumetry into functional segments according to Couinaud's classification. This module began with constructing three vertical planes, namely, Π_{MHV} , Π_{RHV} , and Π_{LHV} . These planes divided a liver into posterior, anterior, medial, and lateral sections. Unlike the other sections, the lateral one was a part of the left lobe and was separated by falciform ligament. Both LHV and falciform ligament were thus used to create the left ventricular plane (Π_{LHV}). Subsequently, the left and right horizontal planes, namely Π_{RPV} and Π_{LPV} , were used to separate the inferior from superior parts. Examples of these planes are illustrated in **Figure 3.13**.

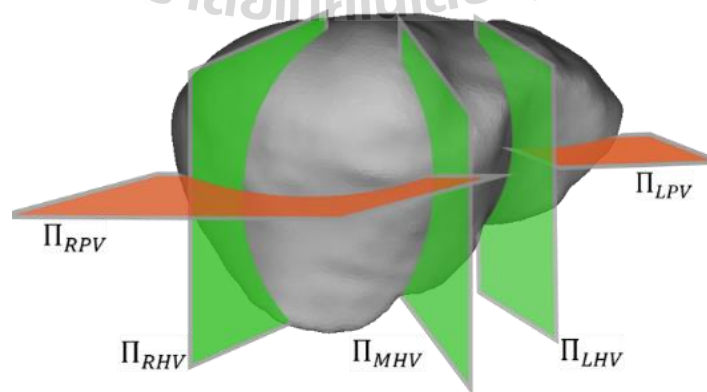


Figure 3.13 Three vertical and two horizontal planes

Assume that a resection plane is defined, either by orthogonal $\Pi^n(\vec{n}_{(\cdot)}, p)$ or tangent $\Pi^t(\vec{h}_{(\cdot)}, p)$ expressions. The former is a plane, defined by a normal vector \vec{n} and a point p , while the latter is that containing both tangential vector \vec{h} and point p .

Firstly, let \vec{h}_{MHV} , \vec{h}_{RHV} , and \vec{h}_{RPV} be the principal vectors, corresponding to MHV, RHV, and RPV, respectively. Let \vec{h}_{TF} be the vector pointing from point T toward F , along the falciform ligament. Accordingly, the vertical planes, defined by these veins are expressed in **Table 3.4**.

Table 3.4 Expressions of MHV, RHV, and RPV planes

Plane	Expression	Remark
MHV	$\Pi_{MHV}^t(\vec{h}_{MHV}, \mathbf{G})$	
RHV	$\Pi_{RHV}^t(\vec{h}_{RHV}, \mathbf{G})$	
RPV	$\Pi_{LHV}^t(\vec{h}_{TF}, \mathbf{q})$	Planar approximation of falciform ligament.

where \mathbf{q} is an arbitrary point on LHV, chosen so that the area of a 3D closed curve formed by intersection between Π_{LHV} and liver volume is minimized, as illustrated in

Figure 3.13.

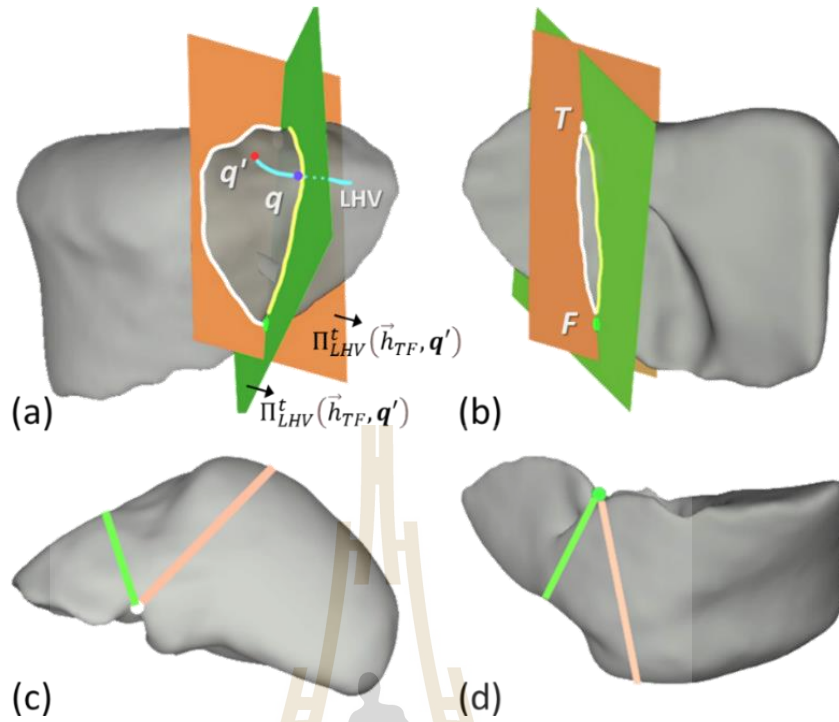


Figure 3.14 Illustrations of the left HV plane (Π_{LHV})

(On anterior (a), posterior (b), superior (c), and inferior (d) views. The intersection region between this plane (filled with green) and liver volume, given, for instance, a point \mathbf{q} is less than a point \mathbf{q}' , then the former was chosen)

Secondly, for the horizontal planes, let \vec{n}_{MHV} and \vec{n}_{RHV} be the normal vectors of MHV and RHV planes, respectively, \vec{n}_{RPV} be a normal vector perpendicular to a plane defined by \vec{h}_{RPV} and an average between let \vec{n}_{MHV} and \vec{n}_{RHV} , and also, \mathbf{r} be a point on \vec{h}_{RPV} . Accordingly, the RPV plane is expressed by $\Pi_{RPV}^n(\vec{n}_{RPV}, \mathbf{r})$. Finally, the LPV plane, Π_{LPV} , was defined such that it was initially perpendicular to Π_{LHV} and then rotated iteratively about \vec{n}_{LHV} axis, until it was also normal to a principal plane (Π_P), in which projections of points on the left branch of PV had greatest variance (well distributed). The planes, $\Pi_{LPV} \perp \Pi_{LHV} \perp \Pi_P$, are shown in **Fig. 8**.

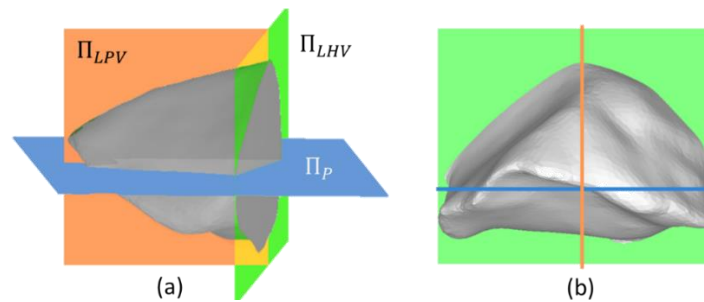


Figure 3.15 The left PV plane (Π_{LPV}) (orange)

(It lies on the lateral section and is perpendicular to both left HV plane (Π_{LHV}) (green) and the principal plane (Π_P) (blue) where left PV are well distributed)

Another contribution of this work is accurate labelling of caudate segment, separated from left and right lobes, by anatomical boundaries. Oxygenated and nutrient blood flow enters this segment via PV, before directly draining into IVC. Accurate localization of the segment plays a crucial role in diagnosing and surgical intervention of hepatic diseases (Kumon, 2017), particularly, Hepatocellular carcinoma (HCC) (Wahab et al., 2011).

Nonetheless, computer assisted extraction of caudate segment from nearby sections remained problematic, because of its morphological variants and ambiguous boundaries, especially on CT images. However, a radiologist could identify caudate segment by its general appearance, i.e., rectangle, piriform or irregular form (Sagoo, Aland, & Gosden, 2018). From posterior perspective, it is positioned behind the hepatic helium and in front of LPV. Its upper end is bounded by HV. To its left is ligamentum venosum, whereas its right margin is unclear (Brown, Filly, & Callen, 1982; Gang et al., 2009; Sagoo et al., 2018; Wahab et al., 2011). As a result, this structure had

so far been disregarded by most CAD studies. To reiterate the survey on this issue, Cheng et al. (Y. Chen et al., 2016) adopted Sell's NNSA technique (Selle et al., 2002) and labelled caudate voxels, while Boltcheva (Boltcheva et al., 2006) located this segment by extending MHV and RHV planes, and hence extrapolating their intersections with the liver. Lastly, Butdee et al. (Butdee et al., 2017) interpolated the structure by manually delineated Bézier curves. Implying caudate segment solely by geometrical elements, these techniques discarding its morphological contexts as well as surrounding vascular and other hepatic structures, and hence were not sufficiently accurate.

It was suggested in (Gang et al., 2009), that IVC can be considered as the right margin of caudate segment. Unfortunately, IVC is not always discernable on CT images nor on a liver surface. With the proposed method, IVC was hence approximated by a line. It was observed that IVC is almost parallel to falciform ligament, which is commonly characterized by concave region in the middle of the liver surface (C.2). Therefore, to simplify the IVC, it was defined by a segment AP , as shown in **Figure 3.16**.

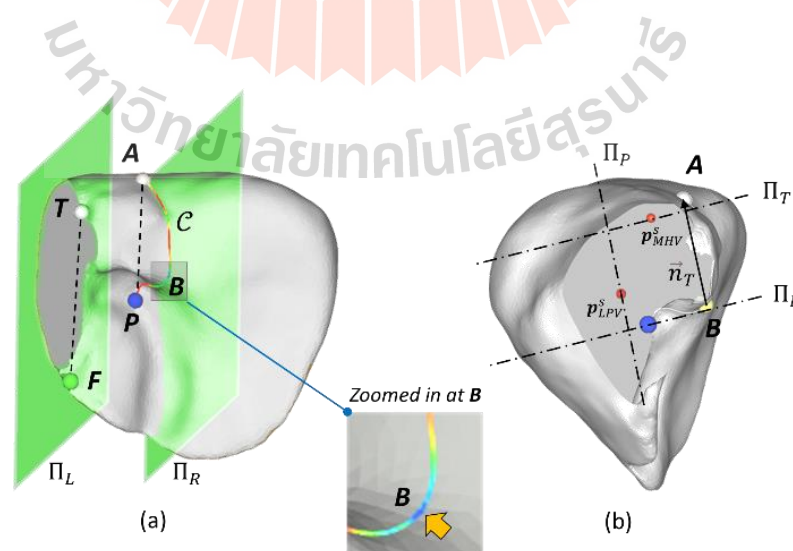


Figure 3.16 The bounding planes of the segment I

((a) depicts left and right planes, while (b) depicts and top, bottom, and posterior planes, respectively)

In this figure, \mathbf{P} was the entry point to the main portal vein (C.3), while \mathbf{A} is an intersection between the liver and a line passing \mathbf{P} and parallel to \vec{h}_{TF} (C.4). Then, the caudate segment is that bounded by the liver exterior and the following planes, as listed in **Table 3.5**.

To define the top plane, assuming \mathcal{C} be a curve segment that was formed by the intersection between the liver surface and bounded by points \mathbf{P} and \mathbf{A} . Then, \mathbf{B} was a point on this curve that had the highest curvature. The normal vector and point associated with the top plane was $\vec{n}_T = \mathbf{A} - \mathbf{B}$, and the starting point of MHV, \mathbf{p}_{MHV}^S , respectively. Similarly, the posterior plane was defined by an orthogonal vector $\vec{n}_P = \vec{n}_T \times \vec{n}_{LHV}$ and the starting point of LPV, \mathbf{p}_{LPV}^S .

Table 3.5 Expressions of the bounding planes and surface of the segment I

Plane	Expression	Remark
Left	$\Pi_L^t(\vec{h}_{MHV}, \mathbf{G})$	See section 3.2.3.4 for Π_{LHV}^t
Right	$\Pi_R^n(\vec{n}_{LHV}, \mathbf{P})$	
Top	$\Pi_T^n(\vec{n}_T, \mathbf{p}_{MHV}^S)$	See text and Figure 3.16 for \vec{n}_T .
Bottom	$\Pi_B^n(\vec{n}_T, \mathbf{P})$	
Posterior	$\Pi_P^n(\vec{n}_P, \mathbf{p}_{LPV}^S)$	See text and Figure 3.16 for \vec{n}_P .
Anterior	Liver surface	Exterior surface of the liver

Finally, provided these planes were defined as such, resections of all eight functional segments as per Couinaud's scheme could be performed virtually by tracing along their intersecting curves with the extracted liver surface.

3.3 Parameterization of a Liver Surface

The spherical conformal parameterization has been widely used in analysis of brain surface, face expression. Given two genus-0 surfaces $S_{1,2}$, and their corresponding landmarks, $P = (p_1, p_2, \dots, p_n)$, $Q = (q_1, q_2, \dots, q_n)$, the registration between landmarks can be obtained by landmark aligned SCM techniques, e.g., FLASH (P. T. Choi et al., 2015). Based on this idea, this study proposed a technique by combination of the aligned mapping and rigid body transformation for estimating the GV in LDLT surgery. Firstly, a set of landmarks are defined on both recipient liver (referred as recipient or S_1) and donor liver (referred as donor or S_2). Then the landmark matching spherical map is obtained using FLASH algorithm.

Assume S'_1 be the symmetric corresponding of S_1 to S_2 . It means that S'_1 has the same topology to S_1 but geometry to S_2 ; R_1 denotes the segment to be resected in S_1 . It is noted that both R_1 and R_2 may include points on liver surface (called by v_{1u}, v_{2u}) and interior points (called by v_{1i}, v_{2i}) which define the boundary of each segment. Moreover, each point in set v_{2u} could be computed by its corresponding v_{1u} . The goal is to estimate the GV R_2 on S'_1 . To do so, the surface points of R_1 (v_{1u}) is firstly aligned to the ones of $R_2(v_{1u})$ by using rigid body transform with iso-scaling. In details, we are looking for a transformation,

$$T: v_{2u} \approx \mathbf{s}\mathcal{R}(v_{1u}) + \mathbf{t} \quad (3.31)$$

where \mathbf{s} , \mathcal{R} and \mathbf{t} are the scale coefficient, rotation matrix and translation offset. This least square problem has been efficiently solved using closed-form solution which reported in (Horn, 1987). Assume $v_1 = \{v_{1u}, v_{1i}\}$ and v_1^* stands for the registration of v_1 to v_{2u} , then,

$$v_1^* = \mathbf{s}\mathcal{R}(v_1) + \mathbf{t} \quad (3.32)$$

Thin Plate Spline (TPS)(Bookstein, 1989) has been known as a smooth surface interpolation pass through controls points is applied to minor adjust v_1^* . Given a set of control points $p_{1 \leq i \leq n}$, the surface point is defined as follow:

$$f(x, y, z) = a_0 + a_1x + a_2y + a_3z + \sum_{i=1}^n w_i U(\|(x, y, z) - p_i\|) \quad (3.33)$$

Where a_k is coefficients, w_i is weight of control point; $U(\|\chi\|) = \chi^2 \log(\chi)$.

To reconstruct interior point of $R_2 (v_{2i})$, the control points are uniformly selected from surface points in v_1^* and v_{2u} . Finally, each point in v_{2i} is obtained by applying TPS transformation of each point in v_{1i}^* .

The process of rigid and TPS transformation are illustrated in **Figure 3.17**.

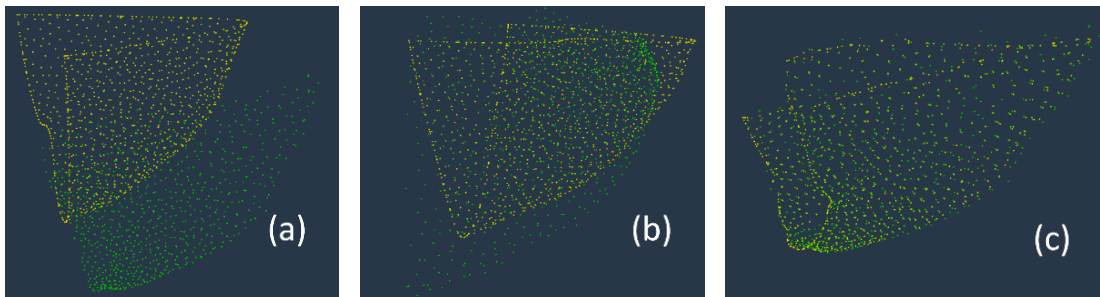


Figure 3.17 The rigid and TPS of surface points

(On segment's recipient (yellow) and estimated GV (green). The original points (a) from source surface are registered on target by rigid body and uniform scaling (b) and TPS (c))

In summary, the process of graft estimation is as following: The surgeon selects a segment to be resected on recipient, then initialize a few surface landmarks in this segment. For a donor's, liver, a few landmarks which is corresponding to the ones in recipient are located. The SCM based on these landmarks is executed before similarity transformation is used. Finally, TPS is applied to reconstruct the estimated graft.

CHAPTER 4

EXPERIMENTS AND RESULTS

This chapter briefly presents the dataset which are used for evaluating the proposed methods, Medical Image Computing and Computer-Assisted Intervention (MICCAI) 2007. Five metrics and score are applied to quantitatively compare among relevant methods (section 4. 1). Section 4. 2 evaluates the accuracy of segmentation method, section 4. 3 is to evaluate the functional segmentation of liver according Couinaud's scheme. Section 4. 4 and 4. 5 present liver parameterization and application of liver simulation in surgical plaining.



4.1 Dataset and evaluation metrics

The evaluation of performance between different methods is difficult since most algorithms are usually not available and re-implementing is time consuming. Additionally, several authors used different evaluation methods on various datasets which are often local. The using of a publicly dataset and specified evaluation metrics enable a fair comparison between different technique from different researchers. Over recent year, the MICCAI (T. Heimann et al., 2009) dataset has been widely used to evaluate among different segmentation technique. For quantitative evaluations, segmented liver volumes were compared against corresponding references, based on 5 evaluation metrics (T. Heimann et al., 2009). They were Volumetric Overlap Error (VOE), Relative Volume Difference (RVD), Average Symmetric Surface Distance (ASD), Root Mean Square Symmetric Surface Distance (RMSD), and Maximum Symmetric Surface Distance (MSD). The score for each metric was computed based on error rate (e) and average user error (\bar{e}), whose references were provided by (T. Heimann et al., 2009), over all instances. The higher these scores, the better the performance.

The proposed technique was developed by using C and C++ languages and implemented on Linux operating system. It ran on a personal computer equipped with a 2.4 GHz CPU and an 8 GB RAM. Basic image processing and graphics algorithms involved were derived from OpenCV (**OpenCV library**, 2020) and Visualization Toolkit (VTK) (**Visualization Toolkit**, 2020) and Vascular Modeling Toolkit (VMTK) (**VMTK**, 2020). The first library implemented general and advantaged algorithms which used in computer vision applications. The second library has been widely used in many medical imaging studies, thanks to its ability to parse standard DICOM image and its meta data. It also allows intuitive graphical manipulations of a 3D object, e.g.,

geometrical operations, material processing, representing a model in points, wireframes, or surfaces forms, slicing, and clipping, etc. The third library was typically used to perform 3D vascular segmentation, centerline detection, mesh generation, and geometrical analyses. In order to visually assess the segmentation results, a surface model of segmented liver was reconstructed by using the Marching Cubes (MC), implemented in VTK. The workflow of experiments is illustrated as **Figure 4.1**.

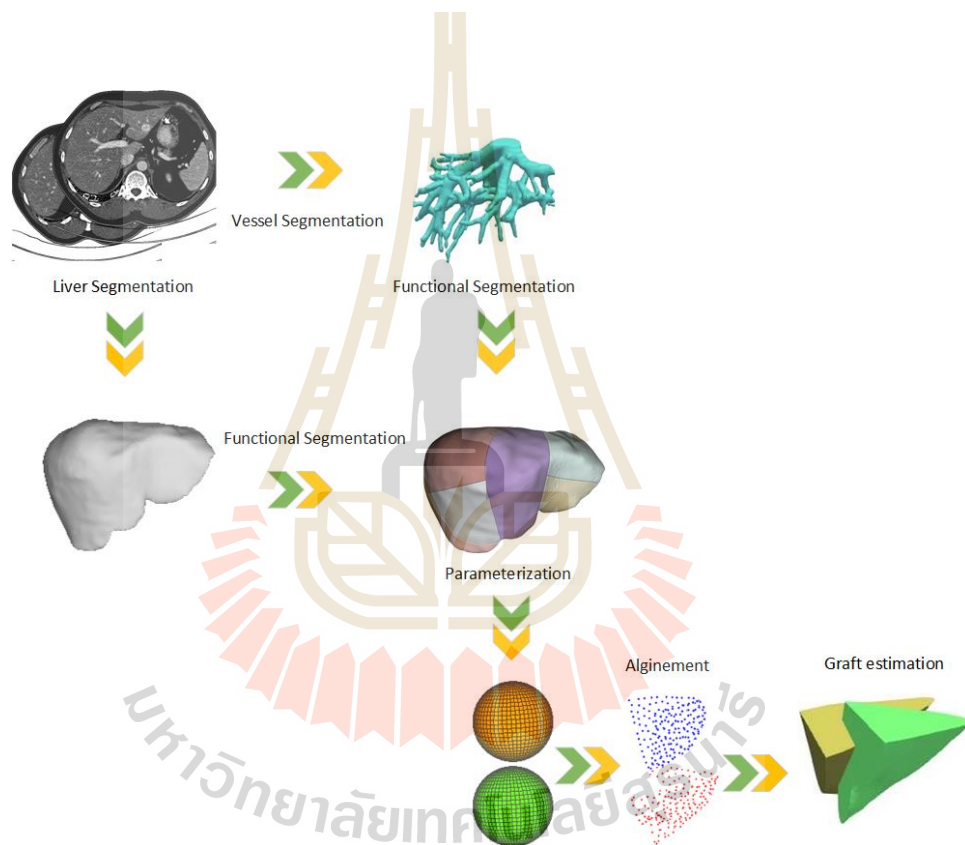


Figure 4.1 The workflow of experiments.

4. 1. 1 MICCAI dataset

MICCAI 2007 dataset was set forth by (T. Heimann et al., 2009) at Medical Image Computing and Computer-Assisted Intervention (MICCAI) conference, in Brisbane, Australia. This dataset has been widely used by several research during a

decade. It contains 30 contrast-enhanced CT volumes captured by a variety of different CT scanners come from different manufacturers. The dataset consisted of 30 CT volumes. Out of these, 20 volumes were training scans, whose ground-truth (labelled reference) was provided. The remaining 10 volumes, referred here as testing scans, were unlabeled. To evaluate the results on the latter, the authors were required to submit segmented livers to MICCAI SLIVER07 website. All images were recorded at a resolution of 512×512 pixels. The pixel sizes ranged from 0.55mm to 0.8mm, while distances between slices ranged from 1.0mm to 3.0mm. The number of slices in each volumetric scan varied between 64 to 502 (T. Heimann et al., 2009). Each CT image in MICCAI is presented by one metadata file associated to a raw data file.

4. 1. 2 Evaluation metrics

Segmentation results from proposed approaches are normally compared to expert-generated references based on two kinds of measurements, including volumetric overlap error and distance error. Depending on each application which the segmentation results is designed for, the user may prefer for a metric over other. There are five metrics which extended from these categories were used for evaluation. Each of metric is used to measure an aspect of the segmentation quality. It is noted that each CT image was independently evaluated on these metrics. It means that the assignment of each image was not affected by the number of slices or resolution. In MICCAI dataset, the number of slices varies from 64 to 502. This number may increase up to 1000 in modern scanner. The using of higher number of slices gives more details of liver surface. The missing slice if any in a CT volume will be ignored during segmentation progress. It may be filled by using interpolation between two adjacency slices or smoothing after reconstructed by Marching Cube if necessary. Let R and G be sets of voxels in

segmentation and reference; $\mathcal{S}(R)$ and $\mathcal{S}(G)$ be sets of voxels on surface of R and G , respectively. Each metric is given by follows (T. Heimann et al., 2009).

Volumetric overlap error (VOE)[%]

$$VOE(R, G) = 100 \left(1 - \frac{|R \cap G|}{|R \cup G|} \right) \quad (4.1)$$

Volumetric overlap error is the most popular metric used to evaluate the accuracy of segmentation methods. It measures the error rate between the intersection and union of two volumes in percent. The higher of volumetric overlap error, the lower of accuracy of a method. The VOE of 0 is for perfect segmentation technique, and 100 for failed segmentation.

Relative volume difference (RVD)[%]

$$RVD(R, G) = 100 \left(\frac{|R| - |G|}{|G|} \right) \quad (4.2)$$

This is a signed distance function and asymmetric. It is used to measure the over-under segmentation in percent. However, it should not be used as the only measure of the accuracy of segmentation method. This is because even though the relative volume difference equals 0, it does not imply that two volumes are identical. In liver surgical planning, the volume of graft is crucial to avoid post-operative risks such as liver insufficiency. Therefore, the using of this measurement in combination with other measurements will provide useful information for such an application.

Average symmetric surface distance (ASD)[mm]

$$ASD(R, G) = \frac{1}{|S(R)| + |S(G)|} \left(\sum_{s_R \in S(R)} d(s_R, S(G)) + \sum_{s_G \in S(G)} d(s_G, S(R)) \right) \quad (4.3)$$

where $d = (x, A) = \min_{s_A \in A} \|x - s_A\|$ is the shortest distance from an arbitrary voxel x to

surface A ; $\| \cdot \|$ denotes the Euclidean distance.

Average symmetric surface distance measures average distance between each voxel on surface of R to each voxel on surface of G in millimeters. Each voxel calculated must have at least one non-object voxel within their 18- neighbors. Unlike relative volume different, this measurement is a metric. The value of 0 means two surfaces are overlap each other. Although VOE metric is normally used in evaluation, it is rarely 0 in practice. Therefore, the combination of VOE which measures the identification and ASD which measure error distance are normally used to evaluate segmentation results.

Root mean square symmetric surface distance (RMSD) [mm]

$$RMSD(R, G) = \frac{1}{\sqrt{|S(R)| + |S(G)|}} \sqrt{\sum_{s_R \in S(R)} d^2(s_R, S(G)) + \sum_{s_G \in S(G)} d^2(s_G, S(R))} \quad (4.4)$$

This metric is also used to compute the distance between two surfaces in millimeters. It is an average of the root mean square of Euclidean distance, instead just Euclidean distance. The value of 0 implies a perfect segmentation. RMSD is a symmetric measurement, and it can be used to measure the accuracy. It also reflects the deviation in error distance rather than average error.

Maximum symmetric surface distance (MSD)[mm]

$$MSD(R, G) = \max \left(\max_{s_R} d(s_R, S(G)), \max_{s_G} d(s_G, S(R)) \right) \quad (4.5)$$

This measurement determines the maximum distance of maximum value from the Euclidean distance between two surfaces in millimeters. It is also known as Hausdorff distance. A perfect segmentation method yields the value of 0 of this metrics. MSD returns maximum distance error between volumes, it emphasizes the worst error rather than average error, which is important in surgical planning. Because MSD is sensitive to outline elements, so a segmentation algorithm with high value of MSD does not really imply the low accuracy. Moreover, a segmentation result with low ASD in overall but high RMSD at small area implies high MSD.

Score

To have an overall evaluation, the score for each metric is calculated based the average user error and error by

$$Score = \max \left(100 - 25 \frac{e}{\bar{e}}, 0 \right) \quad (4.6)$$

where e and \bar{e} are the error of each metric and average user error. The average user error for each metric is given in **Table 4.1**.

Table 4.1 Average user errors

Metric	VOE [%]	RVD [%]	ASD [mm]	RMSSD [mm]	MSD [mm]
Average user error	6.4 ± 1.0	4.7 ± 1.8	1.0 ± 0.2	1.8 ± 0.5	19.3 ± 5.6

4.2 Liver segmentation results

In the first experiment, 18 asymptomatic livers from 20 labelled instances were segmented. Their VOE, RVD, ASD, RMSSD, MSD, and respective and overall scores are reported in **Table 4.2** (except for the severe cases, i.e., 10 and 16). The average overall score for these instances is 72.3 ± 6.09 . Six images (35%) had the scores higher than the average of the Grand Challenge submissions. Note the robustness against noisy data, as shown by a high score of 81.5 in image 05. Nonetheless, without appearance prior model, image 09 exhibited a relative low score, due to mostly obscure separation against other organs.

Table 4.2 The evaluation metrics obtained from 18 (labelled) cases.

CT	VOE		RVD		ASD		RMSSD		MSD		Score
	%	Score	%	Score	mm	Score	mm	Score	mm	Score	
01	10.9	57.4	0.9	95.1	1.9	52.5	3.6	50.5	30.6	60.4	63.2
02	7.9	69.3	1.3	93.0	1.3	66.7	3.0	57.9	32.9	57.3	68.8
03	6.7	73.8	-0.4	97.6	1.0	75.8	2.2	69.9	19.2	75.1	78.5
04	6.8	73.6	-0.7	96.3	0.9	76.8	1.5	78.6	14.4	81.4	81.3
05	6.3	75.6	-0.4	97.9	0.8	79.5	1.6	77.8	17.8	76.9	81.5
06	8.2	68.0	0.3	98.5	1.3	67.9	2.9	60.2	24.6	68.1	72.5
07	8.9	65.1	-1.1	94.2	1.6	61.2	2.9	59.2	23.4	69.7	69.9
08	9.4	63.4	2.8	85.0	1.7	56.8	3.1	56.7	29.2	62.2	64.8
09	9.6	62.3	-3.3	82.5	1.7	56.6	3.5	51.0	29.7	61.5	62.8
11	7.3	71.6	0.1	99.3	1.4	65.8	3.1	56.4	24.1	68.8	72.4
12	6.8	73.4	1.7	91.1	1.0	74.5	2.0	72.6	23.4	69.6	76.2
13	10.5	58.8	6.9	63.5	1.6	60.9	2.4	66.9	18.2	76.5	65.3
14	7.4	70.9	2.6	86.0	1.2	69.1	3.2	54.9	31.9	58.6	67.9
15	5.6	78.0	2.2	88.0	0.8	80.6	1.6	77.1	17.3	77.6	80.3

CT	VOE		RVD		ASD		RMSSD		MSD		Score
	%	Score	%	Score	mm	Score	mm	Score	mm	Score	
17	7.8	69.6	2.0	89.6	1.2	68.9	2.8	60.8	23	70.2	71.8
18	8.2	68.1	2.9	84.8	1.3	68.4	2.1	71.5	20.2	73.8	73.3
19	6.4	74.9	1.8	90.7	1.1	72.2	2.7	63.1	38.2	50.5	70.3
20	6.2	75.7	1.1	93.9	0.9	78.2	1.7	75.9	17.5	77.3	80.2
Avg	7.8	69.4	1.2	90.4	1.3	68.5	2.6	64.5	24.2	68.6	72.3
Std	1.5		2.1		0.3		0.7		6.6		6.09

Figure 4.2 shows Box-Whiskers plots of these metrics and overall scores. Among these metrics, RVD was consistently the highest, followed by VOE and ASD, respectively.

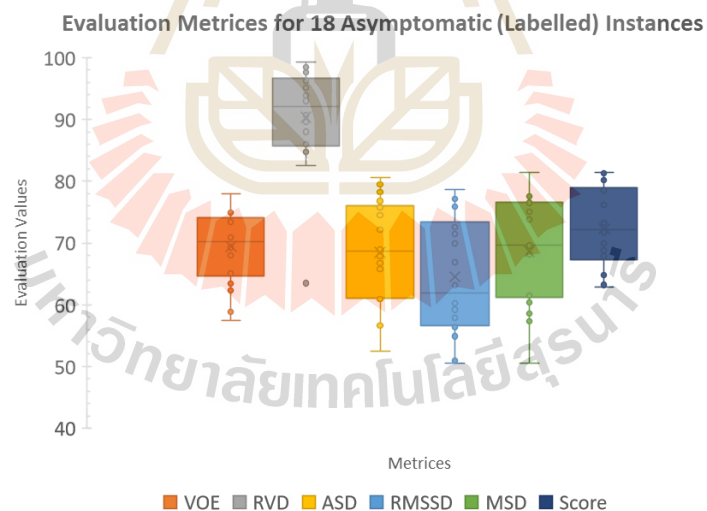


Figure 4.2 Box-Whiskers plots of metrics, and over scores

Figure 4.3 illustrates two cases, whose total scores were highest (05) and lowest (09), respectively, and their locations, where over and under segmentation occurred.

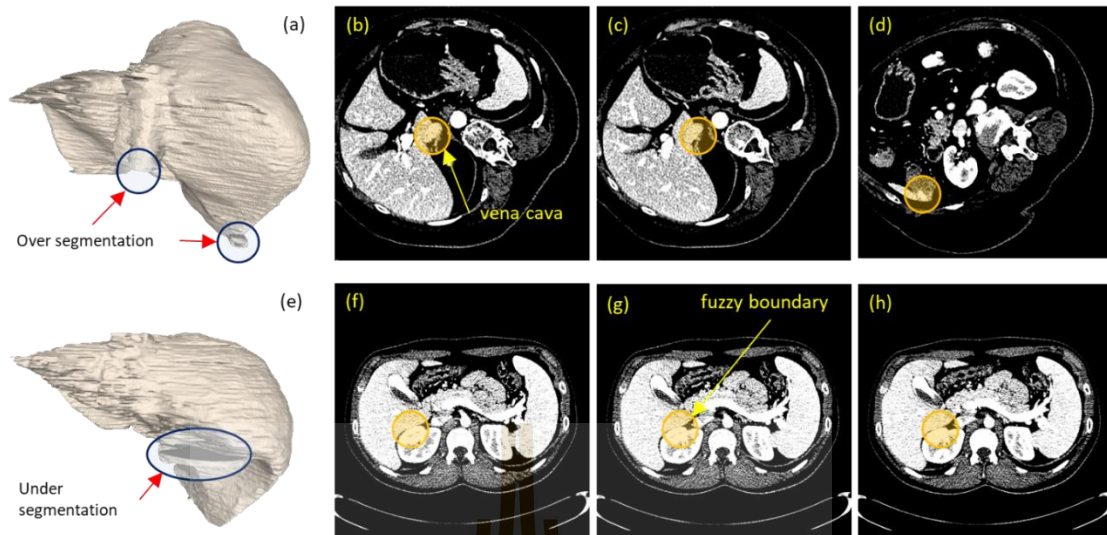


Figure 4.3 Examples of 3D segmentations

(Case 05 (top row) and 09 (bottom row), whose scores were the highest and the lowest, respectively. The corresponding images on their right shows CT slices where over (b), (c), and (d) and under (f), (g), and (h) segmentation occurred)

Figure 4.4 illustrates 2 examples of segmented healthy livers (one row for each case) by the proposed method, compared with the respective ground truths. Each column depicts an original image, segmented liver, ground-truth, and respective surface, rendered with false colors, representing errors (in mm).

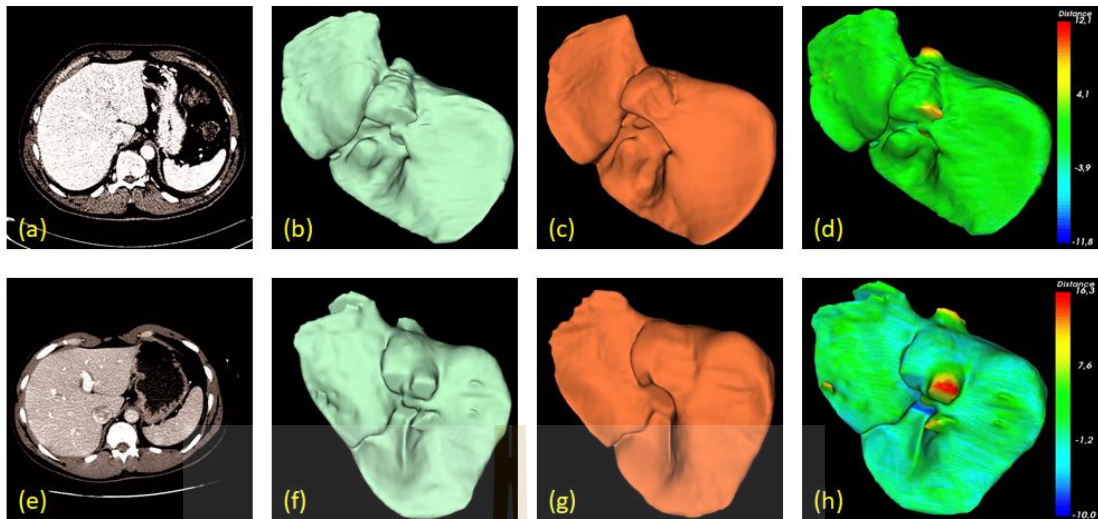


Figure 4.4 Selected examples of two healthy livers

(The first column (a, e) shows an original image. The second (b, f) and third (c, g) columns show the segmented results and respective ground truths. The last column (d, e) shows the error distance (in mm) between the segmented results and reference livers. The green color on the surface corresponds to the low error rate, while red and blue colors correspond to the high positive and negative ones, respectively)

Except seed points, initialized by the user, the remaining process was fully automatic. However, there were two empirical parameters involved in the process, i.e., the weighting factor in graph-cut and the threshold angle for bottleneck condition. As a guideline on how to determine the appropriate values, the experiments were run on available dataset. The weight and threshold were varied between $0.1 - 0.9$ and $120^\circ - 170^\circ$, respectively. **Figure 4.5** plots the overall scores versus weights (a) and thresholds (b), respectively.

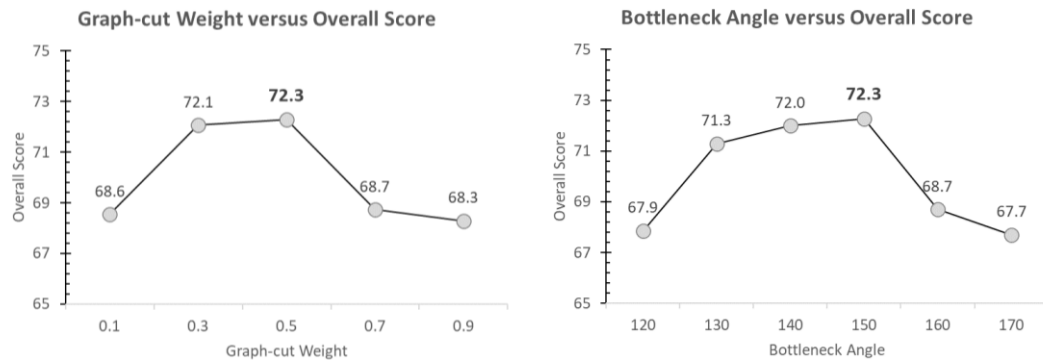


Figure 4.5 Graph-cuts weight/ bottleneck angle and score

Referred to these, the combination that yielded the highest overall score was chosen. As such, for the results reported herein, we set these numbers to 0.50 and 150°, respectively. Since these were the only empirical setups required, to assess the score variability due to these settings, **Figure 4.6** plots overall scores, when varying GC weights, with fixed exterior angles (a) and vice versa (b). It is evident that within optimal range, adjusting either of these parameters did not much affect the average scores, but slightly their deviations, in practice.

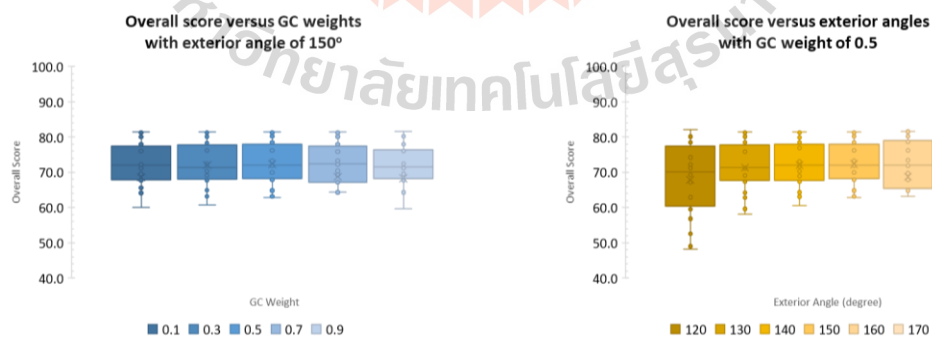


Figure 4.6 Graph-cuts weight / or exterior angle and score

- a.** Score variability with respect to GC weights, between 0.1 – 0.9. **b. Score** variability with respect to Exterior angle, between 120 – 170 degrees.

Visual and numerical assessments revealed one major pitfall of the method in this work. Except errors, caused by ambiguous boundary between liver and other abdominal structures, which could only be elevated by means of statistically trained or deeply learnt models, the major cause of lower accuracies (compared to (X. Chen et al., 2012), (Liao et al., 2016)) was due to inferior vena cava (IVC). It was cylindrical and appeared oval in a cross-sectional image that connects to the main branches of hepatic vein. But it was not considered as a part of the liver, hence excluded from the ground references. Nonetheless, it is anticipated that including IVC in surface reconstruction did not make a low-quality 3D model, especially in pre-operative planning. If it were, however, really necessary to remove this structure, a contrast agent enhancing blood passage, could be administered. Alternatively, a model-based approach, targeting a tubal structure, could be employed. To confirm the hypothesis, we manually removed portions of this IVC in one dataset and found that the errors significantly decreased. To this end, a user could choose few slices above and below the liver, where vena cava is found. Excluding these slices would effectively disconnect it from the liver. Besides, adding this step would not cause much burden to the user, in addition to specifying a seed point. That being said, it would increase observer variability, and hence was not included in the above analyses. **Figure 4.7** and **Table 4.3** illustrate the segmented liver before and after partial removal of IVC at bottom.

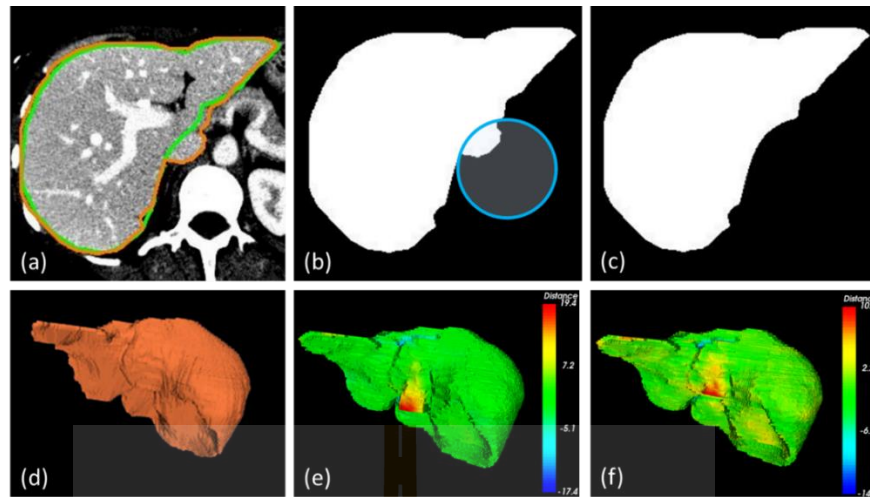


Figure 4.7 An example of manually remove IVC

(In the original image (a), the green and orange contours show the segmented and ground-truth. In the binary image (b), the IVC detected as bottleneck and removed(c). In comparing to the ground-truth (d), the segmented liver after removing IVC has the error distance from $[-14.7, 10.6]$, which is lower than the one before removing IVC $[-17.4, 19.4]$)

Table 4.3 The errors before and after removing IVC on the above case.

Metric	VOE[%]	RVD[%]	ASD[mm]	RMSD[mm]	MSD[mm]
Before	6.9	3.2	0.9	1.8	19.4
After	6.4	2.7	0.8	1.4	14.7

Alternatively, the liver and entire hepatic vasculature could be independently segmented. To this end, parts of the proposed method could be exploited. Particularly, MND, and RL, without GC or related constraints, were simultaneously applied to

extract interior vessels, which were subtracted from and later fused with the liver. The extracted result is illustrated in **Figure 4.8**. This vessel segmentation process took about additional 1.2 minutes.

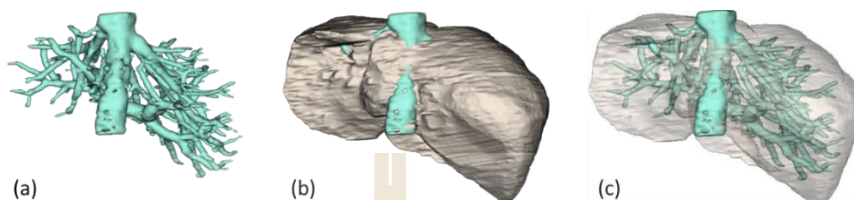


Figure 4.8 Segmentation of vessel and liver

In the second experiment on liver segmentation, the improved method is evaluated on 20 CT images of MICCAI dataset. The distribution of VOE, RVD, ASD, RMSD, MSD metrics, and the overall score for all 20 segmented livers are plotted in Figure 4.9. The average overall score was 75.69 ± 5.388 . The lowest and highest scores were 65.3 and 83.1, respectively. Out of 20 instances, 11 instances gave scores higher than the average.

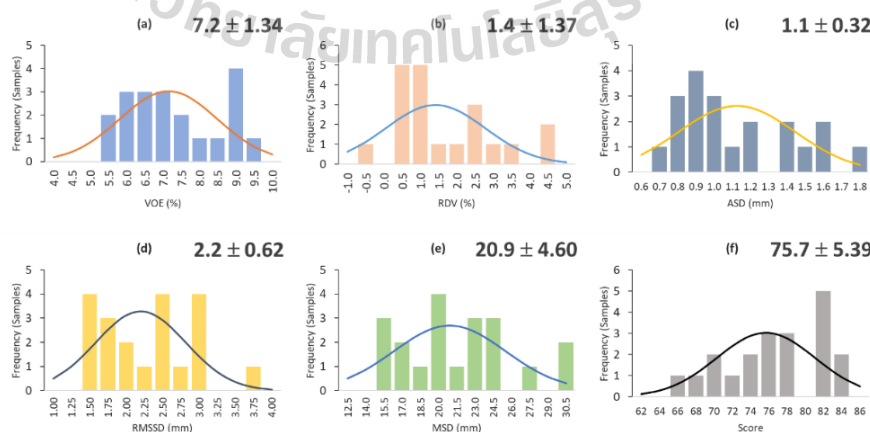


Figure 4.9 Sample distribution of metrics

(VOE (a), RVD (b), ASD (c), RMSD (d), MSD (e) metrics, and overall score (f) for all 20 segmented livers from MICCAI)

Subsequently, the evaluation metrics, obtained by the proposed method, for 20 MICCAI images, as well as their processing times, were also compared against those obtained by state-of-the-art methods. The comparisons are listed in Table 2.

Table 4.4 Benchmarking on metrics and processing time

Metrics	VOE	RVD	ASD	RMSD	MSD	Time	CPU
Peng et al	4.5 ± 1.0	0.15 ± 0.9	0.8 ± 0.2	1.5 ± 0.3	16.8 ± 2.9	2-3	i5, RAM 8GB
Liao et al	5.8 ± 3.2	-0.1 ± 4.1	1.0 ± 0.5	2.0 ± 1.2	21.2 ± 9.3	4.7	i7 2.4GH, Nvidia GeForce 16GB RAM
Chen et al	6.5 ± 1.8	-2.1 ± 2.3	1.0 ± 0.4	1.8 ± 1.0	20.5 ± 9.3	6.0	Xeon workstation 2.8 RAM 8GB
Lu et al	7.4 ± 1.9	4.6 ± 2.8	1.2 ± 0.4	2.8 ± 1.3	38.5 ± 18	12.4	i7 2.4GH, Nvidia GeForce 16GB RAM
Wu et al	$7.5 \pm *$	$4.2 \pm *$	$1.0 \pm *$	$1.9 \pm *$	$18.5 \pm *$	0.4	2.4GH, 4GB
Zheng et al	$7.8 \pm *$	$5.1 \pm *$	$1.1 \pm *$	$1.4 \pm *$	$11.1 \pm *$	**	-
Yang et al	8.9 ± 2.2	2.3 ± 2.0	1.4 ± 0.3	2.4 ± 1.2	24.3 ± 9.6	2.1	i7 2.4GH, Nvidia GeForce 16GB RAM
Selver et al	11.9 ± 4.5	-3.4 ± 5.2	1.7 ± 0.6	3.6 ± 1.8	49.3 ± 27.1	7.9	i7 2.4GH, Nvidia GeForce 16GB RAM
Model 1	7.8 ± 1.5	1.2 ± 2.1	1.3 ± 0.3	2.6 ± 0.7	24.2 ± 6.6	1.3	i7 2.4 GH, 16GB RAM
Model 2	7.2 ± 1.3	1.4 ± 1.4	1.1 ± 0.3	2.2 ± 0.6	20.9 ± 4.6	1.4	i7 2.4 GH, 16GB RAM

Note: Fields denoted with

* are those not reported in the corresponding works.

** the author concluded that their method takes a long time for image analysis, but they did not report the number.

It is evident that Peng's and Liao's method outperformed the rest and ranked first on VOE, RVD and ASD. Their techniques took 2-3 min and 4.7 min to segment a liver on average. Meanwhile, Zheng's work performed best on RMSD and MSD, but worst on RVD and VOE and take a long time for processing. These findings suggested that the former performed well on volume overlapping, while the latter did so on point-to-surface distance. Regarding VOE, our method is ranked 4th/9 after Peng, Liao and Chen, however, our method did not require interaction, pre-processing, nor multiple landmarks being specified by a user and training model like Chen. In addition, another key advantage of the proposed method was the lowest standard deviation except Peng's, which implies the most consistent performance. Its average score was also higher than the reported user (manual) score. This indicates that the proposed method was highly reproducible and could be applied in clinical practice. In some cases, the executing time is important to measure efficiency among algorithms if they were run upon the same system computer configuration. However, the re-implementation of algorithms is time consuming and difficult. Therefore, the processing time listed in the table were for reference purpose because the proposed algorithms have been implemented on difference computers.

As mentioned in (T. Heimann et al., 2009), there are number of factors affect to the accuracy of segmentation technique. The user interactive based method reaches to high performance, but it depends on the experiences and skill of users. The model-based method invokes to training set which is not always available in practice. Regarding mechanic, Despite several attempts to accelerate the process by automatic seed-point selection (S. S. Kumar et al., 2011), if an underlying CT image includes multiple regions, its localization may be less accurate or even lie completely in non-liver areas (e.g., tumor, or dark object). It was, therefore, pointed out in (T. Heimann et al., 2009)

that interactive methods and those based on a statistical deformable model outperform their automatic counterparts, especially those without a prior model. Nonetheless, due to the particularly diverse morphology of a liver, a universal model would require a prohibitively large collection of training samples. On the other hand, with a limited number of known liver samples, higher interaction would be required on the user's part. Depending on the specific purpose and expected degree of confidence, care must be observed when balancing these requirements and devising a liver segmentation scheme.

Segmentations on unlabeled (testing) dataset were also submitted to MICCAI website, for online evaluation. The resultant metrics and corresponding overall scores for 7 of 10 asymptomatic livers are presented in **Table 4.5**. Particularly, VOE, RVD, ASD, RMSD, MSD metrics were 8.0 ± 1.1 , -0.3 ± 2.7 , 1.3 ± 0.4 , 2.5 ± 1.0 , and 24.9 ± 10.0 . These are hence converted to corresponding scores of 68.8, 88.3, 68.0, 64.5, and 67.1, respectively. Accordingly, the mean overall score was 71.3 ± 7.95 . It is also noticed that, while the metrics varied across images, they were particularly low for case 08.

Table 4.5 The evaluation metrics and score obtained from 7 asymptomatic

CT	VOE		RVD		ASD		RMSD		MSD	
	[%]	Score	[%]	Score	[mm]	Score	[mm]	Score	[mm]	Score
01	7.4	71.1	2.4	87.1	1.1	71.9	2.0	71.9	19.7	74.0
02	8.4	67.2	-2.1	88.4	1.2	71.2	2.2	69.2	21.2	72.1
05	9.6	62.6	0.9	95.3	1.5	60.3	2.7	61.6	24.2	68.0
06	8.6	66.4	3.0	83.8	1.3	66.7	2.2	69.2	20.7	72.7
07	6.6	74.1	0.3	98.2	0.9	76.6	1.8	73.6	23.3	69.2
08	8.6	66.5	-4.5	75.9	1.9	52.1	4.7	33.5	47.2	37.9

CT	VOE		RVD		ASD		RMSD		MSD	
	[%]	Score	[%]	Score	[mm]	Score	[mm]	Score	[mm]	Score
09	6.8	73.3	-2.0	89.3	0.9	76.9	1.9	72.8	18.2	76.0
Avg	8.0	68.8	-0.3	88.3	1.3	68.0	2.5	64.5	24.9	67.1
Std	1.1		2.7		0.4		1.0		10.0	

Similar to labeled dataset, the proposed method (noted as *Proposed*) was benchmarked* against those proposed by Peng (Peng et al., 2015), Kainmüller (Kainmüller et al., 2007), Wu (W. Wu et al., 2016), and Heimann (Tobias Heimann et al., 2007) on unlabeled dataset. The results are presented in **Table 4.6**. With greatest user's intervention, Peng's method outperformed the others in terms of all metrics. Meanwhile, statistical model employed by Kainmüller automatically took care of inter-subject variation. Wu's and proposed method were identical. However, automated ROI initialization by MIP and thresholding was not reliable in presence of multiple or large lesions. The proposed method was better than others in term of RVD.

Table 4.6 Comparison evaluation metrics and score

Method	VOE	RVD	ASD	RMSD	MSD	Time	CPU
Peng et al	4.6 ± 0.5	1.0 ± 0.8	0.7 ± 0.1	1.5 ± 0.4	16.9 ± 3.7	2-3	i5, RAM 8GB
Kainmüller et al	7.0 ± 2.3	-3.6 ± 3.3	1.1 ± 0.3	2.3 ± 0.7	20.9 ± 6.4	15	3.2 GHz
Wu et al	7.9 ± 1.3	1.3 ± 3.1	1.3 ± 0.2	2.5 ± 0.7	23.6 ± 8.1	0.4	2.4GH,4 GB
Heimann et al	11 ± 6.9	-1.7 ± 8.4	2.4 ± 2.3	5.1 ± 4.9	35.2 ± 21.3	10	Standard computer

Method	VOE	RVD	ASD	RMSD	MSD	Time	CPU
Model 1	8.0 ± 1.1	-0.3 ± 2.7	1.3 ± 0.4	2.5 ± 1.0	24.9 ± 10.0	1.3	i7 2.4 GH, 16GB RAM

***Note:** The scores were evaluated on 7 images, while other works were on 10 images.

With the proposed anatomical constraints, our method was specifically designed for segmenting a healthy liver [4], [17], [28] which is used for LDLT. Therefore, the liver is required to be healthy. Consequently, it did not work well in highly pathological cases, especially when lesions, with similar intensity to the background, are present on liver boundary (see in **Figure 4.10**).

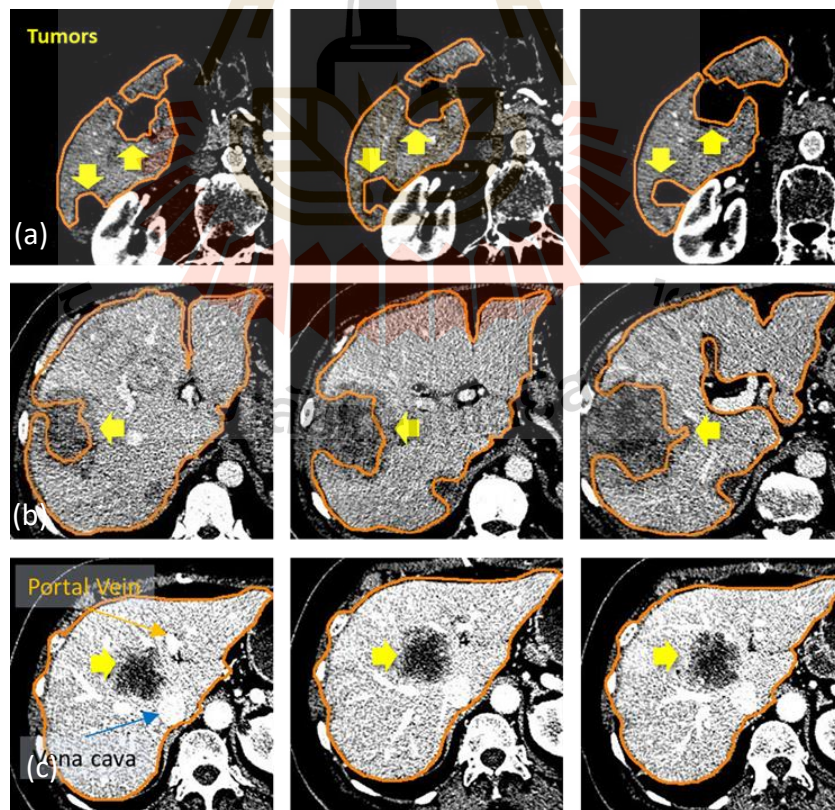


Figure 4.10 Illustration for segmentations of diseased livers

While the liver in case (c) was successfully segmented, the other cases (a and b) were not. This was due to the healthy parts enclosing the lesion (located near vena cava and portal vein entry) remained valid, according to the anatomical constraints. There exist several methods specifically developed for tumor delineation and can be integrated into our scheme during post-processing. Their detailed analyses and treatments, however, fell out of scope of this study and thus left for future investigation.

Unlike other methods which based on prior knowledge of liver (statistical based method), intensity of CT images (thresholding base method) or location and relationship of surround organs with of liver (vessel, grid, or kidney), another strong point of the proposed technique is the ability of extension for segmentation other object, such as vessel, or spleen. This is because the proposed techniques segments liver based in a few seed points initialized on liver region. **Figure 4.11** shows examples of segmentation of spleen.

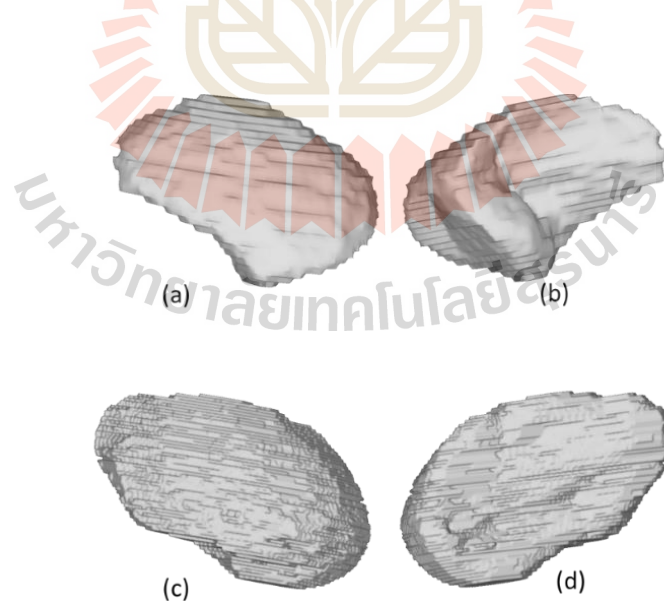


Figure 4.11 Results of spleen segmentation

4.3 Functional segmentation results

This section presents experimental process on public dataset, functional liver resections, validations and benchmarking, and relevant discussions. However, while visual assessment was straightforward, due to thorough documented liver anatomy, numerical comparison was not quite the case. This was primarily because there have not been many studies, presenting entire functional liver segmentation, and there were even fewer, validating on the common datasets. Take for instance, Oliveira et al. (Oliveira et al., 2008) demonstrated their method on 7 CT images. In that work, the method was evaluated for consistency of a specialist's perception. Similarly, Boltcheva et al. (Boltcheva et al., 2006) analyzed 7 images but of a different dataset and measured the errors between the resultant resection planes and those defined by experts. Pamulapati et al. (Pamulapati et al., 2011) studied 13 CT images. In their experiments, 20 points were randomly placed inside a liver, within 2 cm. from its edge. Their (automatically) labelled segments were validated against those identified by a radiologist. There were few studies analyzing standard references. Rusko et al. (Rusko et al., 2013), for example, used 14 out of total 20 CT images from MICCAI dataset. Their method was validated by comparing averaged volume of each segment from three test runs against those reported in the literature. Other works (Alirr & Abd Rahni, 2020; Lebre et al., 2019; Zhang et al., 2017) employed some samples from public liver images but lacking ground truth for functional segments has led to direct comparison being problematic.

To elevate standardize issues, a benchmarking framework was designed, in this study. Firstly, segmented livers were assessed visually, by an experienced radiologist. Objective evaluations were made by measuring and comparing relative hepatic sub-

volumes, at three different levels, i.e., lobes (left and right), sections (lateral, medial, anterior, and posterior), and functional segments (I-VIII), respectively.

4.3.1 Liver dataset

The recent needs for common ground truth for validating liver segmentation, and particularly the grand challenges called for MICCAI SLIVER07 initiative (T. Heimann et al., 2009). Since these data were intended for general purposes liver analyses, and due to limited visibility of the vascular networks in some subjects, they were hence discarded. Accordingly, only 12 out of 20 volumes were considered in the subsequent experiments. Apart from that of liver volume, ground truth of neither its vessels nor functional segment annotations was available. Moreover, to ensure robustness of the proposed algorithm, hepatic vasculature extracted (section 3.2.1. and 3.2.2.) were then approximated by principal vectors (Section 3.2.3.3), which were mutually considered with anatomical landmarks, to estimate liver resection planes. Consequently, detailed information on these vessels, especially at smaller scale, were not imperative. In the following experiments, SLIVER07 data were thus acceptable. This section reports both visual and numerical assessment, of the proposed automated Couinaud's functional segmentation. Critical comparisons against state-of-the-art methods and critical discussion on the findings were also given.

4.3.2 Visual assessment

To ensure functional independence among eight segments and thus rapid recovery, for instance, after graft transplant, a liver should be resected into segments, each of which has sufficient inflow and outflow blood passages. Since not only interior venous network, but also differential surface exterior, were considered, the resection paths appear natural, yet attuned well to the overall shape and anatomical landmarks,

as shown in **Figure 4.12**. As also clearly noticed on axial and sagittal views, each segment has at least a pair of in- and out flows. Furthermore, the smallest caudate segment was correctly localized by HV, IVC, entrances to MHV and PV, and LPV (**Figure 4.13**).

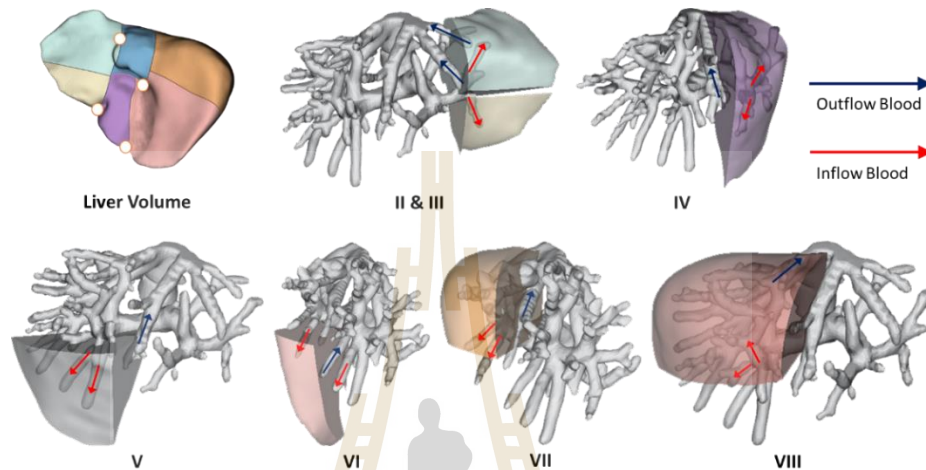


Figure 4.12 The distribution of in- and out blood flows

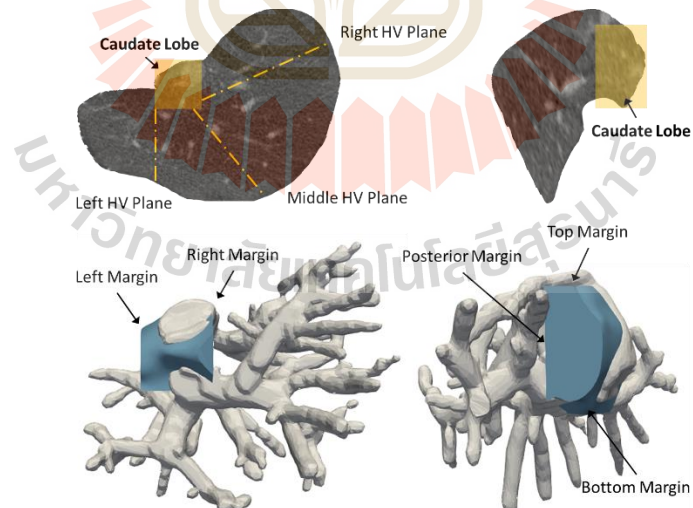


Figure 4.13 Localization of a caudate segment

(In 2D (top row) and 3D (bottom row) on axial (left column) and sagittal views (right column), showing the natural anatomical margins)

4.3.3 Numerical assessment

In addition to sufficient blood flows, there are other factors that determine the likelihood of postoperative recovery, such as minimal volume of FLRV, patient's age, their diabetes conditions, chemotherapy associated injury, blood loss during surgical procedure, and cholestasis, etc.

Among these determinants, FLRV is generally accepted as the most prevailing for postoperative outcome (Loffroy et al., 2015). Therefore, to increase patient's survival rate, this factor must be meticulously observed when planning a liver surgery. For example, to ensure regeneration capacity of a liver after tumor removal, the average FLRV is 25% (15-40%) of a total liver volume. This ratio increases up to 50% (25-90%) in cirrhotic, depending on the stage of the disease and patient's age. For transplant surgery, minimal FLRV for the living donor is 40% on average (30-50%), while the accepted graft per recipient's weight ratio is 0.8% (0.8-1.0% (Ben-Haim et al., 2001) or, as indicated in more recent studies, 0.6-1.2% (Stefan Breitenstein, Carlos Apestegui, Henrik Petrowsky, & Pierre Alain Clavien, 2009; Clavien et al., 2007; Gotra et al., 2017)).

It may be concluded that accurate calculation of relative liver volume as well as localization of its segments are critical for resection planning. Nevertheless, due to lack of common ground truth, and approximation of major vascular vectors, instead of dice similarity coefficient (DSC) or volume overlap error (VOE), this study introduced multi-level quantification, based on percentage of segmented volumes over total liver. By this approach, this work was able to validate the resultant functional segments, against those obtained by four related methods, proposed in the literature. It is

hypothesized that any misclassified (or contradicted) areas would manifest not only in anatomical violation, but also in adjacent partial volume deviation from its general cluster, at corresponding hierarchical levels.

4.3.3.1 Overview of Functional Segments

Unlike other whole liver extraction studies, where focused was placed on its shape boundaries, 12 out of 20 subjects were selected from the SLIVER07 dataset, based on the clarity of vessel appearance. Volumes of all annotated functional segments per subject are listed in **Table 4.7** and summarized in **Figure 4.14**.

Table 4.7 Percentage of functional segment volumes in liver

Subject	Seg I	Seg II	Seg III	Seg IV	Seg V	Seg VI	Seg VII	Seg VIII
1	3.2%	10.7%	3.3%	19.4%	10.5%	18.2%	10.9%	23.9%
2	3.0%	7.2%	3.0%	16.9%	10.3%	24.4%	12.2%	23.2%
3	3.5%	15.2%	6.1%	29.0%	5.4%	16.7%	9.4%	14.6%
4	3.0%	11.3%	5.3%	23.7%	9.8%	24.6%	9.2%	13.1%
5	3.6%	10.1%	3.6%	8.5%	19.6%	29.8%	11.6%	13.2%
6	1.9%	6.9%	3.0%	6.7%	10.6%	28.7%	15.7%	26.5%
7	3.2%	4.5%	3.6%	14.7%	15.8%	27.8%	13.5%	16.9%
8	3.2%	10.3%	7.1%	14.0%	6.4%	23.9%	12.1%	23.1%
9	2.4%	5.1%	4.2%	12.2%	9.7%	31.7%	14.9%	19.7%
10	1.8%	3.5%	2.7%	21.9%	3.7%	21.1%	13.4%	31.9%
11	2.1%	6.8%	7.6%	14.1%	3.7%	26.2%	13.4%	26.2%
12	3.4%	12.3%	6.3%	15.0%	11.5%	28.0%	12.7%	10.9%
Avg	2.86%	8.67%	4.65%	16.33%	9.74%	25.08%	12.42%	20.26%
STD	0.6%	3.5%	1.7%	6.3%	4.7%	4.6%	2.0%	6.5%

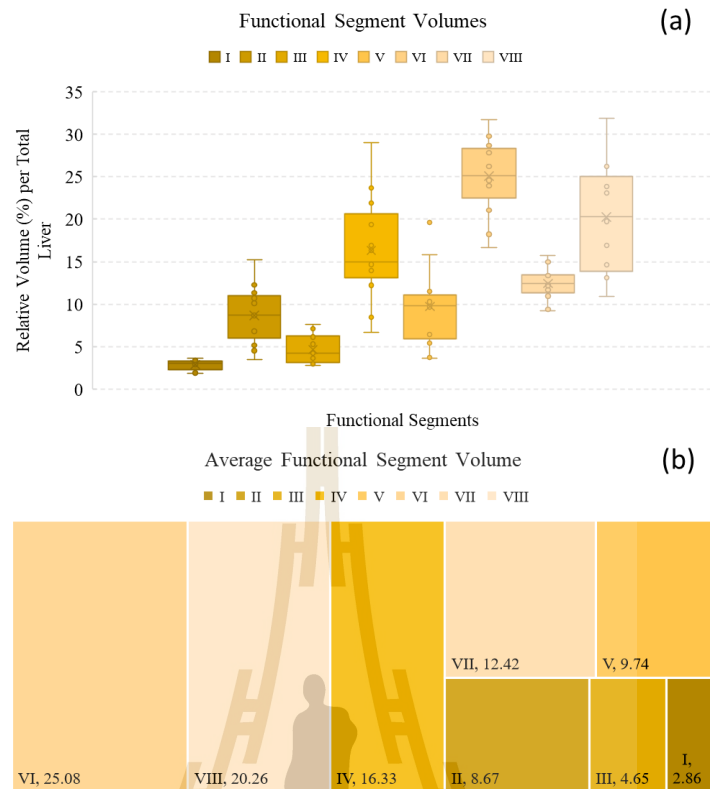


Figure 4.14 Box-Whisker (a) and tree plots (b) of segment volumes

Since the liver volumes were subject specific, and hence varied in both size and shape, their percentage values, relative to individual whole liver volume and corresponding averages are presented here. It can be noted from the table that, segment VI covered large portion of posterior section and has the most volumes (25.08%), while segment I was the smallest (2.86%).

Furthermore, besides the shape of exterior surface, hepatic venous networks played an equally important role in defining and localizing these segments. Accordingly, there existed noticeable cross-subject variability in the resulted resections. Especially, thanks to distributed vascular branches, the segment VIII

exhibited the highest variability (6.5%), followed by segment IV (6.3%), whereas segment I did the lowest (0.6%).

An example of these variations is demonstrated in **Figure 4.15**, where segment VIII was compared between subjects 10 (top) and 12 (bottom). It is clear that segment VIII in the former case was about one third (31.9%), while that in the latter one was only one tenth (10.9%) of the respective whole liver volume.

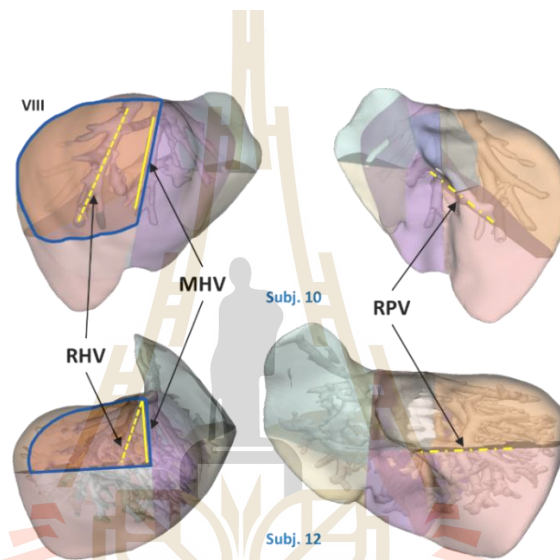


Figure 4.15 The variation of volumetry between two subjects

(Segment VIII, bounded by MHV, RHV, and RPV (solid, dashed, and dash-dotted yellow lines), was drawn on a respective liver surface (solid blue lines))

4.3.3.2 Benchmarking

To compare the proposed liver resection methods with recent related works, we performed relative volume evaluation, at three detail levels, i.e., lobes (left and right), sections (lateral, medial, anterior, and posterior), and functional segments (I-VIII), respectively. The benchmarking was made among Huang (S.-h. Huang

et al., 2008), Rusko (Rusko et al., 2013), Cheng (Y. Chen et al., 2016), Butdee (Butdee et al., 2017) et al., and the method in this work. Unfortunately, in (S.-h. Huang et al., 2008), where venous tree was projected onto a plane, by which these liver segments were separated, segment I was thus missed out due to occlusion. Likewise, despite high degree of user interaction involved, in (Rusko et al., 2013), this segmented was merged with segment IV. In Cheng et al.'s work (Y. Chen et al., 2016), only portal vein was considered, inflow and outflow blood to and from each segment was not guaranteed. Finally, segment I was explicitly estimated by Bézier curves, which required experienced judgment from an operator, unlike ours where the automated process relied on extracted anatomical landmarks. Since different labelling schemes were presented in those works, we decided to follow the most closely related one (Rusko et al., 2013) and compared segments I and IV in merging, in the following analyses.

4.3.3.3 *Evaluation at Lobe-Level*

Figure 4.16 compares the averaged lobe volumes on both side among different methods. It is evident that, regardless of the methods used, the right hemi-liver was always larger than the left one. Particularly, the results were most similar to those by Rusko et al., i.e., left: right volumes of 67.50: 32.50. This was not only because we analyzed the same dataset, but these findings also implied that the proposed resection yielded results, that were closely resemble to those obtained by that intervened by an experienced operator.

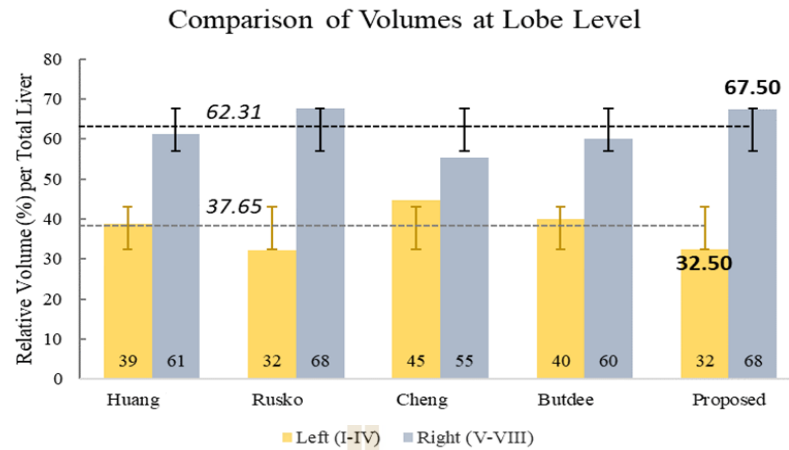


Figure 4.16 Comparisons of relative segment volumes at lobe-level

(The results closely resembled to those obtained by Rusko's method. Dotted lines are the average volumes of left and right lobes, for all methods)

4.3.3.4 Evaluation at Section-Level

Table 4.8 presents averaged proportions of volume sizes in 4 sections, i.e., lateral, medial, anterior, and posterior. It can be noted that this segmentation concurred with Butdee's for anterior section (30.0 vs. 29.4%) and with Rusko's for both lateral (13.3 vs 12.2%) and medial (19.2 vs. 20.0) sections.

Table 4.8 Averaged proportions (in %) of volume sizes in four sections

Methods	Lateral	Medial	Anterior	Posterior
Huang	14.1	24.7	39.3	21.9
Rusko	12.2	20.0	40.2	27.6
Cheng	26.7	18.1	23.3	32.0
Butdee	17.9	22.1	29.4	30.6
Proposed	13.3	19.2	30.0	37.5

To gain better insights into differential characteristics, PCA was applied to these relative volumes (by column) over these methods (by row). Their respective projections onto the principal 2D (eigen) space are plotted in **Figure 4.17**. It is evident from the figure that, this technique yielded similar sectional proportions to the semi-automatic methods (Butdee et al., 2017; Rusko et al., 2013) (dotted arrows), within 2.0σ radius. It is also worth emphasizing here that, in this analysis, section I was merged with IV, and associated with medial section.

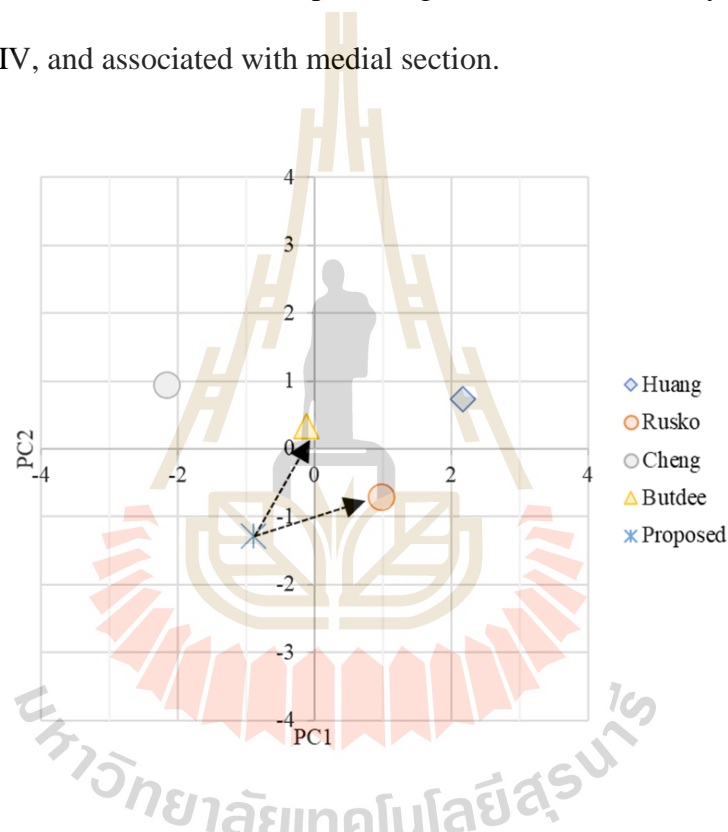


Figure 4.17 The distributions of volume sizes evaluated at section level

(By five methods and projected onto a 2D principal plane)

4.3.3.5 *Evaluation at Functional Section-Level*

Similar to the previous level, **Table 4.9** presents the averaged proportions of volume sizes in all functional segments.

Table 4.9 Averaged proportions (in %) of volume sizes in functional segments

Methods	II	III	I, IV	V	VI	VII	VIII
Huang	3.0	11.1	24.7	20.6	6.1	15.8	18.7
Rusko	5.9	6.3	20.0	16.2	10.6	16.8	24.0
Cheng	8.4	18.2	18.1	6.3	15.6	16.4	16.9
Butdee	13.1	4.8	22.1	11.4	18.6	12.0	18.0
Proposed	8.7	4.6	19.2	9.7	25.1	12.4	20.3

The above results indicated that the results were most consistent with Butdee's, for four out of seven segments, i.e., II, V, VI, and VII. This is mainly because we took the same approach in constructing the HV plane. For segments II, I & IV, and VIII, the results were comparable to those by Cheng, Rusko, and Huang et al.'s works, respectively. Likewise, these are because for these segments we referred to the similar markers as did those works.

PCA was also applied to these relational data, similar to those evaluated at the section-level, and the corresponding projections are plotted in **Figure 4.18**, where individual subjects, analyzed by this method are also shown. Contradicted segment is manifest in partial deviation from its general cluster.

Unlike **Figure 4.17**, however, due to higher dimension (8) than methods (5), PCA was applied to all 12 subjects and averages of compared methods ($12 + 4 = 16 > 8$). Based on Mahalanobis's distance, all instances but Huang's average, lied within 2.4σ radius (bounded by subject 10) around the average. Apart from that, the sample average was closest to Butdee's ($d = 1.0\sigma$), followed by Rukso's (2.1σ), and Cheng's (2.4σ). Despite similar volumes ratios, the proposed method outperformed

these semi-automatic ones, especially in terms of the extent of user interaction and expertise involved, and hence inter- and intra-observer variability (Keegan et al., 2004). Take Rukso's method, for instance, between three trial runs, the volume variations ranged 2.8–5.6%, which is roughly at similar significance levels as those among five methods, presented in Table V.

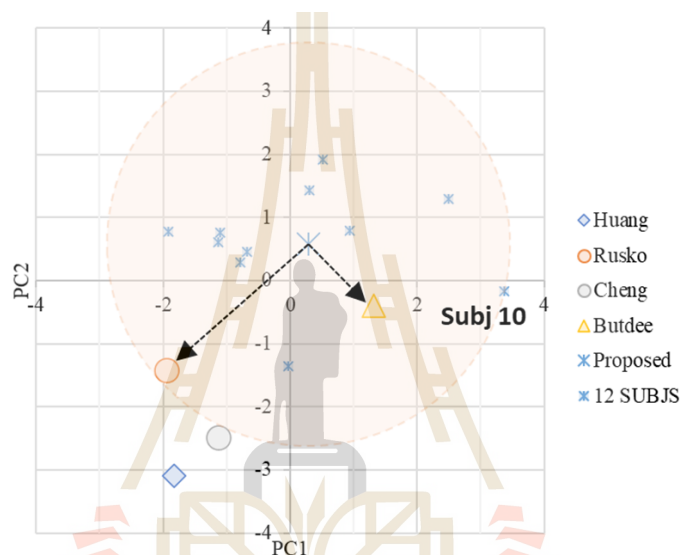


Figure 4.18 The distributions of volume sizes evaluated at segment level

(By five methods and projected onto a 2D principal plane. The projections of individual samples analyzed by the method are included)

In addition to state-of-the-art methods, a range of computer software has also been developed based on Couinaud's definition. They are widely applied in clinical practice and worth mentioned here (Xiaopeng Yang, Wonsup Lee, Yunhee Choi, & Heecheon You, 2012), e.g., MeVis LiverAnalyzer™ (MeVis Medical Solution, Germany), and Synapse Vincent™ (Fujifilm, Japan), etc. While the former

requires its user to submit CT images and then wait for full report, the latter is interactive and thus depends greatly on user's expertise, e.g., significant manual adjustment is required for regions with poor vascular clearance, etc. Therefore, to resolve these limitations, algorithmic enhancement has still remained vital and been an active area of research (Alirr & Abd Rahni, 2020; Butdee et al., 2017; Y. Chen et al., 2016; Lebre et al., 2019; X. Yang, Yang, Hwang, et al., 2018; Zhang et al., 2017).

4.4 Liver parameterization

In addition, to elucidate the merits of the proposed cross-subject correspondence of liver resection, a pair of extracted liver surfaces were selected and denoted as source (S_1) and target (S_2). After segmentation, these surfaces were first preprocessed by the MeshFix tool (Attene, 2010), to remove degenerated and self-intersecting triangles, to fill holes, and to smooth their vertices. Without a loss of generalization ability, each processed mesh was resampling to contain 12k vertices (to reduce mesh elements to a manageable size, while maintaining visual appearance). Subsequently, functional resection was performed on each liver, resulting in eleven landmarks. A description of these landmarks is summarized in **Figure 4.19**.

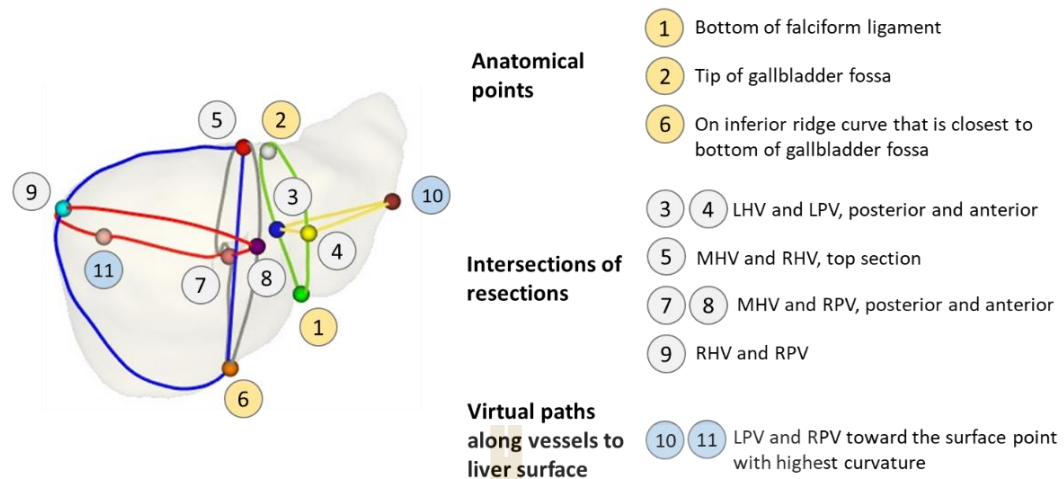


Figure 4.19 Landmark annotations

(LHV, MHV, and RHV refer to the resection paths along the left, middle, and right hepatic veins, respectively; LPV and RPV refer to those along the left and right portal veins, respectively)

Out of these landmarks, three anatomical points (1, 2, and 6) were explicitly detected on the gallbladder fossa and falciform ligament, while the other six points (3–5 and 7–9) were intersections of resection paths; the last two points (10, 11) lay on the virtual paths along the left and right portal veins (PV) passing through the liver surface, where it exhibited the highest curvature.

Example localization of landmarks and the respective mapping are illustrated in **Figure 4.20**. It is revealed by the distortion plots with a slight deviation from 0 degrees that, by using the FLASH algorithm, stabilized and bijective conformal mapping was obtained. The corresponding source to target registrations are shown in **Figure 4.21**

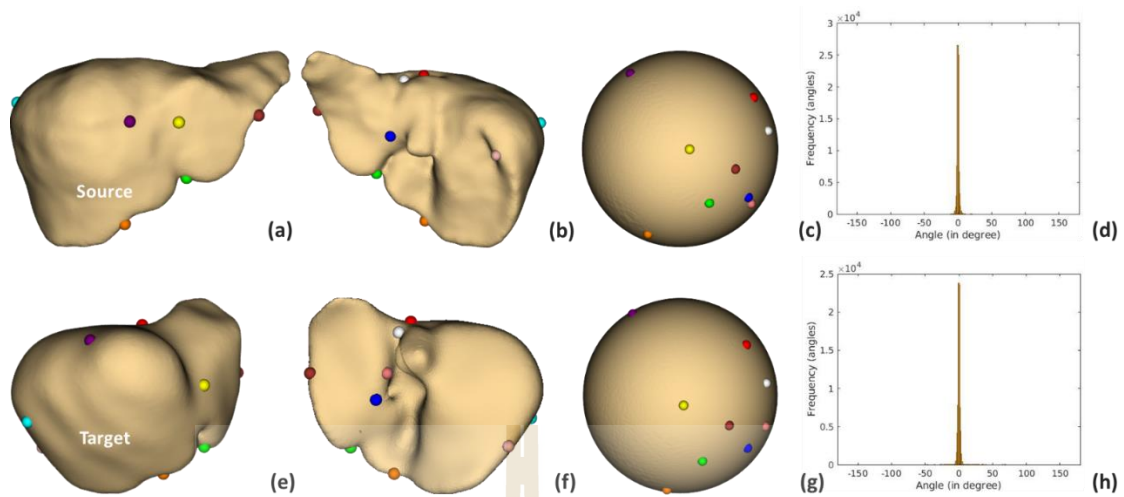


Figure 4.20 The SCM with landmark constraints.

The first and second rows present the source and target livers in anterior (**a,e**) and posterior (**b,f**) views. On the spheres in (**c**) and (**g**) are shown their landmarks, aligned by constrained mapping. The distortions between liver and spherical mapping of source and target livers are plotted in (**d**) and (**h**), respectively.

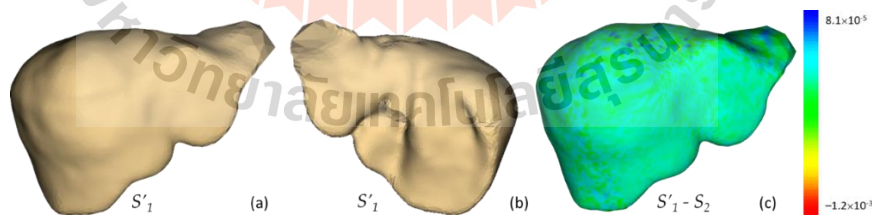


Figure 4.21 The registration (S'_1) of source (S_1) to target (S_2)

(in anterior view (**a**), posterior view (**b**), and the overlaid error distance (**c**). The errors of this example were between -1.2×10^{-3} to 8.1×10^{-5})

To evaluate the correspondence between source and target resections, the resection on the target liver (\mathcal{L}_2), based on its interior vasculature was projected onto the registered source liver, (S'_1), denoted as (\mathcal{L}'_1). Subsequently, the Hausdorff distance between this projected resection and that actually performed on the source (\mathcal{L}_1) was computed by using MeshLab, developed by the Visual Computing Lab of the ISTI-CNR based on the VCG library (Cignoni et al., 2008). Figure 4.22 depicts the resection on source and target livers, their conformal parameterizations, and the projected resection by symmetric correspondences.

Table 4.10 lists the maximum, minimum, mean and root mean square errors of the Hausdorff distances between the correct (determined from its actual vasculature) and projected resection on the source liver.

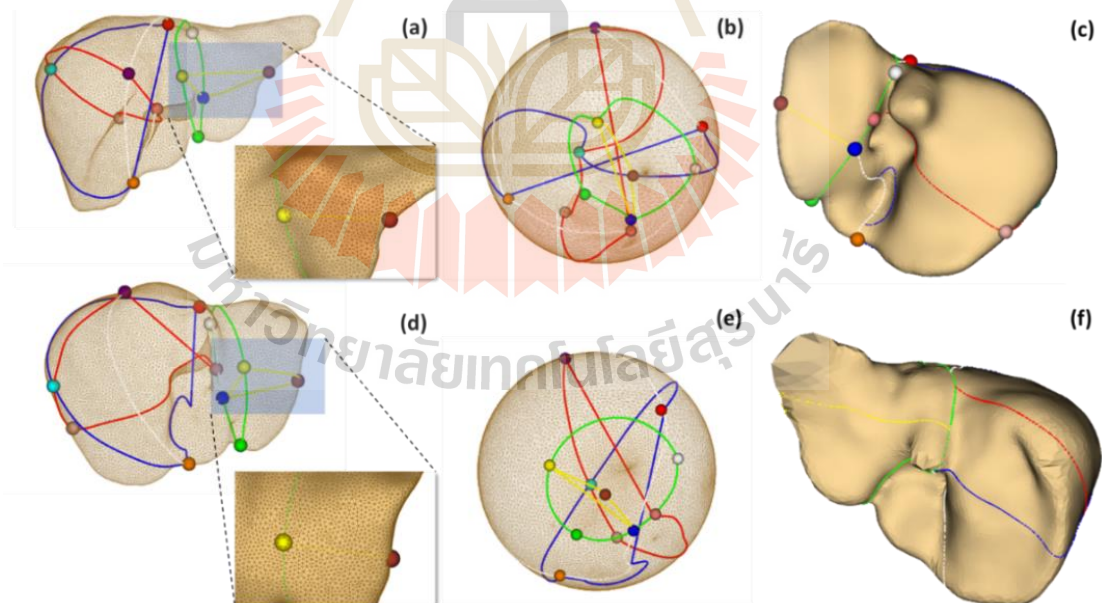


Figure 4.22 An example of resection on source and target livers

(The resection of source (a) and target livers (d), based on hepatic vascular network, their respective SCM (b,e), and the projection of target resection (c) onto the registered source liver (f), by using symmetric correspondence)

Table 4.10 The Hausdorff distance between the correct and projected paths

Resection Paths	Max [mm]	Min [mm]	Mean [mm]	RMS [mm]
LHV	33.12	0.15	13.03	15.50
MHV	38.53	0.45	18.52	21.54
RHV	72.77	0.36	30.77	36.32
LPV	24.10	0.23	13.09	14.32
RPV	62.12	1.06	40.55	43.56
Average	46.130	0.452	23.192	26.249

It is evident from **Table 4.10** that the projections of LHV and LPV exhibited the least error, which implies they are the most consistent between the projected and correct hepatectomy. In which case, when provided with resection paths on the target liver, that one source could be sufficiently determined by conformal correspondence, without the extraction of the entire hepatic vascular network. On the contrary, those on the right hemi-liver exhibited larger errors. This was due to a greater variation of the corresponding segments (e.g., segments IV and VIII).

It is thus worth emphasizing that the cost function given in Equation (2.39) is aimed at balancing between minimized distortion and landmark alignment. This implies that exact alignment was not necessarily guaranteed. In fact, in the original FLASH

implementation, six sulci, each of which consisted of multiple vertices in a cerebral cortex, were imposed to evenly distribute errors. However, since the liver is much morphologically diverse, localized alignment is suggested. To demonstrate this proposition, five anatomical landmarks relevant to LHV and LPV (i.e., 1, 2, 3, 4, and 10) were imposed as constraints. The corresponding errors between the correct and projected resection are shown in **Table 4.11**.

Table 4.11 The Hausdorff distance between the correct and projected paths

Resection Paths	Max	Min	Mean	RMS
	[mm]	[mm]	[mm]	[mm]
LHV	7.85	0.12	4.05	4.44
MHV	39.18	0.16	21.54	23.81
RHV	31.27	0.31	16.94	19.48
LPV	5.13	0.34	1.94	2.09
RPV	85.42	0.39	40.92	48.27
Average	33.707	0.266	17.074	19.618

Figure 4.23 compares these min, max, and mean resection errors between imposing 11 and 5 landmark constraints. It is evident that, by localizing the constraints, the landmarks and hence the relevant resection, i.e., LHV and LPV, were more consistent. However, it could lead to greater errors in other segments, e.g., MHV and RPV paths. Therefore, care must be observed when selecting anatomical landmarks, as they play a vital role in resection consistency.

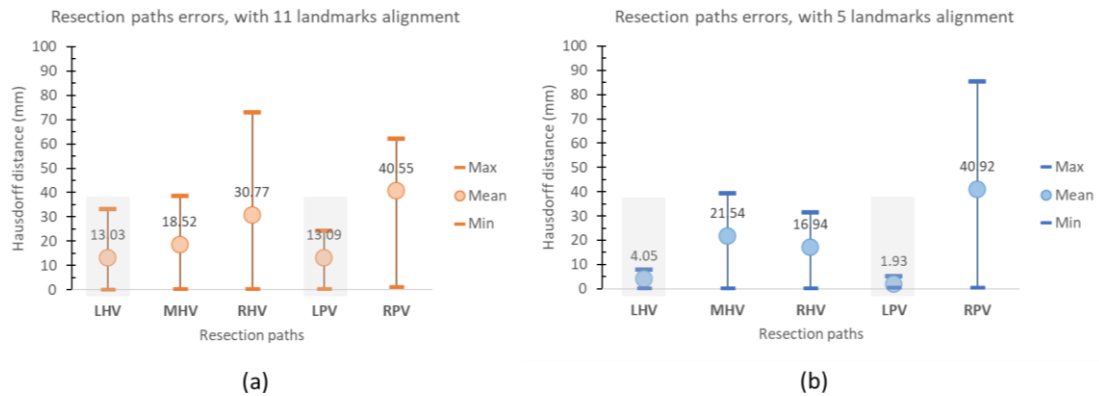


Figure 4.23 The error distances between projected and correct resection paths

4.5 Liver surgical simulation

In LDLT, the pre-operative assessment of GV assists surgeons to estimate the implanted graft before operating in real liver. This work used landmarks matching SCM in combination to rigid body transformation to estimate graft. It is noted that, not all liver as well as segments are compatible. In this case, the estimated volume and its shape may be bad. In practice, the surgeons may base on specified requirements to decide whether a donor's liver is suitable or not. Therefore, there are some segments are selected for demonstration in current research. Firstly, a few landmarks specify for a region are used for SCM constraint (see in **Figure 4.19**). Then the RVD error and distance error are measured. The **Table 4.12** validates the estimated volume with actual volume of the donor.

Table 4.12 The RVD and error between estimated and actual volume

Example	Landmarks ID	RVD [%]	Error distance [mm]
#1	2,3,4,10	7.1	49.0
#2	1,3,4,10	2.2	7.0
#3	1,3,4,10	5.9	8.1
#4	1,2,3,4,10	-9.0	29.0
#5	5,6,7,8,9,11	1.2	35.3

The **Table 4.13** shows the RVD error and distance error between actual, estimated volume (on donor) and actual volume (on recipient).

Table 4.13 The RVD and error distance.

Example	Landmarks ID	RVD-1 [%]	RVD-2 [%]	Error distance [mm]
#1	2,3,4,10	-0.1	7.0	28.7
#2	1,3,4,10	-6.1	-4.0	10.8
#3	1,3,4,10	24.4	31.7	13.6
#4	1,2,3,4,10	10.6	0.6	25.0
#5	5,6,7,8,9,11	-0.8	-3.5	52.4

In **Table 4.13**, RVD-1 is the error between actual volume of donor and actual volume of recipient, while RVD-2 denotes the error between estimated volume and actual volume in recipient. In both tables, the lower and error distance, the more compatible between recipient and donor's graft. The minus (-) in RVD implies the estimated volume smaller than the actual one (underestimation), otherwise it is bigger

(overestimation). In **Table 4.12**, the case #1 and #5 have RVD of 7.1% and 1.2%., but the error distances are large (49 and 35.3, respectively). Due to the compatibility, case #2 and #3 have low error. However, RVD-1 and RVD-2 of case #3 in **Table 4.13** are too large, so it is not suitable for liver transplantation. The estimated graft in case #4 is less than actual volume (RVD of -9.0%). In practice, the difference between the GV in pre-operative surgery (calculated by the assumptive plane) and post-operative (by actual plane) may be 5%, this number may increase up to 10% in comparing to actual graft (Kwon et al., 2018). In another work, Wang et al (F. Wang et al., 2011) performed a comparison between three methods for estimation GW. The first method used CT volumetry, referred as radiological graft volume (RGV), while the second one combined standard liver volume (SLV) and RGV percentage with respect to TVL from CT image. The last method based on portal vein diameter and SLV. They reported the error of $18.5\% \pm 14.5$, $11.7\% \pm 15.4\%$, and $9.5\% \pm 12.8\%$ corresponding to three methods, respectively. They assume that the liver density is $1\text{g}/\text{cm}^3$, it led to the GW is the same to GV. In some materials, the rate between GW and GV may be 0.84 (or 0.82) in right lobe and 0,85 in left lobe (Pinheiro et al., 2017; Yoneyama et al., 2011). The landmarks, overlaid regions and errors between recipient, actual and estimated volumes are illustrated respectively in **Figure 4.24**.

By using this technique, the reconstructed segments were no longer limited to planar separation and were hence much more flexible to the actual morphology of an underlying shape. To lessen estimation errors, a statistical atlas of the livers may be built over a training set, and then its mean shape (instead of an arbitrary instance) may be used as a reference (Horkaew & Yang, 2004), while regulating Equation (2.39) by

plausible variation, only found in this set. Its detailed analyses and discussion, however, fall out of the current scope and are left for future investigation.

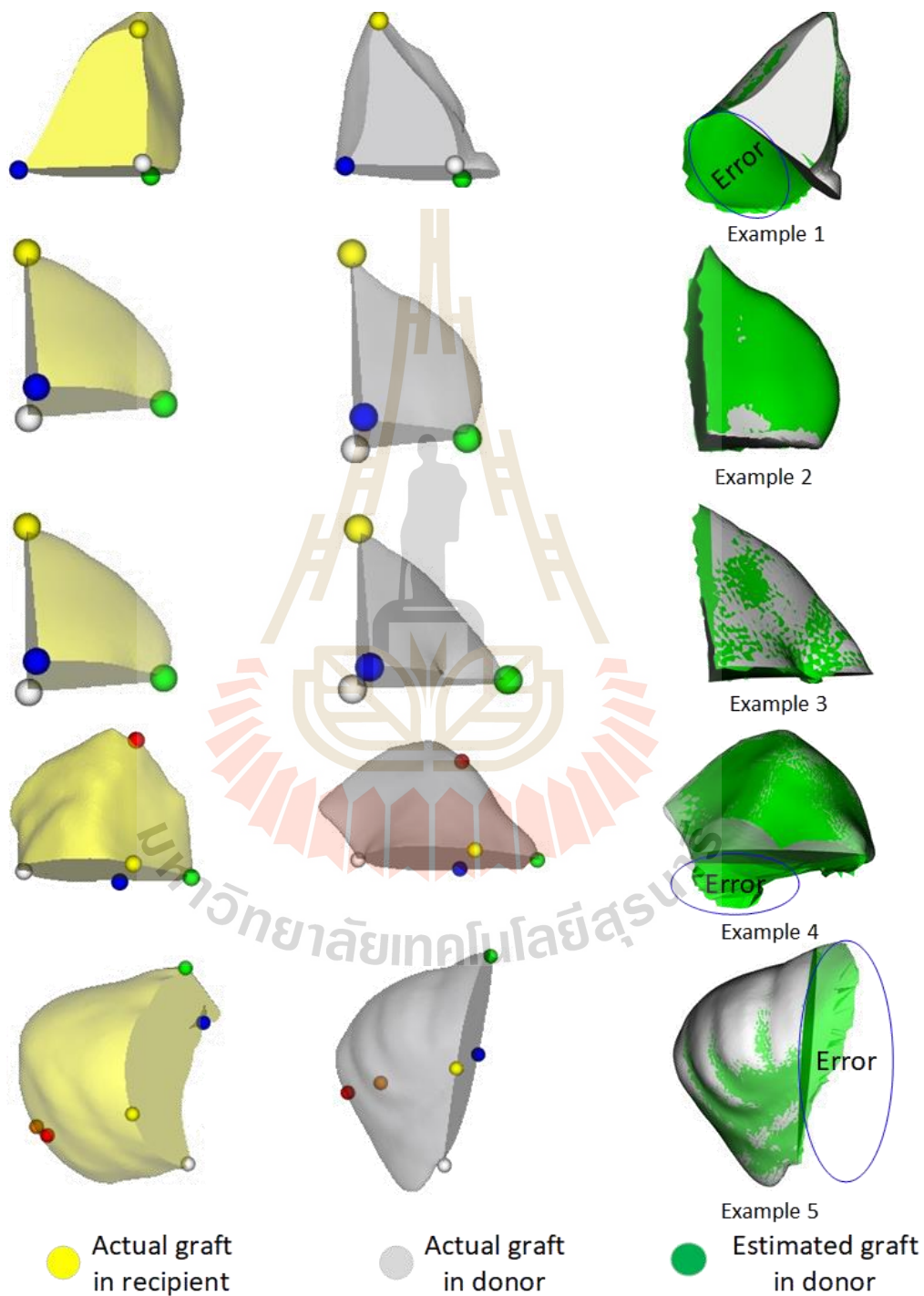


Figure 4.24 Illustration of estimation of graft in examples

CHAPTER 5

CONCLUSION AND FUTURE WORK

This study focused on solving the problem of liver segmentation, functional segmentation in CT image, and application of SCM with similarity transformation for estimation the GV.

Segmenting a liver from a 3D CT image has remained a challenging area of research. This is mainly due to the inherent characteristics of this imaging modality that impede it from rendering clear separation between the liver and connective abdominal parts. In addition, the inhomogeneity of interior voxels has often contributed to erroneous liver extraction. According to the recent survey, model-based and interactive methods offered by far the most promising results. However, anatomical variations across the subject population and high geometrical resolution call for a prohibitively large, annotated dataset for realistic model construction. On the one hand, given a model that captures all plausible variations, a deformable model approach can be adopted to automatically segment a liver. On the other hand, without such priors, user intervention or empirical knowledge is often required, for example, to initialize seed points, estimate rough contours, or make small adjustments to segmented results.

This research proposed a semi-automatic method for segmenting a liver from CT images. Its main contribution was to balance between robustness, accuracy, processing time, while keeping user interaction minimal. More specifically, the probabilistic model of pixel statistics was first built from a user-defined seed point and then enhanced by multi-slice RL. Subsequently, the liver was extracted using the GC algorithm. During graph optimization, a novel local texture compatibility function called anisotropic measure was integrated into boundary energy to enhance its robustness. Finally, BN detection and contour constraints were employed to resolve the remaining under- and over-segmentation. The experimental results, both visual and numerical, reported herein demonstrated that the proposed method not only gave comparable segmentation accuracy to state-of-the-art methods, but was also faster and more consistent than the majority in its class. The proposed technique is designed to segment on CT image of liver which includes a series of slices where shape of object is not much change between two adjacent slices. It is also worth emphasizing that this favorable performance relied neither on any statistical model nor specific anatomical priors of the liver. So, it can thus be readily applied to other similar abdominal organs, such as the spleen or vessel. In segmentation of spleen, for example, user is required to initialize seed points on spleen region. The probabilistic map is then applied to highlight spleen area. The latter steps are applied as in liver segmentation. Parallel or hardware device programming are popular techniques to speed up the algorithm. The vital mechanism of the former is to divide a process into multiple blocks by using multiple threads or CPU, meanwhile the latter is to use hardware devices such as graphics card instead CPU. In this study, proposed algorithm was implemented on notebook. However, it is possible to improve the processing by applying parallel programming on building

probabilistic map, relaxation labeling and refinement steps by dividing images into 8 (or 16) independent blocks, each block contains $N/8$ (or $N/16$) images.

Regarding functional segmentation, this study presented a novel scheme for labeling functional segments of a liver mass and tracing on its surface virtual surgical paths for preoperative liver resection. This scheme took into account liver morphology, its interior vascular network (deep landmarks), and anatomical landmarks (surface landmarks). Given a liver and its vascular surfaces extracted from 3D CT, we divided a liver into eight functional segments, according to Couinaud's definition. Among key hepatic markers, the proposed method was able to identify and localize gallbladder fossa and falciform ligaments on the liver surface, by means of differential geometry operations. Unlike existing methods, these and other markers considered herein were practical and much faithful to hepatic anatomy than manually specified cutting planes or curves. Besides only a few markers being placed by a user on major vessels, the rest of the process was automatic. Accordingly, this significantly reduced observer variability, user fatigue, and needs of radiological expertise. To the best of my knowledge, existing schemes estimated the caudate lobe (segment I), based primarily on a portal vein or manually drawn parametric curves, or more often than not neglected this segment all together. To resolve this issue, the proposed method meticulously defined caudate boundaries based on surrounding segments and local planes. Particularly the extracted gallbladder fossa and falciform ligament forms natural landmarks that enabled its separation from lateral, medial, and right sections. Moreover, the principal vectors approximating main HV, and PV branches ensured necessary blood passages in and out of each segment. To demonstrate its merits, the proposed scheme was validated both visually and numerically on standard public liver dataset. A Total of twelve subjects were undergone virtual

preoperative resection. The resulted functional segments were subsequently validated and benchmarked against four related methods. Numerical evaluations at three volumetric levels were performed and discussed. One of this main contributions was well motivated by a previous work presented in (Boltcheva et al., 2006), where gallbladder fossa and falciform ligament were both considered. However, with this work, the structures of interest were automatically identified, by optimizing parametric curvatures, based on their two-manifold distribution. Another key contribution was that, in addition to referring to these structures and the centroid of liver mass, the method also detected and analyzed its vasculature and other salient anatomical markers, in building resection planes. Unfortunately, numerical measurements were not reported in (Boltcheva et al., 2006), it were thus unable to compare this results with theirs. That said, the proposed methods corresponded well to other counterparts, particularly to those depending on fair amount of interaction from an experienced user. To summarize, successful liver resection procedure is characterized by accurate calculation of postoperative FLRV and functional independence of affected regions. Thus, it is anticipated that the proposed virtual resection method will benefit both preoperative planning and surgical intervention. Future directions worth considered are much precise extraction of vessels and their centerlines (Zhang et al., 2017) (Moccia et al., 2018) and building statistical atlas (Horkaew & Yang, 2004) of functional segments model. Empirical results reported herein have also confirmed large variations of vascular structures (especially HVs) (Fang et al., 2012) and related segments. It is thus worth further explore and correlate these resections with, for examples, biliary tree, by using CT-MRCP (MR cholangiopancreatography) perfusion and functional parenchyma, by using particular contrast material.

Having segments, the proposed virtual resection scheme could be integrated with other computerized therapeutic interventions. For example, percutaneous radiofrequency ablation (RFA) is another prospective area of application. This non-invasive treatment first locates the tumor and then precisely destroys it by heat through a needle. To this end, Egger et al. (Egger et al., 2015) constructed a 3D spherical graph at a seed point. Subsequently, max-flow min-cuts was used to segment the ablation zone from the background. An automatic approach was taken by Wu et al. (P. H. Wu, Bedoya, White, & Brace, 2021). With their method, fuzzy c-mean clustering and cyclic morphology were employed to extract and then refine the ablation zone. Having this zone extracted (or during the procedure), the proposed scheme could be applied to determine the enclosing liver and functional segments, to gain a comprehensive view of the overall treatment.

It has been known that the estimation of graft to be implanted was crucial to avoid liver insufficiency post-operation in liver transplantation. This study integrated SCM with similarity transformation to predict the shape and size of graft. Firstly, a few anatomical landmarks were chosen in both recipient and donor's liver at a specified area. Then the landmark matching map will be utilized to align landmarks. Then the symmetric corresponding surface points are obtained. Lastly, the similarity transformation is used to construct interior points of the estimated region. The objective is to find the compatible graft in donor with recipient.

Although obtained some results, the current work still has some limitations:

- The first one is the complete IVC removal, which is vital for preoperative planning and computerized surgical simulation. This can be done by segmenting the liver and its vasculature simultaneously. Furthermore, errors may be propagated during

post-processing. A novel user experience (UX) and interface (UI) design could help make manual editing much more intuitive and efficient. Lastly, the proposed method did require a seed point from a user. To fully automate the segmentation, the seed point may be chosen, such that the resultant probabilistic map virtually covers an estimated VOI.

- Second, the functional segmentation is based on vessel network enable to ensure the independence of segments. Therefore, beside segmented liver, the vascular system must be separated into HV and PV.

- Estimation of GV which supports surgeons in finding the suitable donor, bases on a few landmarks may be not enough to constrains the map. In some application of brain analysis, this number may up to hundred or more than. Moreover, the estimation process depends on the compatibility between recipient and donor's liver. Therefore, if this requirement is not satisfied, it may lead to over or under estimation. In conclusion, the using of the proposed technique should in combination to conventional methods would be useful.

REFERENCES

- Abdalla, E. K., Adam, R., Bilchik, A. J., Jaeck, D., Vauthey, J. N., & Mahvi, D. (2006). Improving resectability of hepatic colorectal metastases: expert consensus statement. **Ann Surg Oncol**. 13(10): 1271-1280.
- Abdalla, E. K., Barnett, C. C., Doherty, D., Curley, S. A., & Vauthey, J.-N. (2002). Extended Hepatectomy in Patients With Hepatobiliary Malignancies With and Without Preoperative Portal Vein Embolization. **Archives of Surgery**. 137(6): 675-681.
- Adams, R., & Bischof, L. (1994). Seeded region growing. **IEEE Transactions on Pattern Analysis and Machine Intelligence**. 16(6): 641-647.
- Agha, R. A., & Fowler, A. J. (2015). The role and validity of surgical simulation. **International surgery**. 100(2): 350-357.
- Akdur, A., Kirnap, M., Ozçay, F., Sezgin, A., Ayvazoğlu Soy, E., Yarbug, F., . . . Haberal, M. (2015). Large-for-Size Liver Transplant: A Single-Center Experience. **Experimental and clinical transplantation : official journal of the Middle East Society for Organ Transplantation**. 13: 108-110.
- Alirr, O. I., & Abd Rahni, A. A. (2020). Automatic atlas-based liver segmental anatomy identification for hepatic surgical planning. **Int J Comput Assist Radiol Surg**. 15(2): 239-248.

- Allard, M.-A., Lopes, F., Frosio, F., Golse, N., Sa Cunha, A., Cherqui, D., . . . Vibert, E. (2017). Extreme large-for-size syndrome after adult liver transplantation: A model for predicting a potentially lethal complication. **Liver Transplantation**. 23(10): 1294-1304.
- Altarawneh, N. M., Luo, S., Regan, B., & Tang, G. (2015). 3D Liver Segmentation from CT Images Using a Level Set Method Based on a Shape and Intensity Distribution Prior. **Computer and Information Engineering**. 9(12).
- Altarawneh, N. M., Luo, S., Regan, B., & Tang, G. (2015). 3D Liver Segmentation from CT Images Using a Level Set Method Based on a Shape and Intensity Distribution Prior. **Computer and Information Engineering**. 9(12): 2442-2448.
- Antiga, L. (2002). **Patient-specific modeling of geometry and blood flow in large arteries**. Ph.D. Thesis. Politecnico Di Milano. Italy.
- Antonidoss, & Kaliyamurthie, K. P. (2014). Segmentation from images using adaptive threshold. **Middle - East Journal of Scientific Research**. 20: 479-484.
- Attene, M. (2010). A lightweight approach to repairing digitized polygon meshes. **The Visual Computer**. 26(11): 1393-1406.
- Avşar, T. S., & Arıca, S. (2018, 2018//). Automatic Segmentation of Computed Tomography Images of Liver Using Watershed and Thresholding Algorithms. In **Proceesings of the EMBEC & NBC 2017** (pp. 414-417). Singapore.
- Awad, A., & Hassaballah, M. (2016). **Image Feature Detectors and Descriptors** (Vol. 630).

- Bartholomew, D. J. (2010). Principal Components Analysis. In P. Peterson, E. Baker, & B. McGaw (Eds.), **International Encyclopedia of Education** (pp. 374-377). Oxford: Elsevier.
- Baumgarten, D. (2006). Fundamentals of Body CT, 3rd ed. **American Journal of Roentgenology**. 187(4): W444-W445.
- Beck, A., & Aurich, V. (2007). HepaTux – A Semiautomatic Liver Segmentation System. **Proceedings of the 3D Segmentation in The Clinic: A Grand Challenge**.
- Beichel, R., Bauer, C., Bornik, A., Sorantin, E., & Bischof, H. (2007). Liver Segmentation in CT Data: A Segmentation Refinement Approach. **Proceedings of the 3D Segmentation in The Clinic: A Grand Challenge**.
- Beichel, R., Bornik, A., Bauer, C., & Sorantin, E. (2012). Liver segmentation in contrast enhanced CT data using graph cuts and interactive 3D segmentation refinement methods. **Med Phys**. 39(3): 1361-1373.
- Ben-Haim, M., Emre, S., Fishbein, T. M., Sheiner, P. A., Bodian, C. A., Kim-Schluger, L., . . . Miller, C. M. (2001). Critical graft size in adult-to-adult living donor liver transplantation: Impact of the recipient's disease. **Liver Transplantation**. 7(11): 948-953.
- Bidgood, W. D., Jr., & Horii, S. C. (1992). Introduction to the ACR-NEMA DICOM standard. **Radiographics**. 12(2): 345-355.
- Bidgood, W. D., Jr., Horii, S. C., Prior, F. W., & Van Syckle, D. E. (1997). Understanding and using DICOM, the data interchange standard for biomedical imaging. **Journal of the American Medical Informatics Association : JAMIA**. 4(3): 199-212.

- Boltcheva, D., Passat, N., Agnus, V., Jacob-Da Col, M.-A., Ronse, C., & Soler, L. (2006). Automatic anatomical segmentation of the liver by separation planes - art. no. 61411A. **Proceedings of SPIE - The International Society for Optical Engineering**. 6141.
- Bookstein, F. L. (1989). Principal warps: thin-plate splines and the decomposition of deformations. **IEEE Transactions on Pattern Analysis and Machine Intelligence**. 11(6): 567-585.
- Boykov, Y., & Jolly, M. P. (2001). Interactive Graph Cuts for Optimal Boundary & Region Segmentation of Objects in N-D Images. In **Proceedings of the Computer Vision** (pp. Vancouver, BC, Canada, Canada).
- Boykov, Y., & Kolmogorov, V. (2004). An experimental comparison of min-cut/max-flow algorithms for energy minimization in vision. **IEEE Trans Pattern Anal Mach Intell**. 26(9): 1124-1137.
- Bozkurt, B., Emek, E., Arıkan, T., Ceyhan, O., Yazıcı, P., Sahin, T., . . . Tokat, Y. (2019). Liver Graft Volume Estimation by Manual Volumetry and Software-Aided Interactive Volumetry: Which is Better? **Transplantation Proceedings**. 51(7): 2387-2390.
- Bray, F., Ferlay, J., Soerjomataram, I., Siegel, R. L., Torre, L. A., & Jemal, A. (2018). Global cancer statistics 2018: GLOBOCAN estimates of incidence and mortality worldwide for 36 cancers in 185 countries. **CA Cancer J Clin**. 68(6): 394-424.
- Brechbuehler, C., Gerig, G., & Kuebler, O. (1992). **Surface parametrization and shape description** (Vol. 1808): SPIE.

- Breitenstein, S., Apestegui, C., Petrowsky, H., & Clavien, P. A. (2009). "State of the art" in liver resection and living donor liver transplantation: a worldwide survey of 100 liver centers. **World J Surg.** 33(4): 797-803.
- Breitenstein, S., Apestegui, C., Petrowsky, H., & Clavien, P. A. (2009). "State of the Art" in Liver Resection and Living Donor Liver Transplantation: A Worldwide Survey of 100 Liver Centers. **World Journal of Surgery.** 33(4): 797.
- Brown, B. M., Filly, R. A., & Callen, P. W. (1982). Ultrasonographic anatomy of the caudate lobe. **Journal of ultrasound in medicine : official journal of the American Institute of Ultrasound in Medicine.** 1(5): 189-192.
- Butdee, C., Pluempitiwiriyaewej, C., & Tanpowpong, N. (2017). 3D plane cuts and cubic Bézier curve for CT liver volume segmentation according to Couinaud's classification. **Songklanakarin Journal of Science and Technology.** 39: 793-801.
- Chartrand, G., Cresson, T., Chav, R., Gotra, A., Tang, A., & De Guise, J. A. (2017). Liver Segmentation on CT and MR Using Laplacian Mesh Optimization. **IEEE Trans Biomed Eng.** 64(9): 2110-2121.
- Chartrand, G., Cresson, T., Chav, R., Gotra, A., Tang, A., & DeGuise, J. (2014, 29 April-2 May 2014). SEMI-automated liver CT segmentation using Laplacian meshes. In **Proceedings of the 2014 IEEE 11th International Symposium on Biomedical Imaging (ISBI)** (pp. 641-644).
- Chen, E. L., Chung, P. C., Chen, C. L., Tsai, H. M., & Chang, C. I. (1998). An automatic diagnostic system for CT liver image classification. **IEEE Trans Biomed Eng.** 45(6): 783-794.

- Chen, M. F., Hwang, T. L., & Hung, C. F. (1991). Human liver regeneration after major hepatectomy. A study of liver volume by computed tomography. **Annals of surgery**. 213(3): 227-229.
- Chen, X., Udupa, J. K., Bagci, U., Zhuge, Y., & Yao, J. (2012). Medical image segmentation by combining graph cuts and oriented active appearance models. **IEEE Trans Image Process**. 21(4): 2035-2046.
- Chen, Y., Wang, Z., Zhao, W., & Yang, X. (2009, 11-13 June 2009). Liver segmentation from CT images based on region growing method. In **Proceedings of the 2009 3rd International Conference on Bioinformatics and Biomedical Engineering** (pp. 1-4). Beijing, China.
- Chen, Y., Yue, X., Zhong, C., & Wang, G. (2016). Functional Region Annotation of Liver CT Image Based on Vascular Tree. **Biomed Res Int**. 2016: 5428737.
- Chi, Y., Cashman, P., Bello, F., & Kitney, R. (2007, 01/01). A discussion on the evaluation of a new automatic liver volume segmentation method for specified CT image datasets. In **Proceedings of the MICCAI Workshop on 3D Segmentation in the Clinic: A Grand Challenge** (pp. 167-175).
- Choi, P. T. (2016). Surface Conformal/Quasi-conformal Parameterization with Applications. **MPhil Thesis, The Chinese University of Hong Kong**.
- Choi, P. T., Lam, K. C., & Lui, L. M. (2015). FLASH: Fast Landmark Aligned Spherical Harmonic Parameterization for Genus-0 Closed Brain Surfaces. **SIAM Journal on Imaging Sciences**. 8(1): 67-94.
- Chung, F., & Delingette, H. (2013). Regional appearance modeling based on the clustering of intensity profiles. **Computer Vision and Image Understanding**. 117(6): 705-717.

- Ciecholewski, M. (2014). Automatic Liver Segmentation from 2D CT Images Using an Approximate Contour Model. **Journal of Signal Processing Systems for Signal Image and Video Technology**. 74(2): 151-174.
- Cignoni, P., Callieri, M., Corsini, M., Dellepiane, M., Ganovelli, F., & Ranzuglia, G. (2008). **MeshLab: an Open-Source Mesh Processing Tool** (Vol. 1).
- Clavien, P. A., Oberkofler, C. E., Raptis, D. A., Lehmann, K., Rickenbacher, A., & El-Badry, A. M. (2010). What is critical for liver surgery and partial liver transplantation: size or quality? **Hepatology**. 52(2): 715-729.
- Clavien, P. A., Petrowsky, H., DeOliveira, M. L., & Graf, R. (2007). Strategies for safer liver surgery and partial liver transplantation. **N Engl J Med**. 356(15): 1545-1559.
- Cootes, T. F., Taylor, C. J., Cooper, D. H., & Graham, J. (1995). Active Shape Models- Their Training and Application. **Computer Vision and Image Understanding**. 61(1): 38-59.
- Corness, J. A., McHugh, K., Roebuck, D. J., & Taylor, A. M. (2006). The portal vein in children: radiological review of congenital anomalies and acquired abnormalities. **Pediatr Radiol**. 36(2): 87-96, quiz 170-171.
- Couinaud, C. (1999). Liver anatomy: portal (and suprahepatic) or biliary segmentation. **Dig Surg**. 16(6): 459-467.
- da Silva, E. A. B., & Mendonça, G. V. (2005). Digital Image Processing. In W.-K. Chen (Ed.), **The Electrical Engineering Handbook** (pp. 891-910). Burlington: Academic Press.
- Datar, S., M., A. B., & Stebbins, K. (2019). Magnetic Resonance Imaging: Case Histories of Significant Medical Advances Harvard Business School

Accounting & Management Unit Working. **Harvard Business School Working.**

de la Grandmaison, G. L., Clairand, I., & Durigon, M. (2001). Organ weight in 684 adult autopsies: new tables for a Caucasoid population. **Forensic Sci Int.** 119(2): 149-154.

Debarba, H. G., Zanchet, D. J., Fracaro, D., Maciel, A., & Kalil, A. N. (2010). Efficient liver surgery planning in 3D based on functional segment classification and volumetric information. **Annu Int Conf IEEE Eng Med Biol Soc.** 2010: 4797-4800.

Desbrun, M., Meyer, M., Schröder, P., & Barr, A. H. (1999). Implicit fairing of irregular meshes using diffusion and curvature flow. In **Proceedings of the 26th annual conference on Computer graphics and interactive techniques - SIGGRAPH '99** (pp. 317-324).

Egger, J., Busse, H., Brandmaier, P., Seider, D., Gawlitza, M., Strocka, S., . . . Moche, M. (2015). Interactive Volumetry Of Liver Ablation Zones. **Scientific Reports.** 5(1): 15373.

Erdt, M., Steger, S., Kirschner, M., & Wesarg, S. (2010, 12-15 Oct. 2010). Fast automatic liver segmentation combining learned shape priors with observed shape deviation. In **Proceedings of the 2010 IEEE 23rd International Symposium on Computer-Based Medical Systems (CBMS)** (pp. 249-254).

Fang, C.-H., You, J.-H., Lau, W. Y., Lai, E. C. H., Fan, Y.-F., Zhong, S.-Z., . . . Bao, S.-S. (2012). Anatomical Variations of Hepatic Veins: Three-Dimensional Computed Tomography Scans of 200 Subjects. **World Journal of Surgery.** 36(1): 120-124.

- Fausto, N., & Riehle, K. J. (2005). Mechanisms of liver regeneration and their clinical implications. **J Hepatobiliary Pancreat Surg.** 12(3): 181-189.
- Floater, M. S., & Hormann, K. (2005, 2005//). Surface Parameterization: a Tutorial and Survey. In **Proceedings of the Advances in Multiresolution for Geometric Modelling** (pp. 157-186). Berlin, Heidelberg.
- Foruzan, A. H., Zoroofi, R. A., Hori, M., & Sato, Y. (2009). A knowledge-based technique for liver segmentation in CT data. **Comput Med Imaging Graph.** 33(8): 567-587.
- Gaba, D. M. (2004). The future vision of simulation in health care. **Qual Saf Health Care.** 13 Suppl 1(suppl 1): i2-10.
- Gang, C., Xuecheng, L., Guoqing, W., Rigao, Y., Shaoxiang, Z., Liwen, T., & Jiahong, D. (2009). Sectional anatomy of the caudate lobe of liver: based on coronal and sagittal sections. **Journal of Medical Colleges of PLA.** 24(4): 187-197.
- Ganguly, D., Chakraborty, S., Balitanas, M., & Kim, T.-h. (2010). Medical Imaging: A Review. In **Security-Enriched Urban Computing and Smart Grid** (Vol. 78, pp. 504-516).
- Garamendi, J. F., Malpica, N., Martel, J., & Schiavi, E. (2007, 2007//). Automatic Segmentation of the Liver in CT Using Level Sets Without Edges. In **Proceedings of the Pattern Recognition and Image Analysis** (pp. 161-168). Berlin, Heidelberg.
- Gloger, O., Kuhn, J., Stanski, A., Volzke, H., & Puls, R. (2010). A fully automatic three-step liver segmentation method on LDA-based probability maps for multiple contrast MR images. **Magn Reson Imaging.** 28(6): 882-897.

- Gong, N., & Chen, X. (2011). Partial liver transplantation. **Frontiers of Medicine**. 5(1): 1-7.
- Gonzalez, R. C., & Woods, R. E. (2002). **Digital Image Processing**: Prentice Hall; 2nd edition (January 15, 2002).
- Gotra, A., Sivakumaran, L., Chartrand, G., Vu, K. N., Vandenbroucke-Menu, F., Kauffmann, C., . . . Tang, A. (2017). Liver segmentation: indications, techniques and future directions. **Insights Imaging**. 8(4): 377-392.
- Graham, J., & Baldock, R. (2000). **Image Processing and Analysis: A Practical Approach**: Oxford University Press.
- Graham, R. N., Perriss, R. W., & Scarsbrook, A. F. (2005). DICOM demystified: a review of digital file formats and their use in radiological practice. **Clin Radiol**. 60(11): 1133-1140.
- Gu, X., Wang, Y., Chan, T. F., Thompson, P. M., & Yau, S. T. (2004). Genus zero surface conformal mapping and its application to brain surface mapping. **IEEE Trans Med Imaging**. 23(8): 949-958.
- Hansen, M. W., & Higgins, W. E. (1997). Relaxation methods for supervised image segmentation. **IEEE Transactions on Pattern Analysis and Machine Intelligence**. 19(9): 949-962.
- Haralick, R. M., Shanmugam, K., & Dinstein, I. H. (1973). Textural Features for Image Classification. **IEEE Transactions on Systems, Man, and Cybernetics**. SMC-3(6): 610-621.
- Heimann, T., Meinzer, H.-P., & Wolf, I. (2007, 01/01). A statistical deformable model for the segmentation of liver CT volumes. In **Proceedings of the MICCAI**

2007 Workshop Proceedings: 3D Segmentation in the Clinic: A Grand Challenge (pp. 161–166).

- Heimann, T., van Ginneken, B., Styner, M. A., Arzhaeva, Y., Aurich, V., Bauer, C., . . . Wolf, I. (2009). Comparison and evaluation of methods for liver segmentation from CT datasets. **IEEE Trans Med Imaging**, 28(8): 1251-1265.
- Horkaew, P., & Yang, G.-Z. (2004). *Construction of 3D Dynamic Statistical Deformable Models for Complex Topological Shapes*. Paper presented at the Medical Image Computing and Computer-Assisted Intervention – MICCAI 2004, Berlin, Heidelberg.
- Horn, B. K. P. (1987). Closed-form solution of absolute orientation using unit quaternions. **Journal of the Optical Society of America A**, 4(4): 629-642.
- Hounsfield, G. N. (1973). Computerized transverse axial scanning (tomography). 1. Description of system. **Br J Radiol**, 46(552): 1016-1022.
- Hu, P., Wu, F., Peng, J., Liang, P., & Kong, D. (2016). Automatic 3D liver segmentation based on deep learning and globally optimized surface evolution. **Phys Med Biol**, 61(24): 8676-8698.
- Huang, Q., Ding, H., Wang, X., & Wang, G. (2018). Fully automatic liver segmentation in CT images using modified graph cuts and feature detection. **Comput Biol Med**, 95: 198-208.
- Huang, S.-h., Wang, B.-l., Cheng, M., Wu, W.-l., Huang, X.-y., & Ju, Y. (2008, 2008//). A Fast Method to Segment the Liver According to Couinaud's Classification. In **Proceesings of the Medical Imaging and Informatics** (pp. 270-276). Berlin, Heidelberg.

- Iyengar, S. S., & Deng, W. (1995). An efficient edge detection algorithm using relaxation labeling technique. **Pattern Recognition**. 28(4): 519-536.
- Jason, M., & Stacy, G. (2017). **Computed Tomography (CT)**. Retrieved from <https://www.insideradiology.com.au/computed-tomography/>
- Jones, Y. W. J. (2018). **Couinaud classification of hepatic segments**. Retrieved from <https://radiopaedia.org/articles/couinaud-classification-of-hepatic-segments?lang=us>
- Kainmüller, D., Lange, T., & Lamecker, H. (2007, 01/01). Shape Constrained Automatic Segmentation of the Liver based on a Heuristic Intensity Model. In **Proceesings of the MICCAI 2007 Workshop Proceedings: 3D Segmentation in the Clinic: A Grand Challenge** (pp. 109–116).
- Kalra, A. (2018). Developing FE Human Models From Medical Images. In **Basic Finite Element Method as Applied to Injury Biomechanics** (pp. 389-415).
- Kasahara, M., Fukuda, A., Yokoyama, S., Sato, S., Tanaka, H., Kuroda, T., & Honna, T. (2008). Living donor liver transplantation with hyperreduced left lateral segments. **Journal of Pediatric Surgery**. 43(8): 1575-1578.
- Kaufman, A. (2003). Volume Visualization: Principles and Advances. 28.
- Keegan, J., Horkaew, P., Buchanan, T. J., Smart, T. S., Yang, G.-Z., & Firmin, D. N. (2004). Intra- and interstudy reproducibility of coronary artery diameter measurements in magnetic resonance coronary angiography. **Journal of Magnetic Resonance Imaging**. 20(1): 160-166.
- Khan, N., Ahmed, I., Kiran, M., & Adnan, A. (2016). Overview of Technical Elements of Liver Segmentation. **International Journal of Advanced Computer Science and Applications**. 7(12): 271-278.

- Kinda, A., Saddi, K., Rousson, M., & Cheriet, F. (2007). Global-to-Local Shape Matching for Liver Segmentation in CT Imaging. **Proc. MICCAI Workshop 3-D Segmentation Clinic: A Grand Challenge.**
- Kishi, Y., Abdalla, E. K., Chun, Y. S., Zorzi, D., Madoff, D. C., Wallace, M. J., . . . Vauthey, J.-N. (2009). Three hundred and one consecutive extended right hepatectomies: evaluation of outcome based on systematic liver volumetry. **Annals of surgery.** 250(4): 540-548.
- Kittler, J., & Illingworth, J. (1985). Relaxation labelling algorithms — a review. **Image and Vision Computing.** 3(4): 206-216.
- Kumar, S. S., Moni, R. S., & Rajesh, J. (2011). Automatic liver and lesion segmentation: a primary step in diagnosis of liver diseases. **Signal, Image and Video Processing.** 7(1): 163-172.
- Kumar, T. S., & Vijai, A. (2012). 3D Reconstruction of Face from 2D CT Scan Images. **Procedia Engineering.** 30: 970-977.
- Kumon, M. (2017). Anatomical Study of the Caudate Lobe with Special Reference to Portal Venous and Biliary Branches Using Corrosion Liver Casts and Clinical Application. **Liver Cancer.** 6(2): 161-170.
- Kwon, H.-J., Kim, K. W., Kim, B., Kim, S. Y., Lee, C. S., Lee, J., . . . Lee, S. G. (2018). Resection plane-dependent error in computed tomography volumetry of the right hepatic lobe in living liver donors. **Clinical and molecular hepatology.** 24(1): 54-60.
- Lamade, W., Glombitza, G., Fischer, L., Chiu, P., Cardenas, C. E., Sr., Thorn, M., . . . Herfarth, C. (2000). The impact of 3-dimensional reconstructions on operation planning in liver surgery. **Arch Surg.** 135(11): 1256-1261.

- Larbi, A., Orliac, C., Frandon, J., Pereira, F., Ruyer, A., Goupil, J., . . . Greffier, J. (2018). Detection and characterization of focal liver lesions with ultra-low dose computed tomography in neoplastic patients. **Diagn Interv Imaging**. 99(5): 311-320.
- László, R. (2014). **Automated segmentation methods for liver analysis in oncology applications**. Ph.D. Thesis. University of Szeged.
- Le, T., & Tran, D. (2018). **A Robust Liver Segmentation in CT-images Using 3D Level-Set Developed with the Edge and the Region Information**.
- Lebre, M. A., Vacavant, A., Grand-Brochier, M., Rositi, H., Abergel, A., Chabrot, P., & Magnin, B. (2019). Automatic segmentation methods for liver and hepatic vessels from CT and MRI volumes, applied to the Couinaud scheme. **Comput Biol Med**. 110: 42-51.
- Lee, J., Kim, N., Lee, H., Seo, J. B., Won, H. J., Moon Shin, Y., & Gil Shin, Y. (2007, 12/04). Efficient Liver Segmentation exploiting Level-Set Speed Images with 2.5D Shape Propagation. In **Proceedings of the MICCAI 2007 Workshop Proceedings: 3D Segmentation in the Clinic: A Grand Challenge** (pp. 189–196).
- Lee, J. H., & Won, C. H. (2011). Topology preserving relaxation labeling for nonrigid point matching. **IEEE Trans Pattern Anal Mach Intell**. 33(2): 427-432.
- Lee, S.-L., Horkaew, P., Darzi, A., & Yang, G.-Z. (2004). *Statistical Shape Modelling of the Levator Ani with Thickness Variation*. Paper presented at the Medical Image Computing and Computer-Assisted Intervention – MICCAI 2004, Berlin, Heidelberg.

- Li, D., Liu, L., Chen, J., Li, H., & Yin, Y. (2014, 20-23 Sept. 2014). A multistep liver segmentation strategy by combining level set based method with texture analysis for CT images. In **Proceedings of the 2014 International Conference on Orange Technologies** (pp. 109-112).
- Li, G., Chen, X., Shi, F., Zhu, W., Tian, J., & Xiang, D. (2015). Automatic Liver Segmentation Based on Shape Constraints and Deformable Graph Cut in CT Images. **IEEE Trans Image Process.** 24(12): 5315-5329.
- Li, G., Huang, H., Wu, S., Cohen-Or, D., Gong, M., Zhang, H., & Graph, B. (2013). L1-medial skeleton of point cloud. **ACM Transactions on Graphics.**
- Li, X., Chen, H., Qi, X., Dou, Q., Fu, C. W., & Heng, P. A. (2018). H-DenseUNet: Hybrid Densely Connected UNet for Liver and Tumor Segmentation From CT Volumes. **IEEE Trans Med Imaging.** 37(12): 2663-2674.
- Li, Y., Wang, G., Li, M., Li, J., Shi, L., & Li, J. (2020). Application of CT images in the diagnosis of lung cancer based on finite mixed model. **Saudi Journal of Biological Sciences.** 27(4): 1073-1079.
- Li, Y., Yang, Z.-w., & Deng, J.-s. (2006). Spherical parametrization of genus-zero meshes by minimizing discrete harmonic energy. **Journal of Zhejiang University-SCIENCE A.** 7(9): 1589-1595.
- Liao, M., Zhao, Y. Q., Liu, X. Y., Zeng, Y. Z., Zou, B. J., Wang, X. F., & Shih, F. Y. (2017). Automatic liver segmentation from abdominal CT volumes using graph cuts and border marching. **Comput Methods Programs Biomed.** 143: 1-12.
- Liao, M., Zhao, Y. Q., Wang, W., Zeng, Y. Z., Yang, Q., Shih, F. Y., & Zou, B. J. (2016). Efficient liver segmentation in CT images based on graph cuts and bottleneck detection. **Phys Med.** 32(11): 1383-1396.

- Lim, M. C., Tan, C. H., Cai, J., Zheng, J., & Kow, A. W. C. (2014). CT volumetry of the liver: where does it stand in clinical practice? **Clinical radiology**. 69(9): 887-895.
- Lim, S. J., Jeong, Y. Y., & Ho, Y. S. (2005). Segmentation of the liver using the deformable contour method on CT images. In **Proceedings of the Advances in Multimedia Information Processing** (pp. 570-581). Springer, Berlin, Heidelberg.
- Loffroy, R., Favelier, S., Chevallier, O., Estivalet, L., Genson, P. Y., Pottecher, P., . . . Cercueil, J. P. (2015). Preoperative portal vein embolization in liver cancer: indications, techniques and outcomes. **Quantitative imaging in medicine and surgery**. 5(5): 730-739.
- Lorensen, W., & Cline, H. (1987). Marching Cubes: A High Resolution 3D Surface Construction Algorithm. **ACM SIGGRAPH Computer Graphics**. 21: 163.
- Loukas, C. G., & Linney, A. (2005). On a relaxation-labelling algorithm for quantitative assessment of tumour vasculature in tissue section images. **Comput Biol Med**. 35(2): 157-171.
- Lu, F., Wu, F., Hu, P., Peng, Z., & Kong, D. (2017). Automatic 3D liver location and segmentation via convolutional neural network and graph cut. **Int J Comput Assist Radiol Surg**. 12(2): 171-182.
- Lu, X. Q., Wu, J. S., Ren, X. Y., Zhang, B. H., & Li, Y. H. (2014). The study and application of the improved region growing algorithm for liver segmentation. **Optik**. 125(9): 2142-2147.

- Lui, L. M., Wang, Y. L., Chan, T. F., & Thompson, P. (2007). Landmark constrained genus zero surface conformal mapping and its application to brain mapping research. **Applied Numerical Mathematics**. 57(5-7): 847-858.
- Luo, S., Li, X., & Li, J. (2014). Review on the Methods of Automatic Liver Segmentation from Abdominal Images. **Journal of Computer and Communications**. 02(02): 1-7.
- M Dawant, B., Li, R., Lennon, B., & Li, S. (2007). Semi-automatic segmentation of the liver and its evaluation on the MICCAI 2007 grand challenge data set. **Proc. MICCAI Workshop on 3-D Segmentat. Clinic: A Grand Challenge**.
- Magid, E., Soldea, O., & Rivlin, E. (2007). A comparison of Gaussian and mean curvature estimation methods on triangular meshes of range image data. **Computer Vision and Image Understanding**. 107(3): 139-159.
- Maklad, A. S., Matsuhira, M., Suzuki, H., Kawata, Y., Niki, N., Satake, M., . . . Shimada, M. (2013). Blood vessel-based liver segmentation using the portal phase of an abdominal CT dataset. **Med Phys**. 40(11): 113501.
- Martel, G., Cieslak, K. P., Huang, R., van Lienden, K. P., Wiggers, J. K., Belblidia, A., . . . Vandenbroucke-Menu, F. (2015). Comparison of techniques for volumetric analysis of the future liver remnant: implications for major hepatic resections. **HPB (Oxford)**. 17(12): 1051-1057.
- May, B. J., & Madoff, D. C. (2012). Portal vein embolization: rationale, technique, and current application. **Seminars in interventional radiology**. 29(2): 81-89.
- McReynolds, T., & Blythe, D. (2005). **Advanced Graphics Programming Using OpenGL**: Morgan Kaufmann.

- Mesmoudi, M. M., De Florian, L., & Magillo, P. (2012, 2012//). Discrete Curvature Estimation Methods for Triangulated Surfaces. In **Proceedings of the Applications of Discrete Geometry and Mathematical Morphology** (pp. 28-42). Berlin, Heidelberg.
- Meyer, M., Desbrun, M., Schröder, P., & Barr, A. H. (2003, 2003//). Discrete Differential-Geometry Operators for Triangulated 2-Manifolds. In **Proceedings of the Visualization and Mathematics III** (pp. 35-57). Berlin, Heidelberg.
- Mharib, A. M., Ramli, A. R., Mashohor, S., & Mahmood, R. B. (2012). Survey on liver CT image segmentation methods. **Artificial Intelligence Review**. 37(2): 83-95.
- Mihaylova, A., & Georgieva, V. (2016). Comparative analysis of various filters for noise reduction in mri abdominal images. **International Journal "INFORMATION TECHNOLOGIES & KNOWLEDGE" (IJ ITK)**. 10.
- Mise, Y., Tani, K., Aoki, T., Sakamoto, Y., Hasegawa, K., Sugawara, Y., & Kokudo, N. (2013). Virtual liver resection: computer-assisted operation planning using a three-dimensional liver representation. **J Hepatobiliary Pancreat Sci**. 20(2): 157-164.
- Moccia, S., De Momi, E., El Hadji, S., & Mattos, L. S. (2018). Blood vessel segmentation algorithms — Review of methods, datasets and evaluation metrics. **Computer Methods and Programs in Biomedicine**. 158: 71-91.
- Moghbel, M., Mashohor, S., Mahmud, R., & Saripan, M. I. B. (2018). Review of liver segmentation and computer assisted detection/diagnosis methods in computed tomography. **Artificial Intelligence Review**. 50(4): 497-537.
- Mohamed, F., A., & Viriri, S. (2017, 17-19 Nov. 2017). Liver segmentation: A survey of the state-of-the-art. In **Proceedings of the 2017 Sudan Conference on**

Computer Science and Information Technology (SCCSIT) (pp. 1-6).

Elnihood, Sudan.

Mohamed, R. G., Seada, N. A., Hamdy, S., & Mostafa, M. G. (2017). An Adaptive Method for Fully Automatic Liver Segmentation in Medical MRI-Images.

International Journal of Computer Applications. 179(4): 12-18.

Mosteller, R. D. (1987). Simplified calculation of body-surface area. **N Engl J Med.** 317(17): 1098.

Nakayama, K., Oshiro, Y., Miyamoto, R., Kohno, K., Fukunaga, K., & Ohkohchi, N. (2017). The Effect of Three-Dimensional Preoperative Simulation on Liver

Surgery. **World J Surg.** 41(7): 1840-1847.

Namgoong, J.-M., Hwang, S., Song, G.-W., Kim, D.-Y., Ha, T.-Y., Jung, D.-H., . . .

Kwon, Y. J. (2020). Pediatric liver transplantation with hyperreduced left lateral segment graft. **Annals of hepato-biliary-pancreatic surgery.** 24(4): 503-512.

Newman, T. (2018). **What does the liver do?** Retrieved from

<https://www.medicalnewstoday.com/articles/305075.php>

Nilsson, O., Breen, D., & Museth, K. (2005). **Surface reconstruction via contour metamorphosis: an Eulerian approach with Lagrangian particle tracking.**

Ojala, T., Pietikäinen, M., & Harwood, D. (1996). A comparative study of texture measures with classification based on featured distributions. **Pattern**

Recognition. 29(1): 51-59.

Ojala, T., Pietikainen, M., & Maenpaa, T. (2002). Multiresolution gray-scale and rotation invariant texture classification with local binary patterns. **IEEE**

Transactions on Pattern Analysis and Machine Intelligence. 24(7): 971-987.

Oliveira, D., Feitosa, R., & Correia, M. (2008). **Automatic Couinaud Liver and Veins Segmentation from CT Images.**

OpenCV library. (2020). Retrieved from <https://opencv.org>

Osher, S., & Sethian, J. A. (1988). Fronts propagating with curvature-dependent speed: Algorithms based on Hamilton-Jacobi formulations. **Journal of Computational Physics.** 79(1): 12-49.

Oshiro, Y., & Ohkohchi, N. (2017). Three-Dimensional Liver Surgery Simulation: Computer-Assisted Surgical Planning with Three-Dimensional Simulation Software and Three-Dimensional Printing. **Tissue Eng Part A.** 23(11-12): 474-480.

Oshiro, Y., Yano, H., Mitani, J., Kim, S., Kim, J., Fukunaga, K., & Ohkohchi, N. (2015). Novel 3-dimensional virtual hepatectomy simulation combined with real-time deformation. **World journal of gastroenterology.** 21(34): 9982-9992.

Otsu, N. (1979). A Threshold Selection Method from Gray-Level Histograms. **IEEE Transactions on Systems, Man, and Cybernetics.** 9(1): 62-66.

Pamulapati, V., Venkatesan, A., Wood, B., & Linguraru, M. G. (2011). **Liver Segmental Anatomy and Analysis from Vessel and Tumor Segmentation via Optimized Graph Cuts** (Vol. 7029).

Peng, J., Hu, P., Lu, F., Peng, Z., Kong, D., & Zhang, H. (2015). 3D liver segmentation using multiple region appearances and graph cuts. **Med Phys.** 42(12): 6840-6852.

Perona, P., & Malik, J. (1990). Scale-space and edge detection using anisotropic diffusion. **IEEE Transactions on Pattern Analysis and Machine Intelligence.** 12(7): 629-639.

- Pescia, D. (2011). **Segmentation des tumeurs du foie sur des images CT. (Segmentation of liver tumors on CT images)**. Thesis. Retrieved from <https://tel.archives-ouvertes.fr/tel-00649030>
- Pinheiro, R., Cruz-Jr, R., Andraus, W., Ducatti, L., Martino, R., Nacif, L., . . . D'Albuquerque, L. (2017). Preoperative computed tomography volumetry and graft weight estimation in adult living donor liver transplantation. **ABCD. Arquivos Brasileiros de Cirurgia Digestiva (São Paulo)**. 30: 38-41.
- Qian, K., Su, K. H., Zhang, J. L., & Li, Y. H. (2018). A 3D face registration algorithm based on conformal mapping. **Concurrency and Computation-Practice & Experience**. 30(22): e4654.
- Reitinger, B., Bornik, A., Beichel, R., & Schmalstieg, D. (2006). Liver surgery planning using virtual reality. **IEEE Comput Graph Appl**. 26(6): 36-47.
- Ribero, D., Abdalla, E. K., Madoff, D. C., Donadon, M., Loyer, E. M., & Vauthey, J. N. (2007). Portal vein embolization before major hepatectomy and its effects on regeneration, resectability and outcome. **Br J Surg**. 94(11): 1386-1394.
- Richard, M., & Goergen, S. (2018). **Magnetic Resonance Imaging (MRI)**. Retrieved from <https://www.insideradiology.com.au/mri/>
- Richards, J., Landgrebe, D., & Swain, P. (1981). **On the accuracy of pixel relaxation labeling**.
- Robin, S., & Eduard, E. d. L. (2015, 2015). **Anatomy of the liver segments**. Retrieved from <http://www.radiologyassistant.nl/en/p4375bb8dc241d/anatomy-of-the-liver-segments.html#in56349fa61d4f7>

- Rose, K., Praun, E., & Sheffer, A. (2006). Mesh Parameterization Methods and Their Applications. **Foundations and Trends® in Computer Graphics and Vision**. 2(2): 105-171.
- Rosenfeld, A., Hummel, R. A., & Zucker, S. W. (1976). Scene Labeling by Relaxation Operations. **IEEE Transactions on Systems, Man, and Cybernetics**. SMC-6(6): 420-433.
- Ruskó, L., Bekes, G., Németh, G., & Fidrich, M. (2007). **Fully automatic liver segmentation for contrast-enhanced CT images**.
- Rusko, L., Mateka, I., & Kriston, A. (2013). Virtual volume resection using multi-resolution triangular representation of B-spline surfaces. **Comput Methods Programs Biomed**. 111(2): 315-329.
- Sagoo, M. G., Aland, R. C., & Gosden, E. (2018). Morphology and morphometry of the caudate lobe of the liver in two populations. **Anat Sci Int**. 93(1): 48-57.
- Sahi, K., Jackson, S., Wiebe, E., Armstrong, G., Winters, S., Moore, R., & Low, G. (2014). The value of "liver windows" settings in the detection of small renal cell carcinomas on unenhanced computed tomography. **Can Assoc Radiol J**. 65(1): 71-76.
- Schukfeh, N., Schulze, M., Holland, A. C., Dingemann, J., Hoyer, D. P., Paul, A., & Theysohn, J. M. (2018). Computed tomography donor liver volumetry before liver transplantation in infants ≤ 10 kg: does the estimated graft diameter affect the outcome? **Innovative surgical sciences**. 3(4): 253-259.
- Seghers, D., Slagmolen, P., Lambelin, Y., Hermans, J., Loeckx, D., Maes, F., & Suetens, P. (2007). Landmark based liver segmentation using local shape and local

intensity models. **MICCAI Workshop on 3D Segmentation in the Clinic: A Grand Challenge.**

Selle, D., Preim, B., Schenk, A., & Peitgen, H. O. (2002). Analysis of vasculature for liver surgical planning. **IEEE Trans Med Imaging.** 21(11): 1344-1357.

Selver, M. A., Kocaoglu, A., Demir, G. K., Dogan, H., Dicle, O., & Guzelis, C. (2008). Patient oriented and robust automatic liver segmentation for pre-evaluation of liver transplantation. **Comput Biol Med.** 38(7): 765-784.

Sethian, J. A. (1996). A fast marching level set method for monotonically advancing fronts. **Proceedings of the National Academy of Sciences of the United States of America.** 93(4): 1591-1595.

Shen, L., & Chung, M. K. (2006, 14-16 June 2006). Large-Scale Modeling of Parametric Surfaces Using Spherical Harmonics. In **Proceedings of the Third International Symposium on 3D Data Processing, Visualization, and Transmission (3DPVT'06)** (pp. 294-301).

Smith, S. W. (1997). **The scientist and engineer's guide to digital signal processing:** California Technical Publishing.

Society, A. C. (2018). *Global Cancer Facts & 4th Edition.* Retrieved from Atlanta: American Cancer Society: <https://www.cancer.org/research/cancer-facts-statistics/global.html>

Soyer, P., Roche, A., Elias, D., & Levesque, M. (1992). Hepatic metastases from colorectal cancer: influence of hepatic volumetric analysis on surgical decision making. **Radiology.** 184(3): 695-697.

Stehr, W., & Gingalewski, C. A. (2012). Other Causes of Intestinal Obstruction. In A. G. Coran (Ed.), **Pediatric Surgery** (pp. 1127-1134). Philadelphia: Mosby.

- Sunder, R., Howard, B., Kyoko, F., Wolfgang, K., & David, S. (2018). **Magnetic Resonance Imaging (MRI) Safety and Effectiveness**. Retrieved from <https://www.fda.gov/medical-devices/cdrh-research-programs/magnetic-resonance-imaging-mri-safety-and-effectiveness>
- Sunder, R., Howard, B., Kyoko, F., Wolfgang, K., & David, S. (2019). **Computed Tomography (CT)**. Retrieved from <https://www.fda.gov/radiation-emitting-products/medical-x-ray-imaging/computed-tomography-ct>
- Sung, H., Ferlay, J., Siegel, R. L., Laversanne, M., Soerjomataram, I., Jemal, A., & Bray, F. (2021). Global Cancer Statistics 2020: GLOBOCAN Estimates of Incidence and Mortality Worldwide for 36 Cancers in 185 Countries. **CA: A Cancer Journal for Clinicians**. 71(3): 209-249.
- Tang, S., & Tang, X. (2012). Statistical CT noise reduction with multiscale decomposition and penalized weighted least squares in the projection domain. **Med Phys**. 39(9): 5498-5512.
- Taubin, G. (1999). A Signal Processing Approach To Fair Surface Design. **Computer Graphics (Proceedings of Siggraph '95)**. 29.
- U. Kishan, A., & Lee, P. (2016). MRI-guided radiotherapy: Opening our eyes to the future. **Integrative Cancer Science and Therapeutics**. 3(2): 420-427.
- V, G., & BW, N. (2020, 2020 Aug 15). **Anatomy, Abdomen and Pelvis, Falciform Ligament**. Retrieved from <https://www.ncbi.nlm.nih.gov/books/NBK539858>
- Vascular Modeling Toolkit**. (2020). Retrieved from <http://www.vmtk.org/>
- Vauthey, J. N., Abdalla, E. K., Doherty, D. A., Gertsch, P., Fenstermacher, M. J., Loyer, E. M., . . . Denys, A. (2002). Body surface area and body weight predict total liver volume in Western adults. **Liver Transpl**. 8(3): 233-240.

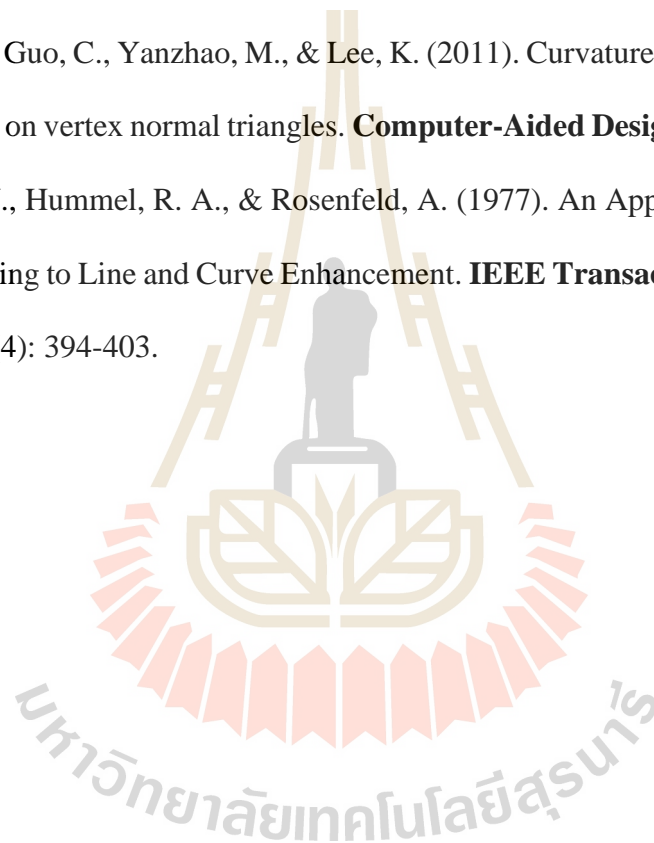
- Vauthey, J. N., Chaoui, A., Do, K. A., Bilimoria, M. M., Fenstermacher, M. J., Charnsangavej, C., . . . Caridi, J. (2000). Standardized measurement of the future liver remnant prior to extended liver resection: methodology and clinical associations. **Surgery**. 127(5): 512-519.
- Vekemans, K., & Braet, F. (2005). Structural and functional aspects of the liver and liver sinusoidal cells in relation to colon carcinoma metastasis. **World journal of gastroenterology**. 11(33): 5095-5102.
- Visualization Toolkit**. (2020). Retrieved from <https://vtk.org/>
- Wahab, M. A., Fathy, O., Elhanafy, E., Atif, E., Sultan, A. M., Salah, T., . . . Sultan, A. (2011). Caudate lobe resection for hepatocellular carcinoma. **Hepatogastroenterology**. 58(112): 1904-1908.
- Wang, D. S., Hassan, O., Morgan, K., & Weatherill, N. (2006). Efficient surface reconstruction from contours based on two-dimensional Delaunay triangulation. **International Journal for Numerical Methods in Engineering**. 65(5): 734-751.
- Wang, F., Pan, K.-T., Chu, S.-Y., Chan, K.-M., Chou, H.-S., Wu, T.-J., & Lee, W.-C. (2011). Preoperative estimation of the liver graft weight in adult right lobe living donor liver transplantation using maximal portal vein diameters. **Liver Transplantation**. 17(4): 373-380.
- Wang, H., Zhang, H., & Ray, N. (2012). Clump splitting via bottleneck detection and shape classification. **Pattern Recognition**. 45(7): 2780-2787.
- Wang, Y., Gu, X., Chan, T. F., Thompson, P. M., & Yau, S.-T. (2004, 12 May 2004). Intrinsic brain surface conformal mapping using a variational method. In

- Proceedings of the Medical Imaging 2004: Image Processing** (pp. 241-252). San Diego, California, United States.
- Wang, Y., Lui, L. M., Chan, T. F., & Thompson, P. M. (2005). Optimization of Brain Conformal Mapping with Landmarks. In **Proceedings of the 8th international conference on Medical image computing and computer-assisted intervention** (pp. 675-683). Berlin, Heidelberg.
- Whitaker, R. T., & Xinwei, X. (2001, 7-10 Oct. 2001). Variable-conductance, level-set curvature for image denoising. In **Proceedings of the 2001 International Conference on Image Processing (Cat. No.01CH37205)** (pp. 142-145 vol.143).
- WHO. (2018). *Latest global cancer data*. Retrieved from
- Wilson, B. G. (2005). The evolution of PET-CT. **Radiol Technol.** 76(4): 301-313; quiz 314-306, 319.
- Withey, D. J., & Koles, Z. J. (2007, 12-14 Oct. 2007). Medical image segmentation: method and software. In **Proceedings of the Noninvasive Functional Source Imaging of the Brain and Heart and the International Conference on Functional Biomedical Imaging** (pp. 140-143). Hangzhou, China.
- Wu, P. H., Bedoya, M., White, J., & Brace, C. L. (2021). Feature-based automated segmentation of ablation zones by fuzzy c-mean clustering during low-dose computed tomography. **Med Phys.** 48(2): 703-714.
- Wu, W., Zhou, Z., Wu, S., & Zhang, Y. (2016). Automatic Liver Segmentation on Volumetric CT Images Using Supervoxel-Based Graph Cuts. **Comput Math Methods Med.** 2016: 9093721.

- Yang, G. Z., Burger, P., Firmin, D. N., & Underwood, S. R. (1996). Structure adaptive anisotropic image filtering. **Image and Vision Computing**. 14(2): 135-145.
- Yang, X., Lee, W., Choi, Y., & You, H. (2012). Development of A User-Centered Virtual Liver Surgery Planning System. In **Proceedings of the Proceedings of the Human Factors and Ergonomics Society Annual Meeting** (pp. 772-776). Boston, MA.
- Yang, X., Lee, W., Choi, Y., & You, H. (2012). Development of A User-Centered Virtual Liver Surgery Planning System. In **Proceedings of the Proceedings of the Human Factors and Ergonomics Society Annual Meeting** (pp. 772-776). Boston, MA.
- Yang, X., Yang, J. D., Hwang, H. P., Yu, H. C., Ahn, S., Kim, B. W., & You, H. (2018). Segmentation of liver and vessels from CT images and classification of liver segments for preoperative liver surgical planning in living donor liver transplantation. **Comput Methods Programs Biomed**. 158: 41-52.
- Yang, X., Yang, J. D., Yu, H. C., Choi, Y., Yang, K., Lee, T. B., . . . You, H. (2018). Dr. Liver: A preoperative planning system of liver graft volumetry for living donor liver transplantation. **Comput Methods Programs Biomed**. 158: 11-19.
- Yang, X., Yu, H. C., Choi, Y., Lee, W., Wang, B., Yang, J., . . . You, H. (2014). A hybrid semi-automatic method for liver segmentation based on level-set methods using multiple seed points. **Comput Methods Programs Biomed**. 113(1): 69-79.
- Yeo, C. T., MacDonald, A., Ungi, T., Lasso, A., Jalink, D., Zevin, B., . . . Nanji, S. (2018). Utility of 3D Reconstruction of 2D Liver Computed

- Tomography/Magnetic Resonance Images as a Surgical Planning Tool for Residents in Liver Resection Surgery. **J Surg Educ.** 75(3): 792-797.
- Yoneyama, T., Asonuma, K., Okajima, H., Lee, K.-J., Yamamoto, H., Takeichi, T., . . . Inomata, Y. (2011). Coefficient Factor for Graft Weight Estimation from Preoperative Computed Tomography Volumetry in Living Donor Liver Transplantation. **Liver transplantation : official publication of the American Association for the Study of Liver Diseases and the International Liver Transplantation Society.** 17: 369-372.
- Yueh, M.-H., Gu, X., Lin, W.-W., Wu, C.-T., & Yau, S.-T. (2015). Conformal Surface Morphing with Applications on Facial Expressions. **arXiv.** arXiv:1504.00097.
- Yussof, W. N. J. H. W., & Burkhardt, H. (2009). 3d anisotropic diffusion for liver segmentation. In **Proceedings of the World Academy of Science, Engineering and Technology** (pp. 1749-1753).
- Yussof, W. N. J. H. W., & Burkhardt, H. (2011). Automatic 3 D Liver Segmentation Using Morphological Operations and Graph-Cut Techniques. **Journal of Next Generation Information Technology.** 2(3): 23-34.
- Zaitoun, N. M., & Aqel, M. J. (2015). Survey on Image Segmentation Techniques. **Procedia Computer Science.** 65: 797-806.
- Zayane, O., Jouini, B., & Mohamed, A. M. (2011). Automatic liver segmentation method in CT images. **Image processing and computer vision.** 2(8): 1923-1717.
- Zhang, Q., Fan, Y. F., Wan, J. F., & Liu, Y. X. (2017). An Efficient and Clinical-Oriented 3D Liver Segmentation Method. **IEEE Access.** 5: 18737-18744.

- Zhao, H. X., & Xu, G. L. (2006). Triangular surface mesh fairing via Gaussian curvature flow. **Journal of Computational and Applied Mathematics**. 195(1-2): 300-311.
- Zheng, Y., Ai, D., Mu, J., Cong, W., Wang, X., Zhao, H., & Yang, J. (2017). Automatic liver segmentation based on appearance and context information. **Biomed Eng Online**. 16(1): 16.
- Zhihong, M., Guo, C., Yanzhao, M., & Lee, K. (2011). Curvature estimation for meshes based on vertex normal triangles. **Computer-Aided Design**. 43(12): 1561-1566.
- Zucker, S. W., Hummel, R. A., & Rosenfeld, A. (1977). An Application of Relaxation Labeling to Line and Curve Enhancement. **IEEE Transactions on Computers**. C-26(4): 394-403.



List of Publication

- Le, D. C., Chinnasarn, K., Chansangrat, J., Keeratibharat, N., & Horkaew, P. (2021). Semi-automatic liver segmentation based on probabilistic models and anatomical constraints. *Sci Rep*, *11*(1), 6106. doi:10.1038/s41598-021-85436-7
- Le, D. C., Chansangrat, J., Keeratibharat, N., & Horkaew, P. (2021). Functional Segmentation for Preoperative Liver Resection Based on Hepatic Vascular Networks. *IEEE Access*, *9*, 15485-15498. doi:10.1109/Access.2021.3053384
- Le, D. C., Chansangrat, J., Keeratibharat, N., & Horkaew, P. (2021). Symmetric Reconstruction of Functional Liver Segments and Cross-Individual Correspondence of Hepatectomy. *Diagnostics*, *11*(5), 852. doi:10.3390/diagnostics11050852



BIOGRAPHY

Mr. Doan Cong Le was born on 1984 in An Giang province, Viet Nam. He received his Bachelor's degree in Computer from An Giang University and Master's degree in Computer science from Vietnam National University Ho Chi Minh City - University of Science (VNUHCM-US). He received the SUT-PhD Scholarship Program for ASEAN from Suranaree University of Technology in 2017. His research interests include image segmentation and 3D face re-construction.

